İSTANBUL TECHNICAL UNIVERSITY ★ GRADUATE SCHOOL OF SCIENCE ENGINEERING AND TECHNOLOGY

FABRICATION OF POLYMER–BIOACTIVE GLASS NANOCOMPOSITE MATERIALS IN BONE TISSUE ENGINEERING APPLICATIONS

Ph.D. THESIS

Seza Özge GÖNEN

Department of Chemical Engineering

Chemical Engineering Programme

JUNE 2016

İSTANBUL TECHNICAL UNIVERSITY ★ GRADUATE SCHOOL OF SCIENCE ENGINEERING AND TECHNOLOGY

FABRICATION OF POLYMER–BIOACTIVE GLASS NANOCOMPOSITE MATERIALS IN BONE TISSUE ENGINEERING APPLICATIONS

Ph.D. THESIS

Seza Özge GÖNEN
(506102003)

Department of Chemical Engineering

Chemical Engineering Programme

Thesis Advisor: Prof. Dr. Sadriye OSKAY
Thesis Co-Advisor: Assoc. Prof. Dr. Melek EROL TAYGUN

JUNE 2016

İSTANBUL TEKNİK ÜNİVERSİTESİ ★ FEN BİLİMLERİ ENSTİTÜSÜ

KEMİK DOKU MÜHENDİSLİĞİ UYGULAMALARI İÇİN POLİMER–BİYOAKTİF CAM NANOKOMPOZİT MALZEMELERİN ÜRETİLMESİ

DOKTORA TEZİ

Seza Özge GÖNEN
(506102003)

Kimya Mühendisliği Anabilim Dalı

Kimya Mühendisliği Programı

Tez Danışmanı: Prof. Dr. Sadriye OSKAY
Eş Danışman: Doç. Dr. Melek EROL TAYGUN

HAZİRAN 2016

Seza Özge Gönen, a Ph.D. student of İTU Graduate School of Science Engineering and Technology student ID 506102003, successfully defended the dissertation entitled "FABRICATION OF POLYMER–BIOACTIVE GLASS NANOCOMPOSITE MATERIALS IN BONE TISSUE ENGINEERING APPLICATIONS", which she prepared after fulfilling the requirements specified in the associated legislations, before the jury whose signatures are below.

Thesis Advisor :	**Prof. Dr. Sadriye OSKAY** İstanbul Technical University	.....
Co-advisor :	**Assoc. Prof. Dr. Melek EROL TAYGUN** İstanbul Technical University	.....
Jury Members :	**Prof. Dr. Hanzade AÇMA** İstanbul Technical University	.....
	Prof. Dr. Ülker BEKER Yıldız Technical University	.....
	Prof. Dr. Sibel SARGUT Marmara University	.....
	Prof. Dr. Gülhayat SAYGILI İstanbul Technical University	.....
	Assoc. Prof. Dr. Didem SALOĞLU Yalova University	.....

Date of Submission : 22 April 2016
Date of Defense : 28 June 2016

To my parents and brother,

FOREWORD

I would like to express my most sincere gratitude towards my advisor, Prof. Dr. Sadriye KÜÇÜKBAYRAK, for her generous guidance throughout my study.

My sincere thanks also go to my co-advisor, Assoc. Prof. Dr. Melek EROL TAYGUN, whose invaluable help made my study easy for me.

Appreciations are also cordially extended to my PhD thesis committee members, Prof. Dr. Hanzade AÇMA, Prof. Dr. Ülker BEKER, and Prof. Dr. Sibel SARGUT.

I would like to express my appreciation to TUBITAK–BIDEB for their financial support throughout my graduate education. Their financial support is the biggest reason I complete this thesis.

Allow me to extend my thanks to all challenges I have faced with. Those challenges made me discover myself and have transformed me into a much better version of myself.

I am obliged to thank M.Sc. Ayşen AKTÜRK for her meritorious helps and her friendship during my last six years. I am also extremely grateful to all my friends, especially Özge ÇELEBİCAN, Simge Elif ALTAŞ, Nilay BAYLAN, and Nuray YERLİ, for their support, friendship and patience. They were there for me through thick and thin. They have supported me constantly and never let me lose my faith.

Last but not least, I am greatly indebted to my family for their unconditional love, support, encouragement, and patience that enabled me to complete this study. They have never given up on me even though I thought about giving up on myself. This thesis could not have been completed without their support and patience.

June 2016

Seza Özge GÖNEN
(M.Sc. Chemical Engineer)

TABLE OF CONTENTS

Page

ABBREVIATIONS

AcOH	**:** Acetic Acid
BG	**:** Bioactive Glass
Cu-BG	**:** Copper Substituted Bioactive Glass
ECM	**:** Extracellular Matrix
FT-IR	**:** Fourier-Transform Infrared
GTA	**:** Glutaraldehyde
ICP-MS	**:** Inductively Coupled Plasma – Mass Spectrometer
PCL	**:** Poly(ϵ-Caprolactone)
RSM	**:** Response Surface Methodology
SBF	**:** Simulated Body Fluid
SEM	**:** Scanning Electron Microscope
Sr-BG	**:** Strontium Substituted Bioactive Glass
XRD	**:** X-ray Diffraction Analyzer

SYMBOLS

C_0	**:** Constant Term
C_i	**:** Linear Effect Term
C_{ii}	**:** Squared Effect Term
C_{ij}	**:** Interaction Effect Term
X_i	**:** ith Independent Factor
y	**:** Average Fiber Diameter

LIST OF TABLES

Page

LIST OF FIGURES

Page

FABRICATION OF POLYMER–BIOACTIVE GLASS NANOCOMPOSITE MATERIALS IN BONE TISSUE ENGINEERING APPLICATIONS

SUMMARY

The main driving idea of the study was to produce nano-scaled bioactive glass/polymer composite scaffolds with the inclusion of relevant ions in order to develop multifunctional scaffolds for bone tissue engineering. The originality of the study was related to the integration of several functions in a single advanced scaffold composite system based on specific compositions of bioactive glasses, providing a platform for the delivery of therapeutic ions, and biodegradable polymers as the backbone material. This new material was aimed to have the capacity, through engineered nanoparticles and tailored kinetic release of specific ions, to stimulate early angiogenesis and provide an ideal scaffold for cell recruitment and proliferation, thereby accelerating the bone repair process. In this context, nano-scaled materials from polymer blends (e.g., gelatin/sodium alginate and gelatin/poly(ε-caprolactone)), as well as their composites with bioactive glasses were fabricated with the use of electrospinning technique. In electrospinning technique, solutions containing blends of polymers without or with bioactive glass particles were prepared to be converted into electrospun nanofibers at the relevant conditions. For this purpose, the optimal solution parameters (i.e., concentration of each polymer solution, ratio of one polymer to another, and solvent composition) to produce polymeric scaffolds were first investigated by using Box-Behnken design technique. Secondly, the processing parameters (e.g., applied voltage, tip-to-collector distance, and feeding rate) were also optimized in order to conduct a stable electrospinning process and to have a desirable surface topography.Then, cross-linking treatment was also carried out for enhancing the surface properties of the obtained scaffolds. After that, microstructural and physical properties of the polymeric and nanocomposite scaffolds were determined by using scanning electron microscope, X-ray diffraction, Fourier transform infrared spectrophotometer, and differential thermal analyzer. Finally, a comprehensive in vitro simulated body fluid study was also evaluated to determine the bioactivity of the nanocomposite scaffolds. Furthermore, the release of therapeutic ions from the nanocomposite scaffolds was investigated by using inductively coupled plasma optical emission spectrometry. The overall results put forth that scaffolds obtained in this study could be promising candidates for bone tissue engineering applications.

KEMİK DOKU MÜHENDİSLİĞİ UYGULAMALARI İÇİN POLİMER–BİYOAKTİF CAM NANOKOMPOZİT MALZEMELERİN ÜRETİLMESİ

ÖZET

Kemik; mekanik destek sağlayan, mineral deposu olarak davranan, hareketi sağlayan kas kasılmalarını destekleyen, yük taşıyan ve iç organları koruyan oldukça karmaşık bir doku olup, zarar gördüğünde belirli bir ölçüye kadar kendini yara izi olmaksızın yenileyebilmektedir. Ancak, hasarın oldukça ciddi olduğu durumlarda, kemiğin onarılması ve yenilenmesi için otojenik ve allojenik kaynakların kullanılmasına bir alternatif oluşturan kemik doku mühendisliği yaklaşımına ihtiyaç duyulmaktadır. Bu yaklaşım; hücre dışı matrisi taklit eden, üzerinde hücrelerin tutunduğu ve çoğaldığı geçici bir destek görevi gören yapı iskelelerinin kullanımına dayanmaktadır.

Yakın geçmişte, nanopartikül, nanolif ve nanocompozit şeklindeki biyomalzemelerin kemik doku mühendisliği uygulamalarında kullanılması oldukça ilgi uyandırmaktadır. Özellikle, kemik rejenerasyonu için arzu edilen özelliklere sahip, çapları birkaç mikron ile birkaç nanometre arasındaki liflerden oluşan yapı iskeleleri oluşturmak için elektrospinning yöntemi kullanılmaktadır. Elektrospinning yöntemi; basit ve etkili bir araç olup temel olarak hücre dışı matrise yapısal benzerliği, geniş bir malzeme yelpazesi ile çalışılabilmesi, cihazın kurulumunun basit ve ucuz olması gibi özellikleri nedeniyle son zamanlarda kemik doku mühendisliği uygulamalarında ilgi görmektedir.

Hücre dışı matrisin lifli yapısını taklit etmek amacıyla en uygun malzeme seçilirken, malzemenin özelliklerinin yapı iskelesinin özelliklerini belirleyeceği de dikkate alınmalıdır. Şimdiye kadar, sentetik veya doğal olanlar dahil olmak üzere birçok farklı polimer araştırılmıştır. Ancak, ideal bir yapı iskelesi için gerekli tüm özelliklerin tek bir malzeme ile sağlanması mümkün değildir. Kemiğin hücre dışı matrisi, organik ve inorganik maddelerden oluşan bir nanokompozit olduğundan; polimerlerin ve biyoaktif seramiklerin birlikte kullanılması ile daha iyi mekanik özelliğe, hidrofilikliğe, osteoiletkenliğe, osteoendüktiviteye ve hücresel afiniteye sahip yapı iskelelerinin üretilmesi beklenmektedir. Bununla birlikte; tek bir malzeme içerisinde her iki bileşen de içerildiğinden, organik kısmın esnekliğine ve iyi şekillendirilme yeteneğine; inorganik kısmın ise, ısıl kararlılığına, yüksek mukavemetine ve kimyasal direncine sahip olunacaktır. In vitro ve in vivo çalışmalar, organik/inorganik kompozit yapı iskelelerinin, osteoblastların ve mezenkimal kök hücrelerinin tutunmasını, çoğalmasını ve farklılaşmasını desteklediğini ve kemik iyileşmesini kolaylaştırdığını göstermiştir.

Bunlara ek olarak; ideal bir yapı iskelesi geliştirebilmek için malzemelerin damarlaşmayı (anjiyogenez) hızlandırması ve osteoblastlar ile endotel hücrelerin çoğalmasını teşvik etmesi de gereklidir. Bu nedenle; anjiyogenezi uyaran malzemelerin geliştirilmesi de oldukça önemlidir. Bu bağlamda; yapı iskelesine ek işlevler (yani, anjiyojenik ve antibakteriyel etkileri) sağlamak için terapötik metalik iyon salınımı da yapan bir malzeme geliştirmek etkili ve ucuz bir yaklaşımdır.

Stronsiyum, osteoklast bağlantılı kemik erimesini inhibe ederken osteoblast ilişkili kemik oluşumunu teşvik eden ikili bir etki gösterdiğinden; bakır ise, hem antibakteriyel aktiviteye hem de anjiyojenezi geliştirme etkisine sahip olduğundan stronsiyum ve/veya bakır salınımı yapan malzemelerin yapı iskelesi olarak kullanılmalarının etkili bir yaklaşım olduğu düşünülmektedir. Bu bağlamda; bu doktora tezi kapsamında gelişmiş anjiyojenez potansiyeline sahip ve antibakteriyel özellik gösteren çok fonksiyonlu nanokompozit yapı iskelelerinin elektrospinning yöntemi kullanılarak geliştirilmesi hedeflenmiştir.

Doğal ve sentetik polimerler tek başlarına istenilen bütün özellikleri sağlayamazlar. Bu nedenle; iki biyopolimer (jelatin ve sodyum aljinat) ile bir sentetik polimer (poli(ε-kaprolakton)) deneysel çalışmalarda kullanılan üzere seçilmiş ve yapı iskeleleri bunların ikili karışımlarından (jelatin/poli(ε-kaprolakton) ve jelatin/sodyum aljinat) hazırlanmıştır. Jelatin ve sodyum aljinat, hücre dışı matrisin ana bileşenlerinden kolajen ve glikozaminoglikan ile benzerlik göstermektedirler. Buna ek olarak; biyobozunurluk, biyouyumluluk, hidrofilik olma ve nispeten düşük maliyetle ticari kullanılabilirlik gibi birçok avantaja sahip olduklarından, biyomedikal uygulamalarda yaygın olarak kullanılmaktadırlar. Öte yandan; poli(ε-kaprolakton) ise, biyouyumluluk, biyolojik olarak rezorbe edilebilirlik, ucuzluk ve birçoğunun Gıda ve İlaç İdaresi tarafından onaylı olması gibi bazı benzersiz özelliklere sahiptir.

Üretilen lif çapı; proses değişkenleri (uygulanan gerilim, polimer çözeltisinin akış hızı, iğne ucu ve toplayıcı arasındaki açıklık, iğnenin çapı, kolektör tipi), çözelti değişkenleri (polimerin molekül ağırlığı, polimer çözeltisinin derişimi, çözücü tipi) ve çevre koşulları (sıcaklık ve bağıl nem) gibi faktörlerden farklı ölçülerde etkilenmektedir. Elde edilen malzemenin mekanik, elektrik, optik, vb. gibi özellikleri, ortalama lif çapına bağlı olarak değişiklik gösterdiğinden, bu faktörlerin ortalama lif çapı üzerindeki etkilerinin belirlenmesi oldukça önemlidir. Bu nedenle; bu çalışmada, kemik doku mühendisliği uygulamalarında kullanılma potansiyeline sahip nanokompozit yapıda bir malzemenin elektrospinning yöntemi kullanılarak hedeflenen lif çapına sahip olarak üretilmesi için istatistiksel bir deney tasarım yönteminin (yanıt yüzey yöntemi gibi) kullanılması amaçlanmıştır.

Yanıt yüzey yöntemi; istatistiksel yöntemlerden yararlanarak, bağımsız değişkenler ile yanıt değişkenleri arasındaki ilişkiyi belirleyen ve deneysel veriyi ampirik bir modele dönüştüren grafiksel bir yöntemdir. Üç ya da daha fazla faktöre sahip ikinci dereceden yanıt yüzey modeli için Box–Benkhen tasarım yöntemi, merkezi kompozit tasarım yöntemine kıyasla daha üstündür. Bu nedenle; Box–Benkhen tasarım yönteminin kullanılması yoluyla malzeme ve proses değişkenlerinin lif çapı üzerindeki etkilerinin incelenmesi hedeflenmiştir.

Bu doktora tezi kapsamında verilen ilk iki makale polimerik yapı iskelelerinin hazırlanması için en uygun çözelti değişkenlerinin belirlenmesini amaçlamıştır. Sonuç olarak; 80–250 nm lif çapına sahip jelatin/poli(ε-kaprolakton) yapı iskeleleri başarılı bir şekilde üretilmiş; polimer konsantrasyonu ve karışım çözeltisindeki jelatin çözeltisi miktarı arttıkça lif çapının arttığı belirlenmiştir. Çözücü bileşiminin ise, lif çapı üzerinde istatistiksel olarak önemli bir etkisi görülmemiştir. Benzer şekilde; 68–166 nm lif çapına sahip jelatin/sodyum aljinat yapı iskeleleri de farklı yüzey morfolojilerine sahip olarak üretilmiştir. Jelatin konsantrasyonu, karışım çözeltisindeki jelatin çözeltisi miktarı ve çözücü içerisindeki asetik asit oranı arttıkça lif çapının arttığı belirlenirken; çözücünün etanol içerip içermemesine bağlı olarak aljinat konsantrasyonunun etkisi farklılık göstermiştir.

Bu iki çalışma vasıtasıyla çözelti değişkenlerinin belirlenmesinin ardından; stronsiyum veya bakır katkılı biyoaktif cam parçacıkları başarıyla jelatin/poli(ε-kaprolakton) yapı iskeleleri içerisine başarıyla dahil edilerek iyon salınımı özelliğine de sahip nanokompozit yapı iskeleleri üretilmiştir. Biyoaktif cam içeriği arttıkça, ortalama lif çapı ve biyoaktivite artmıştır. Ancak, iyon salınımı stronsiyum içeren nanokompozit yapı iskelelerinde 5.4–10.1 mg/g; bakır içeren nanokompozit yapı iskelelerinde 0.34–1.87 mg/g olarak tespit edildiğinden; biyoaktif camların SrO ve CuO içeriklerinin yükseltilmesinin yapı iskelelerinin osteojenik, anjiojenik ve antibakteriyel potansiyelini geliştirmek için etkili bir yöntem olabileceği düşünülmektedir.

Bunlara ek olarak; nanokompozit yapı iskelelerinin hazırlanması için en uygun proses değişkenlerinin belirlenmesine yönelik de çalışmalar yürütülmüş olup bu çalışmalar henüz yayınlanmadığı için bu tez kapsamında yer verilmemiştir. Ayrıca, stronsiyum veya bakır iyonu salınımı özelliğine sahip jelatin/sodyum aljinat nanokomposit yapı iskeleleri de başarıyla üretilmiş olup bu çalışmalar da henüz yayınlanmadığı için bu tez içerisinde yer almamıştır.

1. INTRODUCTION

Bone is a dynamic, highly vascularized tissue that transports essential nutrients and oxygen as well as maintaining skeletal integrity [1]. Due to trauma, infection, skeletal disorder, and bone disease, large defects often occurs in bone tissue [2]. Bone tissue engineering offers an effective solution for these large bone defects by repairing, replacing or regenerating the diseased or the damaged tissue with the aid of scaffolds [3–6]. An ideal scaffold for bone tissue engineering should be biocompatible, biodegradable, bioactive, osteoinductive, and osteoconductive, as well as presenting similar mechanical properties compatible with the native bone tissue [7–10]. Although developing an ideal scaffold is challenging, mimicing the physical and the chemical structure of the natural extracellular matrix (ECM) could provide a framework for the design of scaffolds. This is because the architecture and the composition of a scaffold are important in cellular activities, including adhesion, spreading, migration, proliferation, gene expression and cytoskeletal function [11].

Recently, biomaterials in the form of nanoparticles, nanofibers, and nanocomposites have been receiving considerable interest for bone tissue engineering applications in order to physically mimic the native bone ECM [7]. Especially, preparation of ultrafine fibers of diameters ranging from tens of micrometers down to several nanometers has been conducted with the use of electrospinning technique in order to produce scaffolds with desirable properties for bone regeneration [7–8,12]. Electrospinning is a process that allows the fabrication of fibrous matrices having high porosity and large surface area from a wide range of materials [7,11]. In addition, this technique does not require expensive equipments and has low operating costs [7].

Creating an ideal scaffold is challenging since only one material alone cannot meet all the requirements of an ideal scaffold. The ECM of bone is a nanocomposite in which type I collagen fibrils and nanocrystalline hydroxyapatite–like particles are intimately

combined [7,13]. Therefore, one strategy that has been considered to resemble the structure of native bone tissue is composite systems comprising the biodegradable polymer matrix combined with bioactive ceramics through combining the biodegradation and the flexibility of polymers with the bioactivity and the mechanical strength of bioceramics [7,9,14].

Among bioactive ceramics, bioactive glasses are of particular interest, since they can bond firmly with both bone and surrounding tissues by the formation of a hydroxycarbonate apatite layer on the material surface when it is in contact with body fluid [15–17]. Ever since its introduction by Hench et al. [18] in 1971, bioactive glasses in the form of particles, dense solids, and porous scaffolds have been widely researched as a promising choice for biomedical applications, due to their excellent biocompatibility, biodegradability, and osteoconductivity [9,19–20]. As an attempt to maximize their biological activity, bioactive glasses have also been fabricated into various nanostructures, such as nanoparticles, nanofibers, and mesoporous nanofibers [8].

In addition, key for developing an ideal scaffold is the potential biocompatibility of these materials to induce rapid vascular ingrowth (namely angiogenesis), as well as their ability to induce sufficient proliferation of local osteoblasts and endothelial cells [2]. Several approaches have been investigated to enhance or to accelerate the angiogenesis, such as partially combining angiogenic peptides, angiogenic genes and transfected endothelial cells expressing angiogenic peptides, or integrating the growth factors into the scaffolds [1,21]. Nevertheless, all of these methods limit the application of the scaffolds because of the complexity of the methods and the shortcomings related to the growth factors, including expensive prices, safety problems and short halflife [1,21]. Comparing with the foregoing approaches, the simpler, more sustainable and inexpensive strategy to induce angiogenesis is to develop materials that induce angiogenesis [1–2,21]. Therefore, it is of high interest to develop a material with a release ability of therapeutic metallic ions for introducing additional functionalities (i.e., angiogenic and antibacterial effects) into the scaffolds.

Among many therapeutically active ions, strontium has the ability to substitute calcium in the mineral phase of natural bone tissue, which is called “bone seeking behavior” [22–23]. The ability of strontium to remodel bone can be attributed to its dual effect, which is promoting osteoblast-related bone formation while inhibiting osteoclast-related bone resorption [2,21,24–29]. Meanwhile, copper has antibacterial activity, as well as enhancing angiogenesis [30–33].

Within this respective, in the present PhD Dissertation, emphasis has been placed on developing multifunctional scaffolds with enhanced angiogenesis potential and antibacterial properties that have a potential to be used in bone tissue engineering applications. For this purpose, strontium and/or copper substituted nanocomposite fiber mats made of polymeric matrix combined with bioactive glass microparticles are aimed to be fabricated with the use of electrospinning technique. However, natural and synthetic polymers alone cannot meet all the requirements of an ideal scaffold. Generally, natural polymers show superior biocompatibility and cell recognition, while they lose their mechanical properties very early during degradation [34]. On the other hand, synthetic polymers show easier processability and more tunable physical properties, whereas they are less hydrophilic, lack binding sites for cell adhesion and release acidic degradation products [34–35]. To overcome these problems associated with individual polymers, blending two or more polymers has been preferred to assimilate the desirable characteristics of component materials.

Within this context, two natural biopolymers (gelatin and sodium alginate) and a synthetic polymer (poly(ε-caprolactone)) were selected to be employed in the experimental studies. Besides having many merits, such as their biological origin, biodegradability, biocompatibility, non-toxicity, hydrophilicity and commercial availability at relatively low cost, gelatin and sodium alginate bear structural resemblance to collagen and glycosaminoglycan, respectively, which are among the major components of ECMs in human tissue [36–46]. Meanwhile, poly(ε-caprolactone) is a semicrystalline polymer that possesses some unique properties, including biocompatibility, bioresorbability, cheapness and approval by Food and Drug Administration for many of its products [34].

Electrospinning parameters, such as process parameters (i.e., applied voltage, flow rate of the polymer solution, and distance between the needle tip and the collector), solution parameters (e.g., polymer concentration and solvent composition), and ambient conditions (temperature, and relative humidity) affect the average fiber diameter in different extent. Since the resultant fiber diameter determines properties of the electrospun fiber mats such as mechanical, electrical, and optical properties, several studies have been conducted by other researchers to find the extent of the impact of these parameters on average fiber diameter. Most of the studies used one variable-at-a-time technique that is one parameter is changed during the process while keeping the others at a constant level. This approach of optimization is not only time-consuming but also ignores interaction effects of multiple parameters. In order to overcome this problem, optimization can be applied using a statistical experimental design method (i.e., response surface methodology). Within this respective, it was aimed to find the optimum set of parameters for fabricating nanomaterials targeted for bone tissue engineering applications by using response surface methodology based on Box-Behnken design procedure. Since this PhD dissertation aims to design, characterize and investigate a new family of 3D bioactive nanocomposite scaffolds, designing is the most important step of the study. In this context, following sections consist of three published papers that explains the studies performed to achieve these goals.

2. EFFECTS OF ELECTROSPINNING PARAMETERS ON GELATIN/POLY(Ɛ-CAPROLACTONE) NANOFIBER DIAMETER[(*)]

2.1 Introduction

The native extracellular matrix (ECM) is a 3D network of biomacromolecules and serves not only as a structural scaffold but also as an environment directing the actions of tissues and cells [36]. Designing ECM-mimicking artificial matrices or scaffolds that can replace the natural ECM until the seeded cells can produce a new functional matrix and regenerate the diseased or damaged tissue structures, is a key issue in the field of tissue engineering [37,47]. For this purpose, nanofibrous scaffolds have been extensively studied because of their ECM-like topographies.

Among various fabrication methods that have been explored for preparing nanofibrous scaffolds, electrospinning, also called electrostatic fiber spinning, which is a facile, versatile, and cost-effective means in producing continuous fibers from a variety of materials with diameters ranging from several micrometers down to tens of nanometers, has attracted much attention in the past decade [48–50]. Through this process, mostly mats of randomly oriented fibers with large surface-to-volume ratio as well as various fiber morphologies and geometries are obtained [51].

Interest towards employing electrospinning for scaffold fabrication is mainly due to the mechanical, biological, and kinetic properties of the scaffold being easily manipulated by altering the electrospinning parameters that may be divided into two groups: (i) intrinsic parameters, which include intrinsic properties of the polymer solution, i.e., molecular weight, concentration, surface tension, viscosity, conductivity, etc., and the environmental conditions, e.g., temperature, humidity, pressure, etc.; (ii) control parameters, which involve the operating parameters, such as applied voltage, flow rate,

[(*)] This chapter is based on the paper: "**Gönen, S. Ö.**, Erol Taygun, M., and Küçükbayrak, S. (2015). Effects of electrospinning parameters on gelatin/poly(ε-caprolactone) nanofiber diameter: an investigation by Box–Behnken design. *Chemical Engineering & Technology*, *38* (5), 1–8."

distance between the needle and the collector, needle diameter, and collector type [50–52].

The fiber diameter, which is a function of the electrospinning parameters, determines properties of the electrospun fiber mats such as mechanical, electrical, and optical properties [50–51]. Therefore, it is important to have control over the fiber diameter. Despite many studies have been carried out to investigate the influence of these parameters on the resultant fiber diameter [53–60], the role of each parameter in the process has not yet been understood clearly, and contradictory results have been frequently reported when a one-variable-at-a-time technique was used. This may be due to the fact that a change in a given parameter can strongly depend on the values selected for the other parameters [52]. The use of an experimental design-based method can overcome this problem.

Among the different experimental design methods, response surface methodology (RSM) is a graphical methodology that is useful for the statistical modeling and analysis of problems in which a response of interest affected by several variables is aimed to be optimized [61]. This methodology has the advantage of taking into account the combined effects of several parameters and minimizing the number of experiments to optimize a number of factors [62–63]. Till now, several authors have employed RSM in order to establish a quantitative relationship between electrospinning parameters and fiber diameter [50–51,61–62,64–70]. However, the obtained results cannot be generalized for all the polymer/solvent systems since they are highly dependent on the polymer structure and chemistry [71]. To the best of our knowledge, this paper is the first report that investigates the effect of intrinsic parameters related to preparation of polymer blends on the resultant diameter of nanofibers via RSM.

Natural and synthetic polymers alone cannot meet all the requirements of a perfect scaffold. Generally, natural polymers show superior biocompatibility and cell recognition, while they lose their mechanical properties very early during degradation [34]. On the other hand, synthetic polymers offer easier processability and more tunable physical properties, whereas they are less hydrophilic, lack binding sites for cell adhesion, and release acidic degradation products [34–35]. To overcome these problems

associated with individual polymers, electrospinning of blends of two or more polymers, especially synthetic-natural polymeric combinations, have been explored by researchers that assimilate the undesirable characteristics of component materials.

Gelatin, which is a natural biopolymer derived from collagen by controlled hydrolysis, is a heterogeneous mixture of single- or multi-stranded polypeptides containing between 300 and 4000 amino acids [37–38]. Because of its numerous advantages, such as its biological origin, biodegradability, biocompatibility, excellent cell affinity, and commercial availability at relatively low cost, gelatin has been widely used in biomedical applications [36–39]. However, it is also a soft material and has low tensile properties [35]. On the other hand, poly(ϵ-caprolactone) (PCL) is a semicrystalline, biocompatible, bioresorbable, low-cost synthetic polymer, which has been successfully electrospun, and many of the products using this material are approved by the Food and Drug Administration [34]. Although PCL has good mechanical properties, its low hydrophilicity together with a lack of surface cell recognition sites often results in low cell adhesion and proliferation [35,72–73]. Therefore, a combination of PCL and gelatin can yield a potential biomaterial with improved mechanical, physical, chemical, and biological properties.

In this context, some researchers have investigated the potential use of gelatin/PCL nanofibrous scaffolds for various tissue engineering applications, e.g., dental tissue [63], bone tissue [34,74], cardiovascular tissue [37], neural tissue [35,72], skin tissue [39], muscle tissue [75], and cardiac tissue [76–77]. For instance, Zhang et al. [48] reported that bone-marrow stromal cells can attach and grow on the gelatin/PCL or PCL-alone scaffolds, but the cells spread better and migrate deeper inside the gelatin/PCL scaffold. Similarly, Ghasemi-Mobarakeh et al. [72] indicated that nerve cells can attach and grow on PCL/gelatin and PCL nanofibrous scaffolds, but cell proliferation was improved by blending PCL with gelatin. Moreover, the gelatin/PCL fibrous membrane was found to exhibit improved mechanical properties as well as more favorable wettability than that obtained from either gelatin or PCL alone [48].

In electrospinning, the solvent used has a significant influence on the spinnability of a polymer solution [48]. According to the open literature, the most common solvents for

gelatin/PCL blends were fluorinated alcohols, i.e., 2,2,2-trifluoroethanol [35,38,48] and 1,1,1,3,3,3-hexafluoro-2-propanol [37,72,75–77]. However, their cost, possible toxicity issues, and environmental concerns are the disadvantages of these solvents for biomedical applications. As an alternative to the fluorinated alcohols, in this study, a solvent system consists of acetic acid and formic acid was preferred as a relatively cheap and less toxic solvent combination.

The effect of electrospinning parameters on the resultant diameter of gelatin/PCL nanofibers was investigated for the first time by RSM. Since established studies in the literature have reported intrinsic properties of the polymer solution, especially solution concentration, as to be critical [50–52,61–62,65–67], emphasis was given to the effect of concentration-related properties of the polymer solution. Therefore, the individual and interactive effects of four factors, namely, gelatin concentration, PCL concentration, content of acetic acid in the overall solvent, and content of gelatin solution in the blend solution, on the resultant fiber diameter were investigated. A quantitative basis for the relationship between fiber diameter and these parameters was established within the context of RSM based on a three-level, four-variable Box-Behnken design.

2.2 Experimental

2.2.1 Preparation of polymer solution

Gelatin (Gt, type A, from porcine skin) and poly(ϵ-caprolactone) (PCL, Mn = 70 000–90 000) were obtained from Sigma Aldrich and used without further purification. Acetic acid (AcOH) and formic acid were purchased from Merck. Firstly, Gt and PCL solutions were separately prepared by dissolving for 2 h at room temperature in a solvent mixture consisting of acetic acid and formic acid. After that, Gt and PCL solutions were mixed with different weight ratios and stirred for 2 h at room temperature in order to obtain homogeneous Gt/PCL blend solutions.

2.2.2 Electrospinning

The Gt/PCL blend solutions were placed into a syringe/capillary tube connected to a high-voltage source and were electrospun under a constant applied voltage of 20 kV. An

electric field was formed between the grounded collector and the tip of the syringe/capillary tube. The grounded collector was located at a distance of 10 cm. A syringe pump was utilized to form a constant flow rate of 3 mL h^{-1}. Fibers were directly collected on the aluminum foil.

2.2.3 Morphology

The morphology of produced electrospun Gt/PCL fibers was observed by scanning electron microscopy (Jeol JSM-5410) after being platinum-coated. For each experiment, the average fiber diameter was determined from about 75 measurements of the random fibers.

2.2.4 Design of experiment

Investigation of the impact of electrospinning parameters on the resultant fiber diameter requires a number of experiments. The planning and analysis of these experiments were performed within the context of RSM, which follows four sequential steps: (i) screening the independent variables (factors) and their levels; (ii) building the response surface model using an appropriate experimental design method; (iii) estimating the coefficients of the mathematical model; and (iv) assessing the accuracy of the response [64].

The levels of the four electrospinning factors, namely, Gt concentration, PCL concentration, content of AcOH in the overall solvent, and content of Gt solution in the blend solution, were screened based on results from preliminary experiments (data not shown here). The factors and their levels, real values as well as coded values are listed in Table 2.1.

Table 2.1 : Factors and their levels used in the experimental design.

Factors	Symbol	Variable levels		
		-1	0	1
Gt concentration [% w/v]	X_1	10	15	20
PCL concentration [% w/v]	X_2	7	11	15
Content of AcOH in the overall solvent [vol %]	X_3	0	25	50
Content of Gt solution in the blend solution [wt%]	X_4	30	50	70

For a quadratic response surface model with three or more factors, the Box-Behnken design procedure has been reported to be much more advantageous compared to the

central-composite design [64,68–69]. Therefore, a Box-Behnken design procedure was applied to study the response *y*, namely, the average nanofiber diameter. All experiments were carried out in a randomized order to minimize the effect of unexpected variability in the observed response due to extraneous factors. The MINITAB statistical software (Version 16, Minitab Inc., State College, PA) was employed for all statistical computations.

Regression analysis was performed to fit the observed response, i.e., the average fiber diameter, as a function of the electrospinning parameters. The true, but unknown relation between the average fiber diameter and the parameters was approximated by a second-order polynomial model of four variables as Eq. (2.1):

$$y = C_0 + \sum_{i=1}^{4} C_i X_i + \sum_{i=1}^{4} C_{ii} {X_i}^2 + \sum_{i=1}^{3} \sum_{j=i+1}^{4} C_{ij} X_i X_j \qquad (2.1)$$

where *y* is the predicted response value, i.e., the average fiber diameter, X_i is the *i*th independent factor. C_0, C_i, C_{ii}, and C_{ij} are regression coefficients with C_0 being the constant term, C_i the linear effect term, C_{ii} the squared effect term, and C_{ij} the interaction effect term. The quality of fit of the model was evaluated by the coefficients of determination (R^2) and the analysis of variances. The insignificant coefficients were eliminated after examining the coefficients and the model was finally refined. A validation study was also performed by conducting additional experiments to confirm the validity and the accuracy of the response surface model.

2.3 Results and Discussion

2.3.1 Model development

According to the statistical theory, a Box-Behnken design of four factors consists of 27 experiments as indicated in Table 2.2. As it is seen from the results at each design point, the average diameter of Gt/PCL nanofibers varied from 80 to 250 nm depending on the electrospinning conditions. The fabrication of many differently sized Gt/PCL nanofibers has been reported by other researchers in the open literature. Some of them were in the

size of 640–880 nm [37], 232 ± 194 nm [35], 470 ± 120 nm [38], 113–189 nm [72], 343–547 nm [75], 239 ± 37 nm [76], 189 ± 56 nm [77], when fluorinated alcohols were employed as solvents.

Table 2.2 : Box-Behnken design matrix and response values for each design point.

Design point	Coded independent variable levels				Average fiber diameter [nm]	
	X_1	X_2	X_3	X_4	Experimental	Predicted
1	−1	−1	0	0	79 ± 23	69
2	1	−1	0	0	160 ± 28	167
3	−1	1	0	0	144 ± 57	147
4	1	1	0	0	235 ± 64	246
5	0	0	−1	−1	146 ± 35	137
6	0	0	1	−1	140 ± 39	137
7	0	0	−1	1	186 ± 58	178
8	0	0	1	1	220 ± 54	178
9	−1	0	0	−1	121 ± 46	120
10	1	0	0	−1	140 ± 46	153
11	−1	0	0	1	96 ± 48	95
12	1	0	0	1	247 ± 91	260
13	0	−1	−1	0	106 ± 55	118
14	0	1	−1	0	182 ± 52	196
15	0	−1	1	0	91 ± 33	118
16	0	1	1	0	202 ± 69	196
17	−1	0	−1	0	126 ± 53	108
18	1	0	−1	0	239 ± 68	206
19	−1	0	1	0	94 ± 35	108
20	1	0	1	0	231 ± 59	206
21	0	−1	0	−1	108 ± 39	97
22	0	1	0	−1	189 ± 61	178
23	0	−1	0	1	139 ± 38	138
24	0	1	0	1	202 ± 55	217
25	0	0	0	0	145 ± 58	157
26	0	0	0	0	139 ± 53	157
27	0	0	0	0	136 ± 48	157

The summary of the statistics from the experimental data and the regression coefficients of the quadratic response surface model are presented in Table 2.3. The measure of goodness of the fit, R^2, represents the proportion of the total variability that has been explained by the regression model [62]. The R^2 value, roughly around 0.93, illustrates that the model is able to explain 93 % of the variability in the average fiber diameter. However, the predicted R^2 (62.13 %) and the adjusted R^2 (85.67 %) are not close to each

other in a reasonable level. Therefore, the significance of individual and interaction parameters should be checked.

It is known that *p*-values associated with the regression coefficients are statistical measures of significance of the individual parameters in explaining the variability of the fiber diameter [51]. If the *p*-value is less than 0.05, the factor has significant impact on the average fiber diameter, whereas the factor has no significant impact on average fiber diameter when the *p*-value is greater than 0.05 [62]. Since the *p*-values of the Gt concentration (X_1), PCL concentration (X_2), and content of Gt solution in the blend solution (X_4) are below the significance level of 0.05, these factors are significant for the variation of the fiber diameter. Moreover, the interaction term of the Gt concentration and the content of Gt solution in the blend solution (X_1X_4) has also a significant influence on the average fiber diameter. The significance of these four terms is not surprising because they are related to the final concentration of the electrospinning solution, which has been reported to be a significant parameter by other researchers [50–52,61–62,65–67].

Table 2.3 : Regression coefficients for the response surface model using coded values.

Term		Coefficient	*p*-Value	Term		Coefficient	*p*-Value	Summary of fit	
Constant	C_0	140.000	0.000	X_4X_4	C_{44}	12.458	0.153	R^2	93.39 %
X_1	C_1	49.333	0.000	X_1X_2	C_{12}	2.500	0.795	R^2(adj)	85.67 %
X_2	C_2	39.250	0.000	X_1X_3	C_{13}	6.000	0.536	R^2(pred)	62.13 %
X_3	C_3	−0.583	0.916	X_1X_4	C_{14}	33.000	0.004	Regression	
X_4	C_4	20.500	0.003	X_2X_3	C_{23}	8.750	0.371	*p*-Value	0.000
X_1X_1	C_{11}	9.708	0.257	X_2X_4	C_{24}	−4.500	0.641	*F*-Value	12.10
X_2X_2	C_{22}	0.333	0.968	X_3X_4	C_{34}	10.000	0.309	Lack of fit	
X_3X_3	C_{33}	16.083	0.072					*p*-Value	0.048
								F-Value	20.08

However, there is no strong statistical evidence that the coefficients are different from zero as the *p*-values are greater than 0.05 for the content of AcOH in the overall solvent (X_3), all of the second-order terms, and all of the interaction terms except for the interaction term of X_1 and X_3. Since these terms have no significant impact on the average fiber diameter, the response surface model was further refined by deleting the terms which were associated with a level of significance $> 5\,\%$ ($p > 0.05$), and the coefficients of the model with their respective *p*-values were recalculated as listed in Table 2.4.

Table 2.4 : Regression coefficients for the response surface model using coded values after removal of insignificant terms.

Term		Coefficient	*p*-Value	Summary of fit	
Constant	C_0	157.15	0.000	R^2	88.66 %
X_1	C_1	49.33	0.000	R^2(adj)	86.60 %
X_2	C_2	39.25	0.000	R^2(pred)	84.22 %
X_4	C_4	20.50	0.001	Regression	
X_1X_4	C_{14}	33.00	0.002	*p*-Value	0.000
				F-Value	43.01
				Lack of fit	
				p-Value	0.129
				F-Value	2.22

The refined response surface model comprised of terms which are statistically significant at 95 % confidence level ($p \leq 0.05$) is designated as Eq. (2.2):

$$y = 97.4606 - 6.6333\,X_1 + 9.8125\,X_2 - 3.925\,X_4 + 0.33\,X_1X_4 \qquad (2.2)$$

where *y* is the average fiber diameter (nm), X_1 is the Gt concentration (% w/v), X_2 is the PCL concentration (% w/v), and X_4 is the content of Gt solution in the blend solution (wt %).

The error associated with the refined response surface model was evaluated by computing the lack-of-fit that compares the residual error from the model error to the pure error from replicated experiments [71]. A *p*-value of 0.129 associated with the lack-of-fit suggested that the model was statistically significant and the lack-of-fit was insignificant at a 5 % level of significance. This means that the model adequately fits the response surface. Moreover, the predicted R^2 (84.22 %) and the adjusted R^2 (86.60 %) are also in reasonable agreement with the R^2 (88.66 %) in the refined model.

The response surface plot is a theoretical 3D plot that illustrates the relationship between the response and independent variables [70]. The 2D display of the surface plot is called contour plot in which lines of the constant response are drawn in the plane of the independent variables [70]. These plots give useful information about the model fitted. Contour plots and surface plots of the response variable are presented in Figure 2.1 and 2.2, respectively. Each figure visualizes the relationship between the two parameters at the center level of the third parameter.

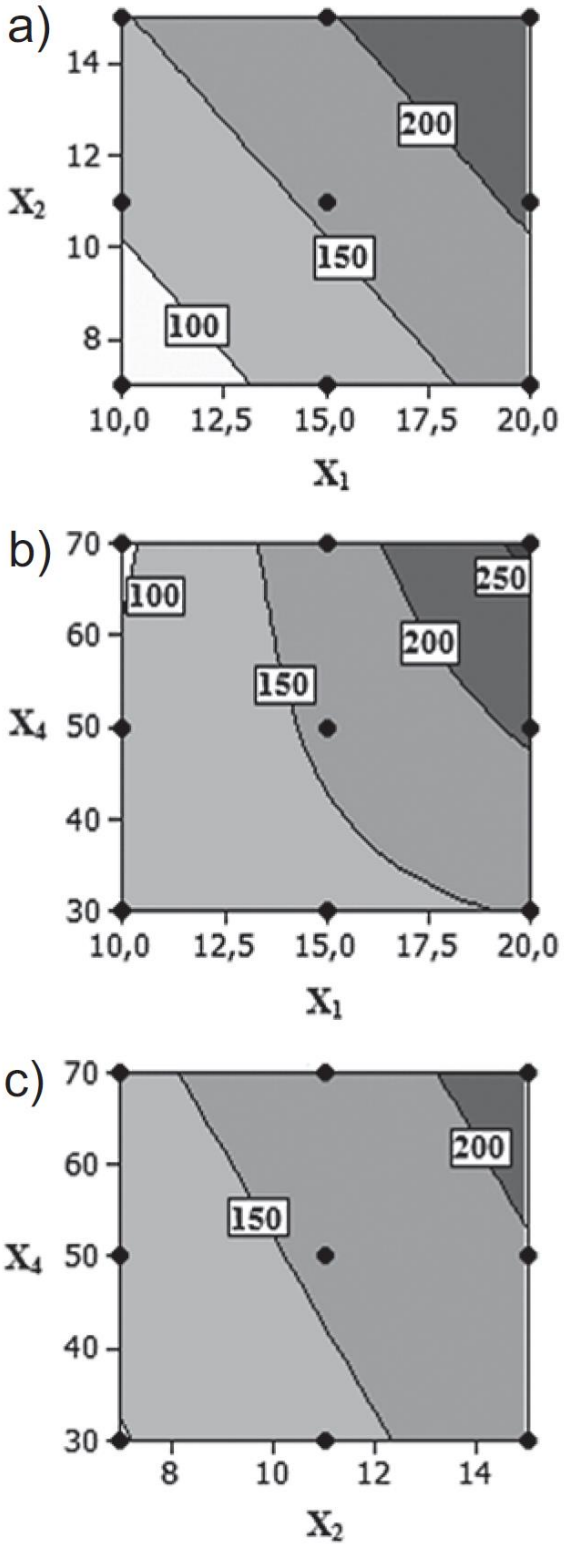

Figure 2.1 : Contour plots of process parameters on fiber diameter.

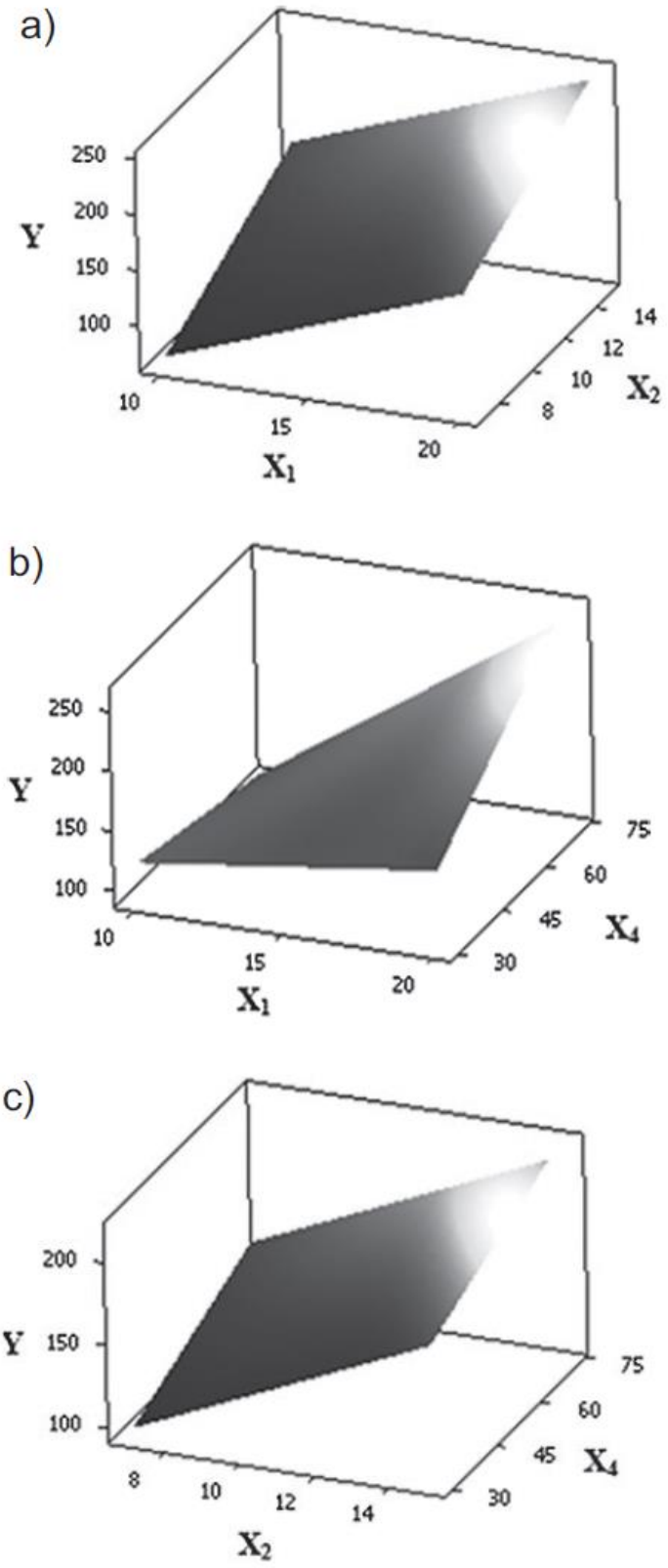

Figure 2.2 : Surface plots of process parameters on fiber diameter.

The contour plot and the 3D surface plot for Gt concentration versus PCL concentration (Figure 2.1(a) and 2.2(a)) demonstrate that increasing the Gt concentration and/or the PCL concentration resulted in a larger fiber diameter. This is not surprising because total polymer concentration in the blend solution rises with the increase in the concentration of one or both of the polymers involved in the blend solution. As previously reported in several other studies [51,62,66], thicker fibers are formed with higher concentration because charges on the electrospinning jet will be able to stretch the polymer solution and thus, the polymer chain.

In addition, the contour plot and the 3D surface plot for Gt concentration versus content of Gt solution in the blend solution (Figure 2.1(b) and 2.2(b)) indicate that the resultant fiber diameter is not responsive to changes in the content of Gt solution in the blend solution when the Gt concentration was low. However, as the Gt concentration increases, it became more responsive to changes in the content of Gt solution in the blend solution. This is because the total polymer concentration in the blend solution does not change significantly with the increase in the content of Gt solution in the blend solution when the Gt concentration was low. Nevertheless, as the Gt concentration rises, the change in the content of Gt solution in the blend solution becomes more important. These results are also consistent with our pre-mentioned results indicating the fact that there is an interaction between these two factors.

Moreover, the contour plot and the 3D surface plot for PCL concentration versus content of Gt solution in the blend solution (Figure 2.1(c) and 2.2(c)) lead to the conclusion that a higher PCL concentration and/or content of Gt solution in the blend solution resulted in a larger fiber diameter. Furthermore, the highest PCL concentration (15 % w/v) coupled with the highest Gt concentration (20 % w/v) and the highest content of Gt solution in the blend solution (70 wt %) resulted in the production of nanofibers with the largest diameter.

2.3.2 Validation of the model

Normalization of the data was done by a normal probability plot. The normal probability plot in Figure 2.3(a) indicates that the errors are normally distributed, as all the points lie close to the line. A normal fit of the probability distribution of residuals verified that the

deviation of the model predictions from the experimental results was random without systematic bias.

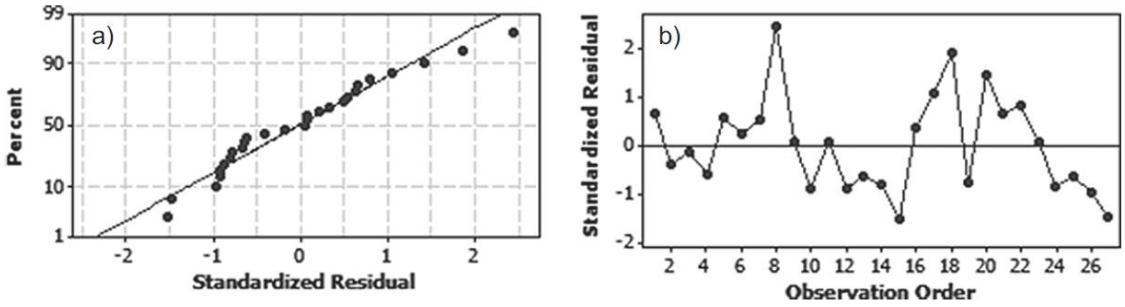

Figure 2.3 : Normal probability and residual plots.

Independency of the data was tested by plotting a graph between the residuals and the run order as given in Figure 2.3(b). The residuals were defined as the difference between the model-predicted value and the experimental outcome at identical factor levels within the design space under consideration. For a well-predicted model, the residuals are expected to follow a normal distribution [64]. Since no predictable pattern was observed and occurrences were random, a well-predicted model was developed in the present study.

To confirm the correlation and significance of Eq. (2.2), the adequacy of the model was examined by additional independent experiments that were not employed in the model generation. The experimental findings as shown in Table 2.5 were in close agreement with the predicted values.

Table 2.5 : Results of model validation experiments.

Trial number	X_1 [% w/v]	X_2 [% w/v]	X_3 [vol %]	X_4 [wt %]	Average fiber diameter [nm]	
					Experimental	Predicted
1	15	11	0	50	168 ± 42	157
2	15	15	50	70	196 ± 46	217
3	20	15	0	70	279 ± 76	299

2.4 Conclusions

In order to use the electrospinning process as a tool for producing materials with targeted fiber diameter for different applications, it was aimed to develop a simple method for predicting the diameter of electrospun Gt/PCL fibers from knowledge of the

electrospinning parameters. Gt/PCL nanofibers with diameters ranging from 80 to 250 nm were produced depending on the electrospinning condition. A quadratic model was obtained within the context of RSM based on a three-level, four-variable Box-Behnken design technique to describe the relationship between the fiber diameter and the electrospinning parameters, namely Gt concentration (10–20 %, w/v), PCL concentration (7–15 %, w/v), content of AcOH in the overall solvent (0–50 vol %), and content of Gt solution in the blend solution (30–70 wt %). Consequently, a simple and effective method for fabricating Gt/PCL nanofibers having a controllable and predictable fiber diameter was developed. Based on these data, Gt/PCL nanofibrous scaffolds can be fabricated conveniently for tissue engineering applications with desired properties. Moreover, the potential use of the as-prepared nanofibers as scaffolds for bone tissue engineering applications is still under investigation.

3. EVALUATION OF THE FACTORS INFLUENCING THE RESULTANT DIAMETER OF THE ELECTROSPUN GELATIN/SODIUM ALGINATE NANOFIBERS VIA BOX–BEHNKEN DESIGN(*)

3.1 Introduction

Electrospinning is a simple, versatile, and cost-effective technique by which fibrous mats with diameters ranging from several microns down to a few nanometers can be fabricated from both synthetic and natural polymers for biomedical applications, including tissue engineering scaffolds, wound dressing pads, and drug delivery platforms [51,62,70,78–87]. In the last decade, this technique has gained much attention because of its various outstanding properties, such as its versatility in processing various kinds of materials, ability to control the diameter and morphology of fibers, ease of operation, and low setup cost of required devices [57,88]. Especially in tissue engineering field, there is an increasing interest toward employing electrospinning for scaffold fabrication because of the similarity of electrospun nanofibrous mats to fibrils of extracellular matrices (ECMs) in both dimensions and morphology [57,89]. Owing to their features, such as very small fiber diameters, large surface area per mass ratio, and high porosity along with small pore size, electrospun nanofibrous matrices support cellular activities and function better than their microscale counterparts [90–92].

Fine tune of the microstructure and diameter of fibers is very crucial since they eventually determine the characteristics of electrospun fibrous mats such as physical, mechanical, biological, electrical, and optical properties [51,69,80,82,93]. The morphology and diameter of electrospun fibers depend on many parameters which are mainly divided into four categories: polymer properties (i.e., type and molecular weight), solution properties (e.g., polymer concentration and solvent composition), processing conditions (i.e., applied voltage, tip to collector distance, flow rate, and

(*) This chapter is based on the paper: "**Gönen, S. Ö.**, Erol Taygun, M., and Küçükbayrak, S. (2016). Evaluation of the factors influencing the resultant diameter of the electrospun gelatin/sodium alginate nanofibers via Box–Behnken design. *Materials Science and Engineering: C, 58*, 709–723."

needle diameter), and ambient parameters (e.g., temperature, atmosphere pressure, and relative humidity) [62,79–83,94]. These parameters affect the morphology and diameter of fibers in different extent. In order to find the extent of the impact on fiber diameter, considerable effort has been devoted to understand the effect of parameters, including molecular weight [51], polymer concentration [51,62,66–67,78–81,88,93–95], electric field [78], applied voltage [51,62,66–67,70,79–83,88,94–95], tip to collector distance [51,66–67,69–70,78–80,83,88,93], and flow rate [66–67,69–70,80,82–83,88,93].

When several factors affect a response of the system, the most extensively used strategy is the one-factor-at-a-time approach, which means one factor is changed while keeping the others constant [80]. However, this approach fails to consider any possible interaction between the factors. On the other hand, response surface methodology enables us to simultaneously investigate the individual factors and their interactions with each other by combining mathematical and statistical techniques to fit an empirical model to the experimental data [62,70,78,82]. Therefore, response surface methodology is a simple and systematic way of describing the relationship between a set of controllable input variables and observed response [83,93]. In this context, this methodology allows for analyzing the effects of electrospinning parameters on the fiber diameter and predicting the electrospinning conditions to fabricate fibrous mats with targeted diameter. Hence, a number of studies have focused on using response surface methodology to present the influence of electrospinning parameters on the fiber diameter of various materials, such as silk [78,95], polyacrylonitrile [51,62,79,96], poly(D,L-lactide) [81], poly(L-lactide) [97], polyvinyl alcohol [80], poly(vinyl pyrrolidone) [88], polymethyl methacrylate [93], cellulose acetate [69], zein [66], starch [67], titanium dioxide [70], chitosan/polylactide [82], polyacrylonitrile/poly(vinylidene fluoride) [94], chitosan/polyvinyl alcohol [83], and gelatin/poly(ε-caprolactone) [98].

The synthesis of natural polymer-based nanofibers is of interest because of their many outstanding properties, including biological origin, biocompatibility, biodegradability, hydrophilicity, commercial availability, renewability, and cost efficiency [90–92]. Among natural polymers, sodium alginate is a linear polysaccharide copolymer that bears structural resemblance to glycosaminoglycan, one of the major components of ECMs in human tissue [41,90–92,99]. It has been extensively studied in the field of

tissue engineering, including the regeneration of skin, cartilage, bone, liver, and cardiac tissue [41–42,90–92,100–103]. However, previous studies have shown that aqueous solutions of sodium alginate do not form fibers through electrospinning [40,91–92,100,104]. To overcome the problem regarding electrospinning of sodium alginate, various strategies has been adopted, such as incorporating a copolymer (i.e., polyethylene oxide [40,90–92,103–105] and polyvinyl alcohol [40,43,106]) sometimes with the use of surfactants (e.g., Triton X-100 [90–92, 104–105], pluronic F127 [104], and lecithin [103]) and/or cosolvents (i.e., dimethyl sulfoxide [90–91,105] and glycerol [100]) to the alginate solution. Although synthetic polymers have tunable mechanical properties and degradation kinetics, cell affinity toward synthetic polymers is generally poor because of low hydrophilicity and lack of recognition sites for integrin-mediated cellular adhesion [72,107]. Therefore, the present study focused on blending sodium alginate with a natural polymer that shows superior biocompatibility and cell recognition, in order to facilitate spinnability of this polymer.

To date, previous researchers have shown the potential use of gelatin/sodium alginate-based materials for biomedical applications, including drug delivery [108–109], wound healing [110–112], and tissue engineering [113–114]. Being a denatured collagen, gelatin has almost identical composition and biological properties as those of collagen, which is the most abundant structural protein found in animal body and one of the most important constituents of ECMs [56–57,84,115]. In particular, its biological origin allows gelatin to promote cellular activities, including cellular attachment, proliferation, and differentiation [116]. Therefore, it was hypothesized that combining gelatin and sodium alginate could enhance the biological properties of the biomaterial. Published data also strengthened this hypothesis. For instance, Pawar et al. [113] reported that the incorporation of gelatin promoted the length of axon outgrowth within the alginate-based hydrogels. Similarly, Graulus et al. [114] indicated that increasing the gelatin content of hydrogels improved cell adhesion and proliferation. Within this respect, gelatin was employed as the copolymer of sodium alginate in this study.

To the best of our knowledge, no systematic study has been reported to establish a quantitative basis for the relationships between the electrospinning parameters and the diameter of gelatin/sodium alginate nanofibers. Therefore, the main objective of the

present work was to develop an empirical model within the context of response surface methodology for statistically investigating the significance of the individual factors and their interactions, as well as providing a prediction capability for the process conditions to achieve fibrous mats with targeted diameter. The solution properties, in particular viscosity, has been reported to have much greater impact on the diameter and morphology of electrospun fibers compared to the processing conditions [66–67]. Thus, emphasis was given to the effect of viscosity related parameters. Within this respect, gelatin concentration, alginate concentration, and content of alginate solution in the blend solution were selected as governing parameters due to their role on determining total polymer concentration, whereas content of acetic acid in the solvent of gelatin solution and presence of ethanol in the blend solution were preferred for their effect on overall solvent composition.

Box–Behnken design is a type of response surface design that consists of combinations at the midpoints of the edges of the experimental space. Since it does not have axial points, Box–Behnken design ensures that all of the design points fall within safe operating zone. Moreover, it has fewer design points than central composite design with the same number of factors. Therefore, Box–Behnken design is often more advantageous for a quadratic response surface model with three or more factors when compared to central composite design [69,98]. Hence, in the present study, response surface methodology based on a three-level, four-variable Box–Benkhen design was employed for understanding how the variations in solution properties affect the fiber diameter and its standard deviation when the blend solutions of gelatin and sodium alginate were electrospun both in the absence and presence of ethanol. In addition, regression analysis was performed to develop empirical models representing the fiber diameter and its standard deviation as a function of the solution properties. By means of these models, gelatin/sodium alginate nanofibers with targeted diameter can be fabricated to be used in the field of tissue engineering.

3.2 Materials and Methods

3.2.1 Materials

Gelatin (type A, from porcine skin) and sodium alginate (alginic acid sodium salt from brown algae) were obtained from Sigma–Aldrich Chemicals. Ethanol and glacial acetic acid were purchased from Merck. All chemicals were used as provided without further purification.

3.2.2 Preparation of polymer solutions

Gelatin solutions with concentrations of 10%–20% (w/v) were first prepared by dissolving in 40%–80% (v/v) acetic acid aqueous solutions at room temperature for 2 h. Meanwhile, sodium alginate was dissolved in deionized water at room temperature for 24 h to obtain the alginate solutions with concentrations of 0–2 wt%. Afterward, gelatin and alginate solutions were mixed at different volumetric ratios both in the absence and presence of ethanol. The content of ethanol in the overall blend solution was 10% (v/v) for the system with ethanol.

3.2.3 Electrospinning

The blend solutions, which were transferred into a 5 mL syringe, was delivered via a syringe pump to maintain a steady flow of the solution at 3 mL/h. Electrospinning was conducted under a constant applied voltage of 20 kV. Randomly oriented electrospun fibers were collected on a grounded plate wrapped with aluminum foil, which was placed at a distance of 10 cm from the syringe tip. All electrospinning experiments were performed at ambient conditions.

3.2.4 Morphology

The surface topography and fiber diameter of the as-spun fibrous mats were determined with the aid of a scanning electron microscope (SEM, Jeol JSM-5410). Prior to imaging, a small section of the samples cut from the fibrous mats was sputter coated with platinum by using an SC7620 sputter coater (Quorum Technologies Ltd, United Kingdom) for 120 s. For each experiment, the average fiber diameter and its standard

deviation were analyzed by the help of an image visualization software (Image-J, National Institute of Health, USA) from about 50 measurements of the random fibers.

3.2.5 Design of experiment

Response surface methodology is a suitable tool to develop numerical models, to measure the influence of variables, and to select the optimum combinations of variables [69]. This approach follows five steps: (1) selecting variables and their levels, (2) choosing suitable experimental design and performing statistically designed experiments, (3) developing a mathematical model with the application of regression analysis to the experimental data, (4) determining the accuracy of the model, and (5) verifying the adequacy of the model [69,83,94].

To follow the steps of response surface methodology, variables to be considered in the design of experiment should first be selected. However, the number of variables influencing on the electrospinning process are large. Therefore, it is impossible to study all of them in the framework of one single research. In the open literature, it was demonstrated that the solution properties, in particular viscosity has much greater impact on the diameter and morphology of electrospun fibers than that of the processing conditions [66–67]. For instance, Khanlou et al. [93] reported that the fiber diameter is more reliant on polymer concentration in comparison with tip to collector distance and flow rate. Similarly, Li et al. [88] found that the fiber diameter is more responsive to polymer concentration compared to applied voltage and tip to collector distance. Moreover, Maleki et al. [97] indicated that the fiber diameter is predominantly affected by polymer concentration and to a lesser extent by applied voltage. Furthermore, some researchers determined that applied voltage has no significant effect on the fiber diameter [81,88,94], as well as its standard deviation [81,94]. Therefore, only the parameters affecting the viscosity of the blend solutions were examined, while the processing conditions and the ambient conditions were held constant during experiments.

The relationship between viscosity and polymer concentration is highly depended on the nature of polymer (e.g., molecular structure and molecular weight) and the intermolecular interactions within polymer solution (i.e., polymer–polymer and

polymer–solvent) [89]. Therefore, concentration of both polymers, ratio of one polymer to another polymer in the blend, and solvent type were selected as variables.

The choice of a suitable solvent for a polymer is fundamental for the electrospinning process. Cytotoxic organic solvents, such as hexafluoroisopropanol [117] and trifluoroethanol [45,48,84], have been employed for electrospinning of gelatin. However, it is very difficult to completely remove these solvents from the resultant scaffolds due to their ability to form strong hydrogen bonds with gelatin [116]. To avoid the use of organic solvents, electrospinning of gelatin aqueous solutions has also been studied [118]. Nevertheless, water is not appropriate for this purposesince gelatin becomes a kind of a colloidal sol when dissolved in water at a temperature below 30°C [84,118]. Although electrospinning of gelatin got easier as the temperature was increased from 35 to 50°C, the thermal degradation of gelatin at high temperatures limited the electrospinnability of gelatin aqueous solution in a narrow temperature window and at a very low rate [116,118]. In addition, water cannot be volatilized as quickly as enough to coagulate the gelatin solution [96]. Besides, its extremely high surface tension (~ 74.2 mN/m) also contributes to the poor spinnability of gelatin aqueous solution [119]. Hence, searching for an alternative organic solvent plays a key role in successfully electrospinning of this biopolymer. For this reason, some carboxylic acids (e.g., formic acid [56–57,86] and acetic acid [86–87,89]) have also been investigated as less cytotoxic solvents for electrospinning of gelatin. However, the acid-induced partial degradation of gelatin molecules can be occurred due to strong acidity [56,116]. Therefore, Ki et al. [56] examined the stability of gelatin solution in formic acid by means of measuring viscosity. They reported that gelatin solution was stable at least for 5 h at 25°C in the concentration range of 8%–12%. It was also noted that spinnability and morphology of gelatin nanofiber was not altered after storing the solutions for 24 h in spite of degradation of gelatin molecules. Moreover, it was found that the degradation time of gelatin in acetic acid was longer than that it was in formic acid because of acetic acid being a weaker acid than formic acid (cf. $K_{a,\ \text{acetic acid}} \approx 1.8 \times 10^{-5}$versus $K_{a,\ \text{formic acid}} \approx 1.7 \times 10^{-4}$) [46,56]. Therefore, acetic acid was decided to be used in the present study. Nevertheless, Erencia et al. [89] pointed out that acetic acid aqueous solutions behaved like a good solvent for gelatin (i.e., cause coils to

expand), while pure acetic acid interacted as a theta solvent for gelatin (e.g., cause coils to contract). Moreover, it was hypothesized that the introduction of water into the acidic solvent can decrease the acidity of the solvent and thus, prolongs the time required for degrading gelatin. Hence, a mixture of acetic acid with water was selected as the solvent material for gelatin. The levels of gelatin concentration and content of acetic acid in the solvent of gelatin solution were determined according to the published data [46,86–87,89,99] and the preliminary studies (data not shown). Furthermore, it was proposed that the introduction of ethanol into the solvent could speed up the volatilization of water, reduce the acidity of the solvent, and decrease the surface tension of gelatin solution. Hence, the blend solutions were prepared both in the absence and presence of ethanol to compare the effect of addition of ethanol into the system. The content of ethanol in the overall solution was selected as 10% (v/v) based on the preliminary studies (data not shown).

On the other hand, water has generally been used for dissolving sodium alginate. However, it was reported that aqueous solutions of sodium alginate started to gelate at very low polymer concentrations (e.g., ca. 2 wt%), above which solutions became too viscous to be injected by the electrostatic forces, even at high voltages [40,91]. For this reason, the concentration of sodium alginate solution was chosen to be in the range of 0–2 wt%. Meanwhile, the level of content of sodium alginate solution in the blend solution was determined by the preliminary studies (data not shown).

After the selection of variables and their levels, codification was further performed by transforming the real value of each variable into coordinates within a scale with dimensionless values. Thereby, the potential impact of greater variables on the assessment of the variables with lesser value was eliminated [69]. Table 3.1 shows the coded and uncoded level of each variable.

Table 3.1 : Factors and their levels used in the experimental design.

Factors	Symbol	Levels		
		-1	0	1
Gelatin concentration (% w/v)	X_1	10	15	20
Alginate concentration (wt%)	X_2	0	1	2
Content of alginate solution in the blend solution (vol%)	X_3	10	20	30
Content of acetic acid in the solvent of gelatin solution (vol%)	X_4	40	60	80

As indicated before, a response surface methodology based on a three-level, four-variable Box–Benkhen design was utilized to establish empirical relationships between two responses (average fiber diameter and its standard deviation) and four solution properties (gelatin concentration, alginate concentration, content of alginate solution in the blend solution, and content of acetic acid in the solvent of gelatin solution). The experimental design contained 27 experimental runs including three replicates at the center point. All experiments were performed in a random order.

Regression analysis was performed to fit the responses as a function of the solution properties. First-order models are unable to capture the interaction between parameters. Therefore, a second-order model was adopted in this study, as given in Eq. (3.1):

$$y = C_0 + \sum_{i=1}^{4} C_i X_i + \sum_{i=1}^{4} C_{ii} {X_i}^2 + \sum_{i=1}^{3} \sum_{j=i+1}^{4} C_{ij} X_i X_j \qquad (3.1)$$

where y is the predicted response value and X_i is the ith independent factor. C_0, C_i, C_{ii}, and C_{ij} are the regression coefficients with C_0 being the constant term, C_i being the linear effect term, C_{ii} being the squared effect term, and C_{ij} being the interaction effect term.

Regression and graphical analysis of the obtained data were carried out using Minitab 16.0 statistical software (Minitab Inc., State College, PA, USA). The accuracy of the models was evaluated by the coefficients of determination (R^2) and the analysis of variances (ANOVA). The relative importance of each term in the models was determined from the t-values and associated p-values. Coefficients with p-values less than 0.05 were considered statistically significant. The models were further refined by deleting the statistically insignificant terms ($p > 0.05$). The validity of the models was evaluated by conducting eight additional experiments inside the design space. Contour plots were depicted to help visualize the relationship between two parameters at the center level of the other parameters.

3.3 Results and Discussion

3.3.1 Development of response surface models

According to the statistical theory, a Box–Behnken design of four factors consists of 27 experiments as shown in Table 3.2. As observed from the results at each design point, the average diameter of gelatin/sodium alginate nanofibers were in the ranges of 68–166 nm and 90–155 nm, depending on the electrospinning conditions in the absence and presence of ethanol, respectively. The morphology of the obtained nanofibers varied from poor to excellent. However, Kong and Ziegler [67] reported that the poor fibers are obtained by mechanisms other than true electrospinning and, thus, should not be included in the model construction. Therefore, results of runs 9 and 19 were eliminated for the system without ethanol, while results of runs 9 and 10 were not utilized for the system with ethanol. Afterward, the coefficients of the response surface models with their respective *p*-values were calculated as given in Table 3.3.

The models can be more efficient with the exclusion of one or more variables. Therefore, the *p*-value of each term in the models was evaluated to determine the statistically insignificant terms. The *p*-value represents the statistical measure of significance level of the individual parameters [51]. When the *p*-value is less than 0.05, the factor has significant impact on the response at a confidence interval of more than 95% [66,93]. Otherwise, the factor has no significant impact on the response [62,81,95]. In order to get refined models, the statistically insignificant terms ($p > 0.05$) were deleted from the full quadratic models. After eliminating the insignificant terms, the mathematical expressions that represent the relationships between the fiber diameter and the solution properties were obtained for the systems without and with ethanol as shown in Eqs. (3.2) and (3.3), respectively.

$$y = 174.371 - 12.255X_1 - 45.667X_2 - 7.623X_3 - 1.693X_4 - 0.37{X_1}^2 \\ -0.294X_1X_3 - 0.164X_1X_4 - 0.725X_2X_4 - 0.06X_3X_4 \tag{3.2}$$

$$y = 105.521 + 4.62X_1 + 1.917X_2 - 2.062X_3 - 1.152X_4 + 0.201{X_3}^2 \\ +0.0231{X_4}^2 - 0.15X_1X_3 - 0.0688X_3X_4 \tag{3.3}$$

where y is the average fiber diameter (nm), X_1 is the gelatin concentration (% w/v), X_2 is the alginate concentration (wt. %), X_3 is the content of alginate solution in the blend solution (vol%), and X_4 is the content of acetic acid in the solvent of gelatin solution (vol%).

Table 3.2 : Summary of the experimental and predicted findings for each design point.

Design point	Coded levels of factors				Average fiber diameter (nm)			
	X_1	X_2	X_3	X_4	Experimental	Predicted	Experimental	Predicted
1	− 1	− 1	0	0	101 ± 17	107 ± 16	90 ± 18	92 ± 16
2	1	− 1	0	0	133 ± 43	135 ± 41	104 ± 20	109 ± 18
3	− 1	1	0	0	96 ± 27	103 ± 26	98 ± 16	96 ± 14
4	1	1	0	0	118 ± 28	131 ± 27	115 ± 17	112 ± 16
5	0	0	− 1	− 1	79 ± 12	96 ± 19	112 ± 28	117 ± 29
6	0	0	1	− 1	108 ± 18	112 ± 14	134 ± 27	136 ± 24
7	0	0	− 1	1	120 ± 25	132 ± 28	155 ± 41	155 ± 36
8	0	0	1	1	101 ± 24	100 ± 23	122 ± 31	119 ± 31
9	− 1	0	0	− 1	68 ± 12	116 ± 23	113 ± 17	99 ± 31
10	1	0	0	− 1	113 ± 25	111 ± 22	104 ± 14	115 ± 11
11	− 1	0	0	1	103 ± 19	95 ± 18	111 ± 16	109 ± 15
12	1	0	0	1	166 ± 49	155 ± 46	135 ± 41	125 ± 40
13	0	− 1	− 1	0	120 ± 32	116 ± 24	130 ± 24	125 ± 25
14	0	1	− 1	0	120 ± 28	112 ± 22	139 ± 28	129 ± 23
15	0	− 1	1	0	107 ± 18	108 ± 20	112 ± 18	117 ± 20
16	0	1	1	0	101 ± 13	104 ± 18	121 ± 18	120 ± 18
17	− 1	0	− 1	0	99 ± 13	94 ± 17	107 ± 15	111 ± 19
18	1	0	− 1	0	155 ± 36	152 ± 42	135 ± 34	142 ± 37
19	− 1	0	1	0	103 ± 15	116 ± 25	121 ± 29	118 ± 30
20	1	0	1	0	113 ± 23	114 ± 26	119 ± 18	119 ± 17
21	0	− 1	0	− 1	130 ± 18	121 ± 18	116 ± 18	105 ± 18
22	0	1	0	− 1	101 ± 18	87 ± 16	105 ± 14	109 ± 16
23	0	− 1	0	1	99 ± 25	103 ± 27	110 ± 24	115 ± 25
24	0	1	0	1	128 ± 26	128 ± 24	107 ± 17	119 ± 23
25	0	0	0	0	110 ± 22	110 ± 21	98 ± 16	102 ± 20
26	0	0	0	0	108 ± 21	110 ± 21	102 ± 22	102 ± 20
27	0	0	0	0	115 ± 16	110 ± 21	106 ± 21	102 ± 20

Table 3.3 : Regression coefficients for the response surface model using coded values.

Term		Without ethanol						With ethanol					
		Average fiber diameter*			Standard deviation**			Average fiber diameter[#]			Standard deviation[##]		
		Coefficient	*t*-value	*p*-value	Coefficient	*t*-value	*p*-value	Coefficient	*t*-value	*p*-value	Coefficient	*t*-value	*p*-value
Constant	C_0	111.000	17.162	0.000	19.6667	6.934	0.000	102.000	21.162	0.000	19.6667	9.114	0.000
X_1	C_1	14.024	3.459	0.006	7.1071	3.998	0.003	7.125	2.414	0.036	1.3750	1.041	0.323
X_2	C_2	− 2.167	− 0.670	0.518	− 1.0833	− 0.764	0.463	1.917	0.795	0.445	− 1.0000	− 0.927	0.376
X_3	C_3	− 4.198	− 1.175	0.267	− 2.4734	− 1.579	0.145	− 4.083	− 1.694	0.121	− 2.4167	− 2.240	0.049
X_4	C_4	5.659	1.585	0.144	4.5504	2.905	0.016	4.917	1.767	0.108	3.4028	2.731	0.021
X_1X_1	C_{11}	8.726	1.606	0.139	6.3512	2.666	0.024	0.458	0.118	0.908	0.3472	0.200	0.845
X_2X_2	C_{22}	− 0.488	− 0.098	0.924	2.6369	1.202	0.257	0.208	0.057	0.956	− 3.9236	− 2.381	0.039
X_3X_3	C_{33}	− 2.785	− 0.549	0.595	− 1.1983	− 0.539	0.602	20.208	5.489	0.000	5.9514	3.611	0.005
X_4X_4	C_{44}	1.023	0.202	0.844	1.1864	0.533	0.605	9.458	2.442	0.035	4.4722	2.579	0.027
X_1X_2	C_{12}	− 2.500	− 0.446	0.665	− 6.2500	− 2.544	0.029	0.750	0.180	0.861	− 0.2500	− 0.134	0.896
X_1X_3	C_{13}	− 13.907	− 1.927	0.083	− 5.0797	− 1.605	0.139	− 7.500	− 1.797	0.103	− 7.5000	− 4.013	0.002
X_1X_4	C_{14}	17.022	2.359	0.040	6.8489	2.165	0.056	4.875	0.739	0.477	11.1250	3.765	0.004
X_2X_3	C_{23}	− 1.500	− 0.268	0.794	− 0.2500	− 0.102	0.921	0.000	0.000	1.000	− 1.0000	− 0.535	0.604
X_2X_4	C_{24}	14.500	2.589	0.027	0.2500	0.102	0.921	2.000	0.479	0.642	− 0.7500	− 0.401	0.697
X_3X_4	C_{34}	− 12.000	− 2.142	0.058	− 1.7500	− 0.712	0.492	− 13.750	− 3.294	0.008	− 2.2500	− 1.204	0.256

* R^2 = 84.8% and R^2 adjusted = 63.5%.
** R^2 = 87.5% and R^2 adjusted = 69.9%.
[#] R^2 = 87.4% and R^2 adjusted = 69.7%.
[##] R^2 = 90.3% and R^2 adjusted = 76.7%.

In the meantime, the mathematical expressions representing the relationships between the standard deviation and the solution properties were obtained for the systems without and with ethanol as given in Eqs. (3.4) and (3.5), respectively.

$$y = 57.008 - 6.71X_1 + 17.667X_2 + 1.646X_3 - 0.835X_4 + 0.251{X_1}^2 - 1.25X_1X_2 - 0.124X_1X_3 + 0.071X_1X_4 \quad (3.4)$$

$$y = 124.856 - 3.41X_1 + 7.004X_2 - 0.341X_3 - 2.794X_4 - 4.002{X_2}^2 + 0.0587{X_3}^2 + 0.0108{X_4}^2 - 0.15X_1X_3 + 0.111X_1X_4 \quad (3.5)$$

where *y* is the standard deviation (nm).

The predicted responses calculated by using these four mathematical models were tabulated in Table 3.2. The calculated values were in agreement with the corresponding experimental results for fiber diameter and its standard deviation, suggesting that the model was accurate.

To confirm the accuracy of the models, the coefficient of determination (R^2) was investigated. R^2 is a statistical measure of how well the experimental data fit the model [97]. It represents the proportion of the total variability that has been explained by the regression model [62,81,94]. However, when a new term is added to the model, R^2 increases regardless of whether the additional term is statistically significant or not [80]. To take this into account, the adjusted form of R^2 is defined to be a more accurate measure than R^2 [97]. R^2 adjusted provides a more useful tool for comparing the models with different number of terms, since it increases only if the additional term improves the model [80]. When R^2 of the refined (Table 3.4) and unrefined models (Table 3.3) were compared, R^2 values were found to decrease slightly for the refined models. This was expected because the refined models consist of fewer terms due to the exclusion of statistically insignificant terms. However, R^2 adjusted increased after the elimination of the insignificant terms, implying that the refined models have the ability to better explain the experimental data. That is to say simpler models that present the experimental data in superior form were obtained by deleting the insignificant terms.

Table 3.4 : Regression coefficients for the refined model using coded values.

Term		Without ethanol						With ethanol					
		Average fiber diameter*			Standard deviation**			Average fiber diameter[#]			Standard deviation[##]		
		Coefficient	*t*-value	*p*-value	Coefficient	*t*-value	*p*-value	Coefficient	*t*-value	*p*-value	Coefficient	*t*-value	*p*-value
Constant	C_0	109.800	44.956	0.000	21.067	18.461	0.000	102.429	44.271	0.000	Constant	C_0	109.800
X_1	C_1	13.958	4.174	0.001	6.667	4.267	0.001	8.100	3.731	0.002	X_1	C_1	13.958
X_2	C_2	− 2.167	− 0.793	0.440	− 1.083	− 0.849	0.408	1.917	0.967	0.348	X_2	C_2	− 2.167
X_3	C_3	− 3.927	− 1.320	0.207	− 2.104	− 1.513	0.150	− 4.083	− 2.060	0.056	X_3	C_3	− 3.927
X_4	C_4	5.865	1.971	0.067	4.479	3.222	0.005	4.964	2.228	0.041	X_4	C_4	5.865
X_1X_1	C_{11}	9.242	2.232	0.041	6.267	3.239	0.005	–	–	–	X_1X_1	C_{11}	9.242
X_2X_2	C_{22}	–	–	–	–	–	–	–	–	–	X_2X_2	C_{22}	–
X_3X_3	C_{33}	–	–	–	–	–	–	20.071	7.200	0.000	X_3X_3	C_{33}	–
X_4X_4	C_{44}	–	–	–	–	–	–	9.250	3.238	0.005	X_4X_4	C_{44}	–
X_1X_2	C_{12}	–	–	–	− 6.250	− 2.828	0.012	–	–	–	X_1X_2	C_{12}	–
X_1X_3	C_{13}	− 14.719	− 2.490	0.025	− 6.187	− 2.240	0.040	− 7.500	− 2.185	0.044	X_1X_3	C_{13}	− 14.719
X_1X_4	C_{14}	16.406	2.775	0.014	7.062	2.557	0.021	–	–	–	X_1X_4	C_{14}	16.406
X_2X_3	C_{23}	–	–	–	–	–	–	–	–	–	X_2X_3	C_{23}	–
X_2X_4	C_{24}	14.500	3.066	0.008	–	–	–	–	–	–	X_2X_4	C_{24}	14.500
X_3X_4	C_{34}	− 12.000	− 2.537	0.023	–	–	–	− 13.750	− 4.005	0.001	X_3X_4	C_{34}	− 12.000

* R^2 = 83.7% and R^2 adjusted = 74.0%.
** R^2 = 83.8% and R^2 adjusted = 75.6%.
[#] R^2 = 86.4% and R^2 adjusted = 79.5%.
[##] R^2 = 88.4% and R^2 adjusted = 81.4%.

For measuring the deviation of the responses from the refined models, the *p*-value of each model was evaluated. The *p*-values of the refined models being below 0.05 implied that there is a little chance that such a small *p*-value could occur due to noise. On the other hand, the error associated with the refined models was evaluated by computing the lack-of-fit, which compares the residual error (from model error) to the pure error (from replicated experiments) [97–98]. The *p*-values associated with the lack-of-fit being above 0.05 (Table 3.5) suggested that the lack-of-fit of each model was insignificant.

Table 3.5 : Summary of the ANOVA results for the refined model.

	Without ethanol				With ethanol			
	Average fiber diameter		Standard deviation		Average fiber diameter		Standard deviation	
	F-value	*p*-value	*F*-value	*p*-value	*F*-value	*p*-value	*F*-value	*p*-value
Regression	8.59	0.000	10.31	0.000	12.66	0.000	12.70	0.000
Linear	4.95	0.010	6.37	0.003	6.02	0.004	4.66	0.012
Square	4.98	0.041	10.49	0.005	28.89	0.000	14.85	0.000
Interaction	7.06	0.002	6.11	0.006	10.41	0.001	19.00	0.000
Lack-of-Fit	7.79	0.119	2.02	0.381	3.22	0.262	1.09	0.576

To validate the adequacy of the obtained models, eight additional experiments that were not employed in the model generation but staying inside the design space, were conducted for each case. The predicted values were found to be reasonably close to the corresponding experimental findings, which confirmed the validity and the adequacy of the models (Table 3.6).

Table 3.6 : Results of the validation experiments.

Trial Number	Uncoded levels of factors				Average fiber diameter (nm)			
	X_1	X_2	X_3	X_4	Experimental	Predicted	Experimental	Predicted
1	15	0	20	60	100 ± 15	112 ± 22	104 ± 20	101 ± 17
2	15	2	20	60	101 ± 27	108 ± 20	111 ± 21	104 ± 15
3	15	1	20	40	111 ± 27	104 ± 17	115 ± 26	107 ± 21
4	15	1	20	80	127 ± 36	116 ± 26	147 ± 32	117 ± 28
5	15	1	30	60	115 ± 23	106 ± 19	103 ± 28	118 ± 23
6	10	1	20	60	120 ± 25	105 ± 21	85 ± 15	94 ± 19
7	20	1	10	80	218 ± 47	186 ± 54	196 ± 61	170 ± 56
8	20	2	10	80	203 ± 62	198 ± 47	206 ± 63	172 ± 51

3.3.2 Influence of solution properties on surface topography

3.3.2.1 Effect of gelatin concentration

For evaluating the effect of gelatin concentration, the electrospinning was performed with different gelatin concentrations varying from 10% to 20% w/v. The morphological structures of electrospun blend nanofibers were shown in Figure 3.1, 3.2, and 3.3. As depicted from figures, many beads as well as droplets were formed at low gelatin concentration (10% w/v) regardless of the level of other three solution properties. However, the beads either reduced or disappeared when the gelatin concentration was increased to 20% w/v. The change in fiber morphology can probably be attributed to a competition between surface tension and viscosity. The surface tension tends to reduce surface area per unit mass and, thus, favors the formation of beads or spheres, while cohesive nature of high viscosity solution resists the formation of beads and allows for the formation of bead-free fibers [62,67,95]. Therefore, when an electric field is applied to a polymer solution with low concentration, solvent evaporation from the initially formed droplet leads to a reduction in its diameter and the charge density of droplet surface is increased [62,95]. With the increase in the charge density, columbic explosion occurs at the Rayleigh limit, the point at which the magnitude of the charge density is sufficient to overcome the surface tension holding a droplet together and cause the droplet to split into smaller droplets [95]. However, as the concentration is increased to a critical value, bead formation reduces and is finally eliminated, supporting the formation of more uniform and smooth fibers instead of bead structures [62,95]. Therefore, concentration of a polymer solution is a key factor in the electrospinning process, since it determines whether the jet breaks up into droplets, beads, or fibers. On the other hand, fiber diameter increased with the gelatin concentration, which is consistent with the observations of other researchers [56–57,85,87,116,118]. This was explained by the higher viscosity being resisted the extension of the jet.

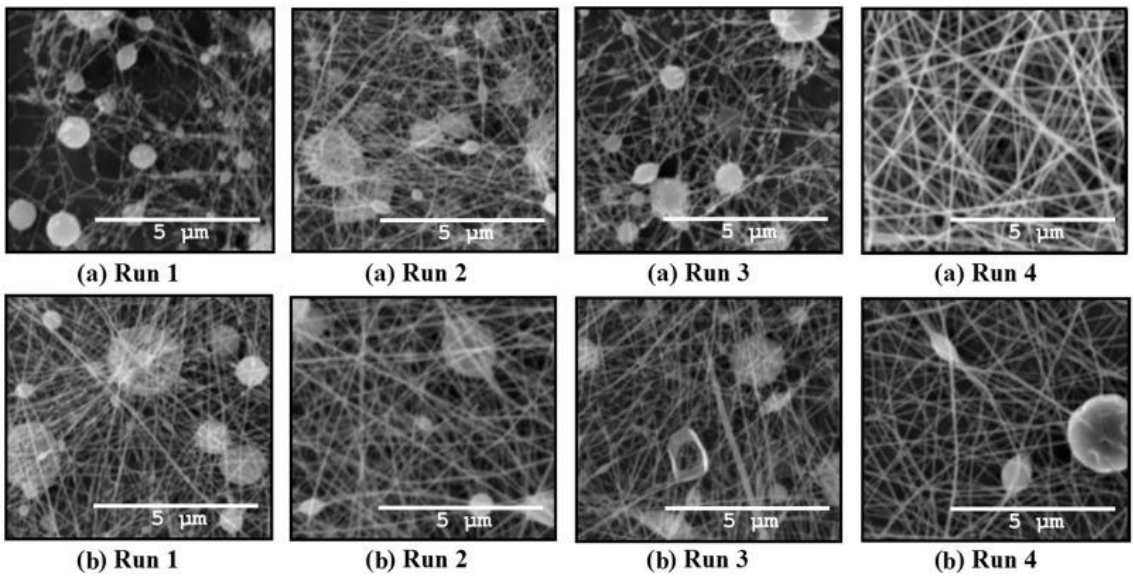

Figure 3.1 : Representative SEM images showing the interaction between gelatin concentration and alginate concentration in the (a) absence and (b) presence of ethanol.

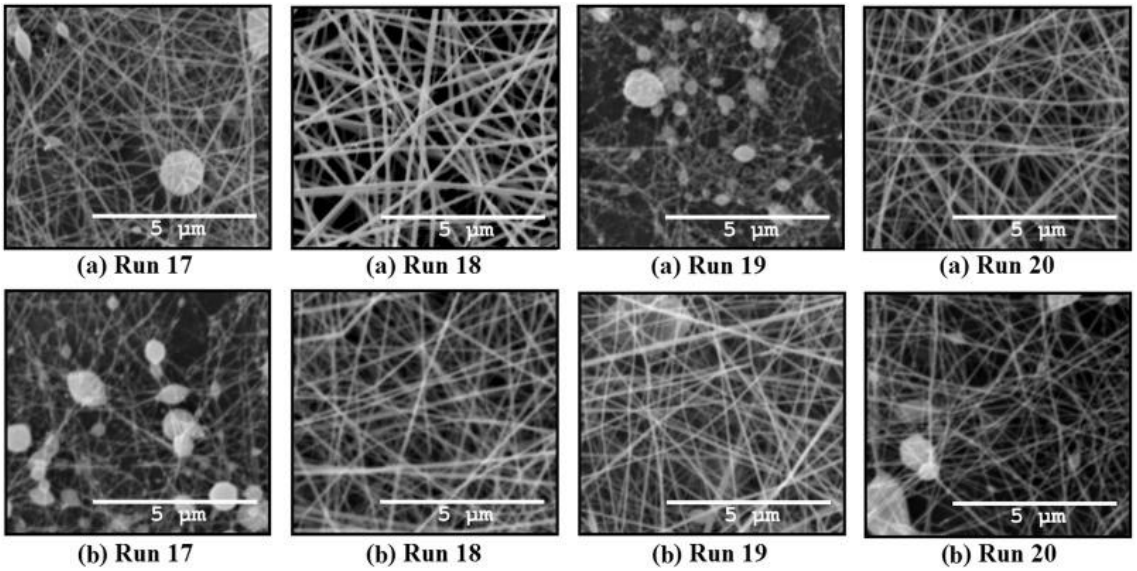

Figure 3.2 : Representative SEM images showing the interaction between gelatin concentration and content of alginate solution in the (a) absence and (b) presence of ethanol.

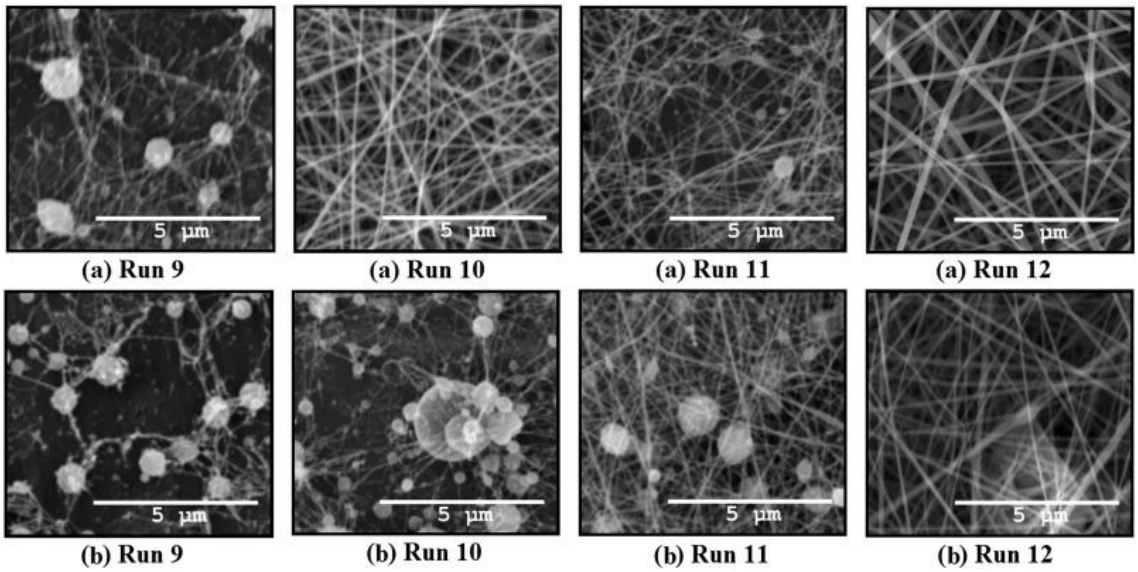

Figure 3.3 : Representative SEM images showing the interaction between gelatin concentration and content of acetic acid in the (a) absence and (b) presence of ethanol.

3.3.2.2 Effect of alginate concentration

In order to determine the effect of alginate concentration, the electrospinning was conducted with different alginate concentrations ranging from 0 to 2 wt%. The morphological structures of electrospun blend nanofibers were shown in Figure 3.1, 3.4, and 3.5. As observed from figures, beaded or bead-free fibers were obtained at low alginate concentration (0 wt%), while the bead formation was minimized or eliminated at high alginate concentration (2 wt%). Similarly, Moon and Farris [99] indicated that the electrospun gelatin/sodium alginate nanofibers with better morphology were produced at lower gelatin concentration compared to the gelatin nanofibers since the viscosity and conductivity of solutions increased with the introduction of alginate into the gelatin solution. In addition, with the increase of alginate concentration from 0 to 2 wt%, the average diameter of the electrospun gelatin fibers was reported to increase from 277 to 347 nm, whereas the morphology of the fibers transformed from beaded to bead-free structure. Meanwhile, the fibers obtained in the present study were in the range of 68–166 nm, which are thinner than that of the fibers in the study of Moon and Farris [99].

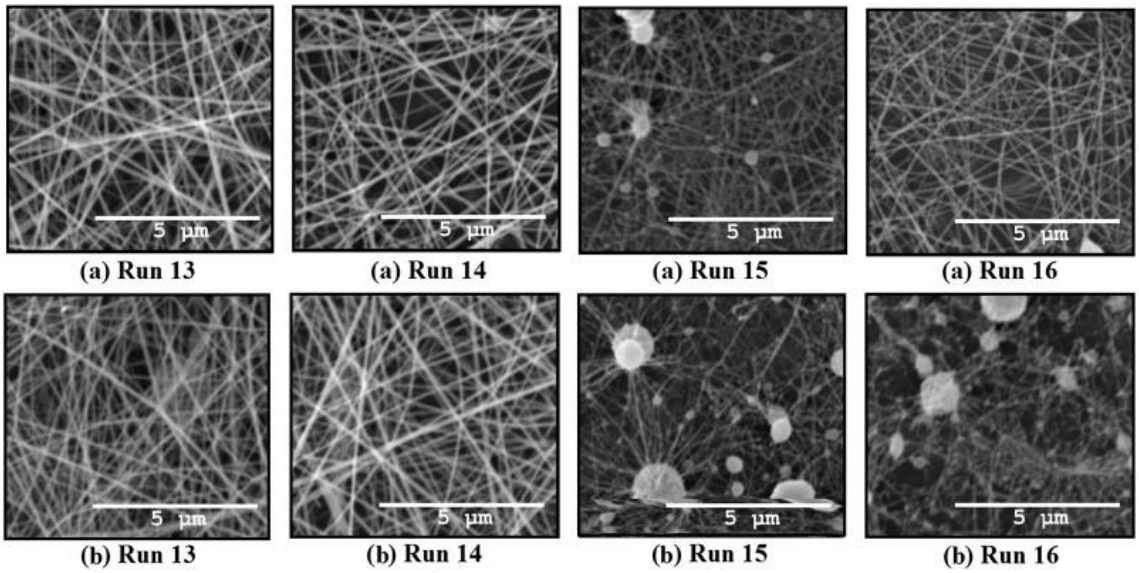

Figure 3.4 : Representative SEM images showing the interaction between alginate concentration and content of alginate solution in the (a) absence and (b) presence of ethanol.

3.3.2.3 Effect of content of alginate solution

For investigating the effect of content of alginate solution, the electrospinning was employed with different contents of alginate solution varying from 10 to 30 vol%. The morphological structures of electrospun blend nanofibers were given in Figure 3.2, 3.4, and 3.6. As depicted from figures, beaded or beadless fibers were formed at low content of alginate solution (10 vol%). However, the beads were appeared or increased as the content of alginate solution was increased to 30 vol%. This can be attributed with the competition between surface tension and viscosity. The reason is the content of gelatin solution in the blend solution decreases when the content of alginate solution is increased. Therefore, total polymer concentration in the blend solution reduces. With the decrease in concentration, viscosity of the solution reduces, favoring the formation of beads.

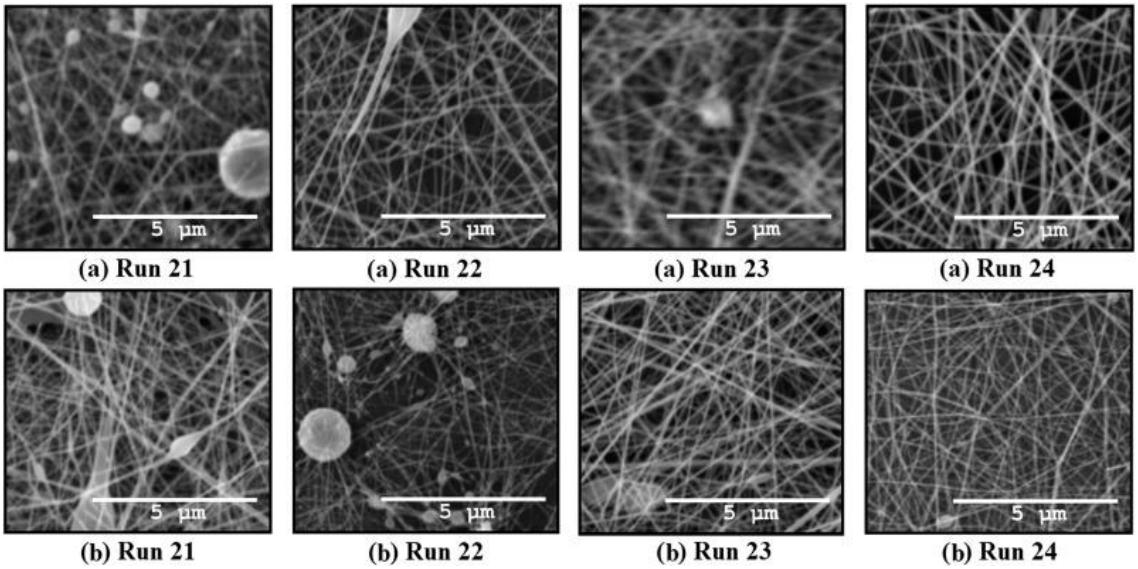

Figure 3.5 : Representative SEM images showing the interaction between alginate concentration and content of acetic acid in the (a) absence and (b) presence of ethanol.

3.3.2.4 Effect of content of acetic acid

To assess the effect of content of acetic acid, the electrospinning was carried out with different contents of acetic acid ranging from 40 to 80 vol%. The morphological structures of electrospun blend nanofibers were given in Figure 3.3, 3.5, and 3.6. As observed from figures, fibers with beads-on-string or bead-free structures were formed at low content of acetic acid (40 vol%). However, the beads were reduced or disappeared with increasing the content of acetic acid to 80 vol%. This can be explained by the competition between surface tension and viscosity, which is because the viscosity increasing with the content of acetic acid. For instance, Songchotikunpan et al. [86] reported that viscosity increased from 0.47 to 0.83 Pa.s as the content of acetic acid was increased from 40 to 80 vol%. Therefore, the formation of fibers is favored with the increase in viscosity.

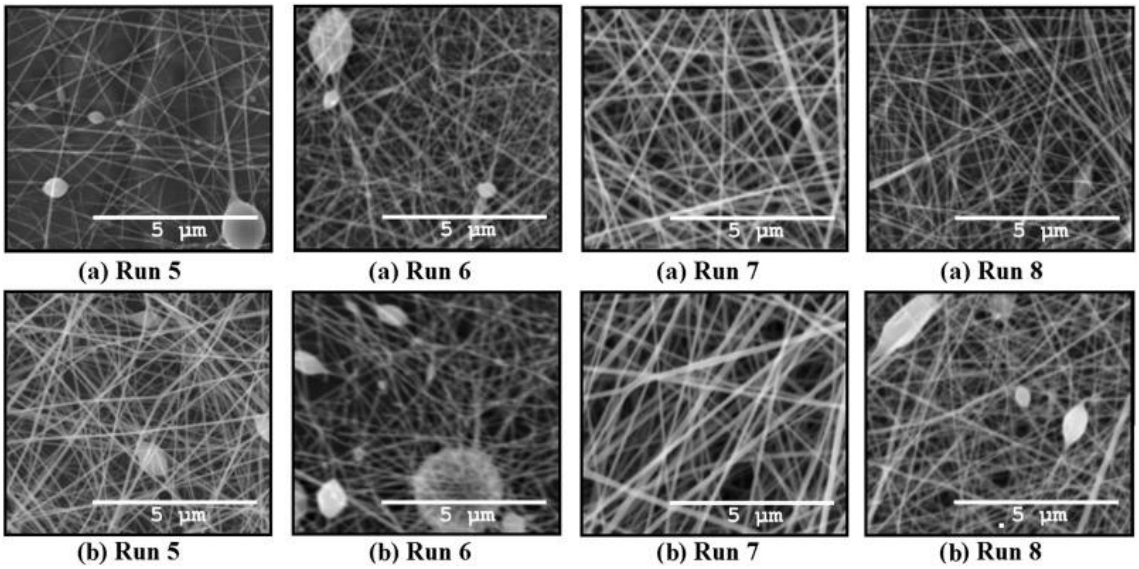

Figure 3.6 : Representative SEM images showing the interaction between content of alginate solution and content of acetic acid in the (a) absence and (b) presence of ethanol.

3.3.3 Influence of solution properties on fiber diameter

The surface plot is a theoretical 3D plot that shows the relationship between response and independent variables, while the 2D display of the surface plot is called contour plot [70]. To obtain an overall impression on the influence of the solution properties on the fiber diameter, to predict the fiber diameter for a new experimental condition inside the design space, and to find the experimental condition that yields the optimum fiber diameter, contour plots illustrated in Figure 3.7 and 3.8 are used.

3.3.3.1 Effect of gelatin concentration

The influence of gelatin concentration on fiber diameter is presented in Figure 3.7(a)–(c). As depicted in these figures, higher gelatin concentration leads to fibers with thicker diameter when one or more of the other solution properties are kept constant. However, the effect of gelatin concentration on fiber diameter becomes negligible at high contents of alginate solution and low contents of acetic acid. The increase in fiber diameter is logical because viscosity increases with concentration. Nevertheless, the content of gelatin solution in the blend solution decreases with an increase in the content of alginate solution, causing the impact of gelatin concentration on viscosity to decrease. This is why the sensitivity of the fiber diameter to the variations in the gelatin

concentration reduces. On the other hand, Songchotikunpan et al. [86] reported that as the content of acetic acid was increased from 40 to 80 vol%, viscosity increased from 0.47 to 0.83 Pa.s, while the conductivity of gelatin solution decreased from 1.76 to 0.77 $mS.cm^{-1}$. Therefore, the formation of fibers with thicker diameter is favored with the increase in content of acetic acid due to the combined effect of the increase in viscosity and the decrease in conductivity. However, increasing gelatin concentration increase both viscosity and conductivity. For instance, Songchotikunpan et al. [86] determined that as the content of gelatin concentration was increased from 15% to 20% w/v, viscosity increased from 0.47 to 1.10 Pa.s, while the conductivity of gelatin solution increased from 1.76 to 1.82 $mS.cm^{-1}$. Similarly, Choktaweesap et al. [85] reported that viscosity of gelatin solution increased from 0.11 to 0.40 Pa.s, while conductivity increased from 0.16 to 0.25 $mS.cm^{-1}$ with rising the gelatin concentration from 15% to 21% w/v. As a result, when the effect of conductivity is more dominant than that of viscosity, the increase in alginate concentration induces the production of thinner fibers. Otherwise, fiber diameter increases with alginate concentration. In the light of these results, it is obvious that gelatin concentration has interactions with content of alginate solution and content of acetic acid, which agrees with the existence of terms X_1X_3 and X_1X_4 in the model of fiber diameter.

Meanwhile, the effect of gelatin concentration on fiber diameter is also investigated after the addition of ethanol into the blend solution. As observed in Figure 3.8(a)–(c), increasing gelatin concentration brings about fibers with thicker diameter when one or more of the other solution properties are kept constant. However, the impact of gelatin concentration on fiber diameter becomes negligible at high contents of alginate solution. This means that the interaction between gelatin concentration and content of acetic acid disappears in the existence of ethanol. Moreover, it is also obvious that fibers with thinner diameter are obtained with the addition of ethanol into the blend solution. This could be explained by the partially replacement of blend solution with ethanol, leading to a decrease in viscosity due to the decrease in total polymer concentration. Moreover, Chen et al. [115] determined that gelatin aqueous solution containing 2 wt% formic acid and 20 wt% ethanol had a lower conductivity (12.5 $mS.cm^{-1}$) than that without ethanol (13.8 $mS.cm^{-1}$) and, thus, favored the formation of fibers with thinner diameter.

Therefore, the decrease in conductivity is also likely the other reason for the decrease in fiber diameter.

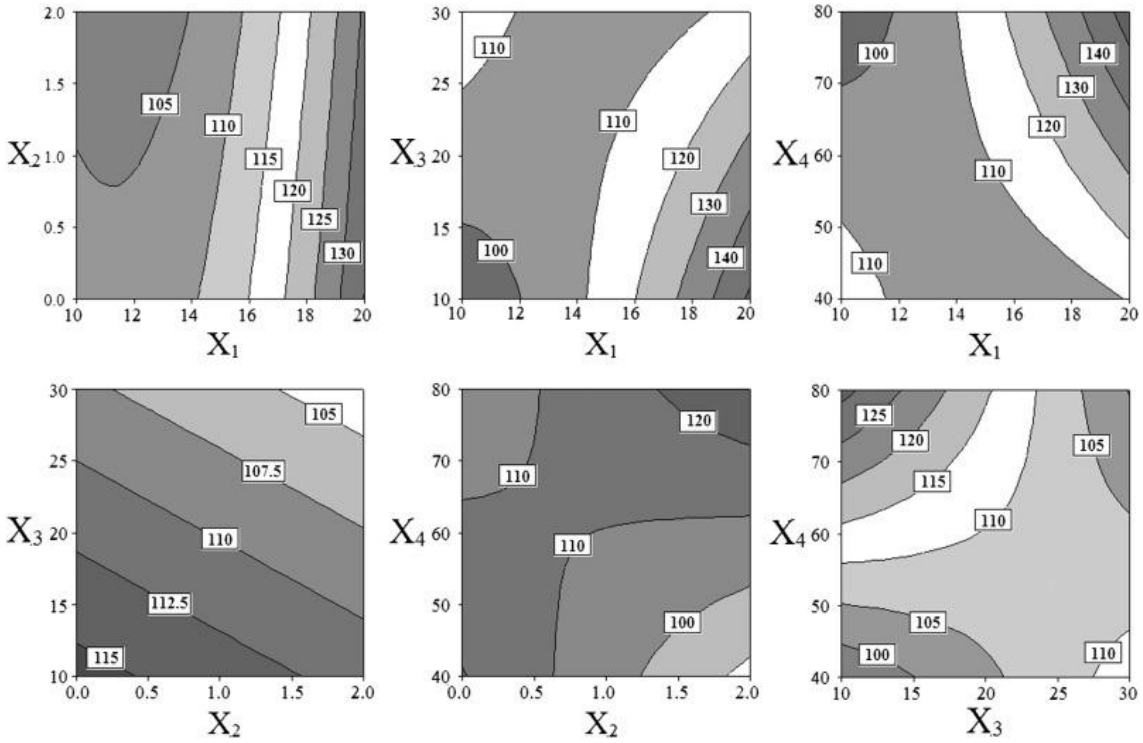

Figure 3.7 : Contour plots of solution properties on fiber diameter in the absence of ethanol.

3.3.3.2 Effect of alginate concentration

The influence of alginate concentration on fiber diameter is shown in Figure 3.7(a), (d), and (e). As demonstrated in these figures, the effect of alginate concentration is not always the same. When gelatin concentration and/or content of alginate solution are kept constant, increasing alginate concentration reduces the fiber diameter slightly, which is likely due to a competition between conductivity and viscosity. Moon et al. [41] reported that as the alginate concentration was increased from 1% to 2% w/v, the conductivity of alginate aqueous solution increased from 2.60 to 4.34 $mS.cm^{-1}$. Similarly, Shalumon et al. [42] determined that viscosity of alginate aqueous solution increased from 0.045 to 0.064 Pa.s, while conductivity increased from 2.39 to 3.36 mS with rising the alginate concentration from 1% to 2%. Accordingly, conductivity and viscosity increase with alginate concentration. In general, higher viscosity and lower conductivity tend to yield fibers with thicker diameter. Therefore, the effect of conductivity is more dominant than

that of viscosity since the fiber diameter decreases with increasing alginate concentration.

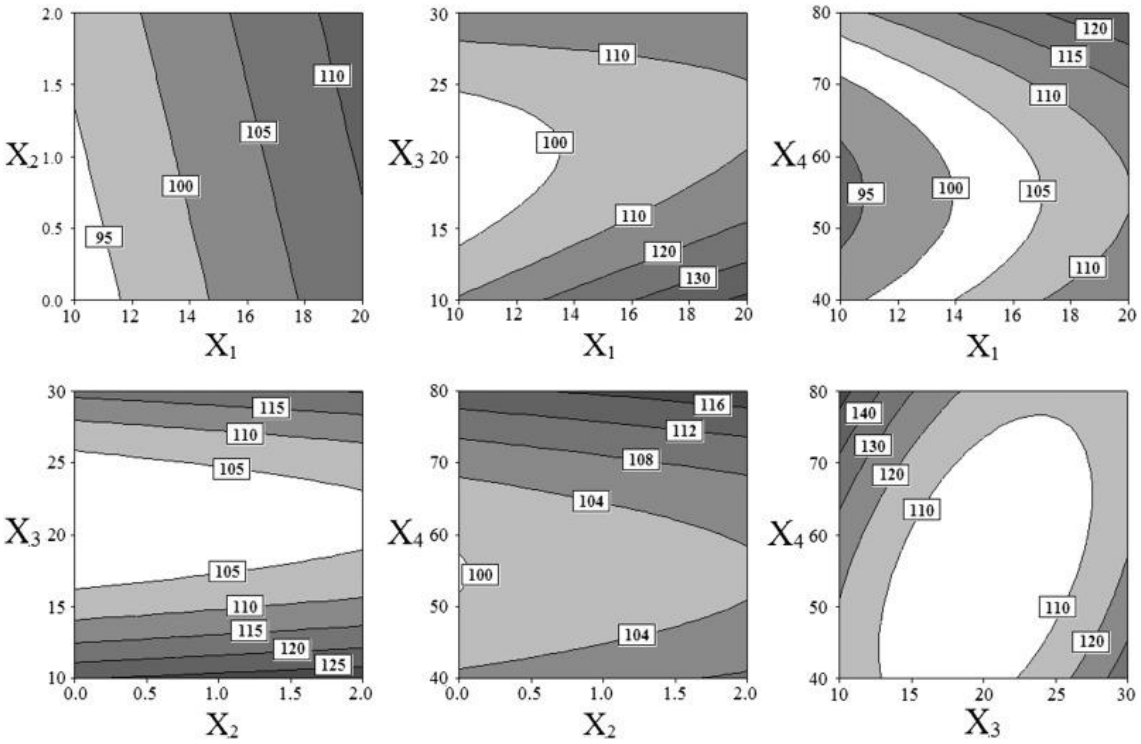

Figure 3.8 : Contour plots of solution properties on fiber diameter in the presence of ethanol.

On the other hand, the effect of alginate concentration on fiber diameter is dramatically influenced by content of acetic acid. At low contents of acetic acid, higher alginate concentration leads to the formation of thinner fibers, whereas at high contents of acetic acid, the effect of alginate concentration is totally reversed and fibers with thicker diameters are obtained as the alginate concentration increases. This is likely resulting from the competition between conductivity and viscosity. As mentioned before, fiber diameter decreases with increasing content of acetic acid due to the combined effect of the increase in viscosity and the decrease in conductivity. However, increasing alginate concentration increases both viscosity and conductivity. Therefore, the competition between conductivity and viscosity determines how the fiber diameter will respond to simultaneous variations in alginate concentration and content of acetic acid. Hence, it is quite apparent that there is an interaction between alginate concentration and content of

acetic acid, which is in agreement with the presence of term X_2X_4 in the model of fiber diameter.

In the meantime, the impact of alginate concentration on fiber diameter is also studied after the addition of ethanol into the blend solution. As depicted in Figure 3.8(a), (d), and (e), increasing alginate concentration brings about fibers with thicker diameter regardless of the other solution properties. Thus, alginate concentration had no interaction with the other solution properties, which proves the absence of terms X_1X_2, X_2X_3, and X_2X_4 in the model of fiber diameter. In the light of these results, it is also obvious that the effect of alginate concentration is totally reversed and the interaction between alginate concentration and content of acetic acid becomes insignificant after the addition of ethanol into the blend solution. This could be explained by the partially replacement of blend solution with ethanol, leading to a decrease in viscosity and conductivity. This means that the effect of viscosity is more dominant than that of conductivity after the inclusion of ethanol into the blend solution.

3.3.3.3 Effect of content of alginate solution

The influence of content of alginate solution on fiber diameter is given in Figure 3.7(b), (d), and (f). As observed in these figures, the fiber diameter is responsive to the changes in content of alginate solution but its effect depends on the level of gelatin concentration and content of acetic acid. For instance, at low gelatin concentrations and low contents of acetic acid, higher content of alginate solution leads to the formation of thicker fibers, whereas at high gelatin concentrations and high contents of acetic acid, the effect of content of alginate solution is totally reversed and fibers with thinner diameters are obtained as the content of alginate solution increases. In addition, the sensitivity of fiber diameter to the changes in the content of alginate solution accelerates at high gelatin concentrations and high contents of acetic acid. Therefore, in agreement with existence of the terms X_1X_3 and X_3X_4 in the model of fiber diameter, content of alginate solution is found to have interactions with gelatin concentration and content of acetic acid. On the other hand, increasing content of alginate solution brings about a decrease in the fiber diameter regardless of alginate concentration, suggesting that there is no interaction

between these two parameters. This result is also in agreement with the absence of the term X_2X_3 in the model of fiber diameter.

As mentioned before, the viscosity of gelatin solution increases with gelatin concentration and/or content of acetic acid. Therefore, the viscosity of two polymer solutions becomes more different than each other as the gelatin concentration and/or content of acetic acid increases. This is likely the reason for fiber diameter being more responsive to the changes in content of alginate solution at high gelatin concentrations and high contents of acetic acid. On the other hand, conductivity increases with increasing polymer concentration and decreasing content of acetic acid, while increasing polymer concentration and/or content of acetic acid yield more viscous solutions. Therefore, the competition between conductivity and viscosity controls the variations in fiber diameter. When the effect of conductivity is more dominant than that of viscosity, the increase in alginate concentration induces the production of thinner fibers. Otherwise, fiber diameter increases with alginate concentration.

Meanwhile, the impact of content of alginate solution on fiber diameter is also investigated after the addition of ethanol into the blend solution. As demonstrated in Figure 3.8(b), (d), and (f), keeping the other solution properties constant, an increase in the content of alginate solution decreases fiber diameter until a threshold limit. However, as the content of alginate solution exceeds a limit, fiber diameter increases with the content of alginate solution. In addition, high gelatin concentrations and high contents of acetic acid accelerate the impact of content of alginate solution on fiber diameter. Moreover, the threshold limit for the content of alginate solution increases at high gelatin concentrations, low alginate concentrations, and high contents of acetic acid. Therefore, it can be concluded that the content of alginate solution has interactions with gelatin concentration and content of acetic acid, which is consistent with the existence of terms X_1X_3 and X_3X_4 in the model of fiber diameter.

3.3.3.4 Effect of content of acetic acid

The influence of content of acetic acid on fiber diameter is presented in Figure 3.7(c), (e), and (f). As depicted in these figures, the effect of content of acetic acid is not always the same. For instance, at low alginate concentrations and/or high contents of alginate

solution, higher content of acetic acid leads to the formation of thinner fibers, whereas at high alginate concentrations and/or low contents of alginate solution, the effect of content of acetic acid is totally reversed and fibers with thinner diameters are obtained as the content of acetic acid increases. Moreover, fiber diameter increases with the content of acetic acid when gelatin concentration is kept constant. In addition, the sensitivity of fiber diameter to the changes in the content of acetic acid gains momentum at high polymer concentrations (both gelatin and alginate) and low contents of alginate solution. This means that the effect of content of acetic acid on fiber diameter is altered by other three solution properties, implying the interaction of content of acetic acid with these parameters, which agrees with the presence of the terms X_1X_4, X_2X_4, and X_3X_4 in the model of fiber diameter.

On the other hand, the impact of content of acetic acid on fiber diameter is also studied after the addition of ethanol into the blend solution. As observed in Figure 3.8(c), (e), and (f), the effect of content of acetic acid is depended on the other three solution properties. Keeping the concentration of one or both polymer constant, an increase in the content of acetic acid reduces the fiber diameter until a threshold limit. However, as the content of acetic acid exceeds a limit, fiber diameter rises with the content of acetic acid. On the other hand, the effect of content of acetic acid on fiber diameter was influenced by the content of alginate solution. Increasing the content of acetic acid leads to thinner fibers at high contents of alginate solution, while fibers with thicker diameter are obtained as the content of acetic acid increases at low contents of alginate solution. This observation proves the interaction between content of acetic acid and content of alginate solution, which is consistent with the existence of term X_3X_4 in the model of fiber diameter.

As discussed before in detail, conductivity increases as the polymer concentration increases and/or the content of acetic acid decreases. Whereas, viscosity rises with polymer concentration and/or content of acetic acid. Since the competition between conductivity and viscosity controls the variations in fiber diameter, fiber diameter increases with content of acetic acid, when the effect of viscosity is more dominant than that of conductivity. Otherwise, the increase in content of acetic acid promotes the formation of fibers with thinner diameters.

3.3.4 Influence of solution properties on standard deviation

3.3.4.1 Effect of gelatin concentration

The influence of gelatin concentration on standard deviation is illustrated in Figure 3.9(a)–(c). As depicted in these figures, the standard deviation is responsive to the changes in gelatin concentration but its effect depends on the level of other solution properties. For instance, at low alginate concentrations, low contents of alginate solution and high contents of acetic acid, increasing gelatin concentration brings about larger standard deviation. Otherwise, the effect of gelatin concentration on standard deviation becomes negligible. Therefore, it is obvious that gelatin concentration has interactions with other three solution properties, which agrees with the existence of terms X_1X_2, X_1X_3, and X_1X_4 in the model of standard deviation.

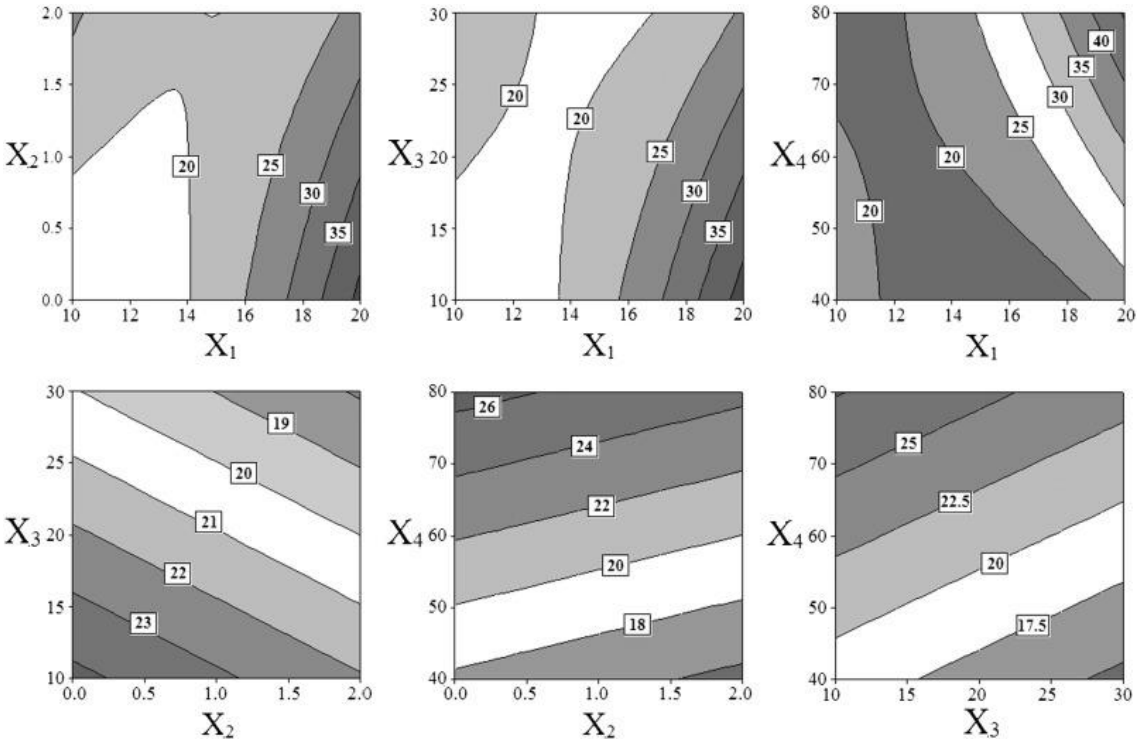

Figure 3.9 : Contour plots of solution properties on standard deviation in the absence of ethanol.

Meanwhile, the impact of gelatin concentration on standard deviation is also investigated after the addition of ethanol into the blend solution. As observed in Figure 3.10(a)-(c), higher gelatin concentration leads to smaller standard deviation at high

contents of alginate solution and low contents of acetic acid, while vice versa is valid at low contents of alginate solution and high contents of acetic acid, in addition to all levels of alginate concentration. This means that the interaction between gelatin concentration and alginate concentration disappears in the existence of ethanol, which proves the absence of term X_1X_2 in the model of standard deviation.

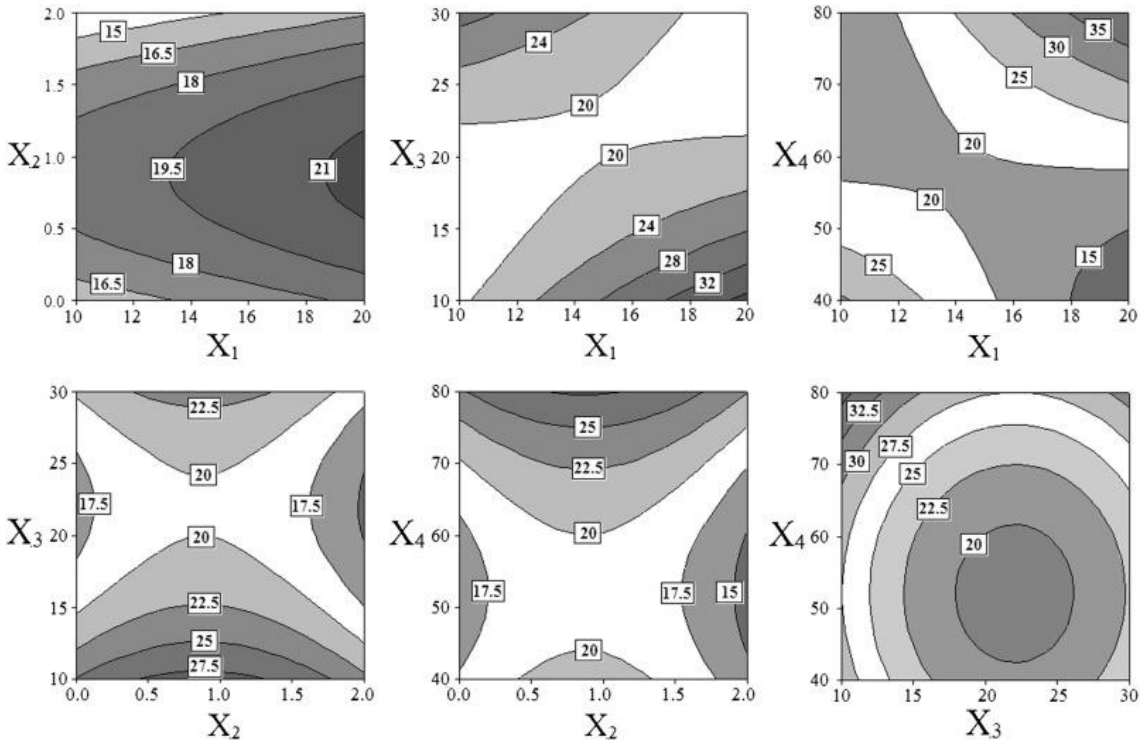

Figure 3.10 : Contour plots of solution properties on standard deviation in the presence of ethanol.

3.3.4.2 Effect of alginate concentration

The influence of alginate concentration on standard deviation is shown in Figure 3.9(a), (d), and (e). As demonstrated in these figures, the effect of alginate concentration is not always the same. When content of alginate solution and/or content of acetic acid are kept constant, increasing alginate concentration reduces the standard deviation slightly. On the other hand, the effect of alginate concentration on standard deviation is dramatically influenced by gelatin concentration. At high gelatin concentrations, higher alginate concentration results in smaller standard deviation, whereas at low gelatin concentrations, the effect of alginate concentration is totally reversed and standard deviation increases with the gelatin concentration. Hence, it is quite apparent that there

is an interaction between alginate concentration and gelatin concentration, which is in agreement with the presence of term X_1X_2 in the model of standard deviation.

In the meantime, the impact of alginate concentration on standard deviation is also studied after the addition of ethanol into the blend solution. As depicted in Figure 3.10(a), (d), and (e), keeping the other solution properties constant, an increase in the alginate concentration increases the standard deviation until a threshold limit. However, as the alginate concentration exceeds a limit, standard deviation decreases with the increase in alginate concentration. In the light of these results, it is clear that the interaction between alginate concentration and gelatin concentration becomes insignificant after the addition of ethanol into the blend solution.

3.3.4.3 Effect of content of alginate solution

The influence of content of alginate solution on standard deviation is given in Figure 3.9(b), (d), and (f). As observed in these figures, when the alginate concentration and/or content of acetic acid are kept constant, the standard deviation slightly reduces as the content of alginate solution increases. On the other hand, the effect of content of alginate solution on standard deviation is dramatically influenced by gelatin concentration. At high gelatin concentrations, higher content of alginate solution leads to smaller standard deviation, whereas at low gelatin concentrations, the effect of content of alginate solution is totally reversed and standard deviation increases with the gelatin concentration. Therefore, in agreement with existence of the term X_1X_3 in the model of standard deviation, content of alginate solution is found to have interaction with gelatin concentration.

Meanwhile, the impact of content of alginate solution on standard deviation is also investigated after the addition of ethanol into the blend solution. As demonstrated in Figure 3.10(b), (d), and (f), keeping alginate concentration and/or content of acetic acid constant, an increase in the content of alginate solution decreases the standard deviation until a threshold limit. However, as the content of alginate solution exceeds a limit, standard deviation increases with the content of alginate solution. On the other hand, the influence of content of alginate solution on standard deviation is significantly altered by gelatin concentration. At high gelatin concentrations, higher content of alginate solution

leads to smaller standard deviation, whereas at low gelatin concentrations, the effect of content of alginate solution is totally reversed and standard deviation increases with the gelatin concentration. Therefore, it can be concluded that the interaction between content of alginate solution and gelatin continues after the addition of ethanol into the blend solution.

3.3.4.4 Effect of content of acetic acid

The influence of content of acetic acid on standard deviation is presented in Figure 3.9(c), (e), and (f). As depicted in these figures, the effect of content of acetic acid is not always the same. When alginate concentration and/or content of alginate solution are kept constant, content of acetic acid increases with the standard deviation. On the other hand, the impact of content of acetic acid on standard deviation is highly depended on gelatin concentration. At low gelatin concentrations, higher content of acetic acid leads to smaller standard deviation, whereas at high gelatin concentrations, the effect of content of acetic acid is totally reversed and standard deviation increases with the gelatin concentration. This means that the effect of content of acetic acid on standard deviation is only altered by gelatin concentration, implying the interaction of content of acetic acid with gelatin concentration, which agrees with the presence of the term X_1X_4 in the model of standard deviation.

In the meantime, the impact of content of acetic acid on standard deviation is also studied after the addition of ethanol into the blend solution. As observed in Figure 3.10(c), (e), and (f), keeping alginate concentration and/or content of alginate solution constant, an increase in the content of acetic acid decreases the standard deviation until a threshold limit. However, as the content of acetic acid exceeds a limit, standard deviation increases with the content of acetic acid. On the other hand, the effect of content of acetic acid on standard deviation is dramatically influenced by gelatin concentration. At low gelatin concentrations, higher content of alginate solution leads to smaller standard deviation, whereas at high gelatin concentrations, the effect of content of alginate solution is totally reversed and standard deviation increases with the gelatin concentration. This observation proves the interaction between content of acetic acid and gelatin concentration standing still after the addition of ethanol into the blend solution.

3.3.5 Processing window for gelatin/sodium alginate nanofibers

The key issue in the field of tissue engineering is to develop a temporary template (scaffold) that can substitute the natural ECM until the seeded cells can produce a new functional matrix. For this purpose, electrospun nanofibrous scaffolds have been extensively studied because of their ECM-like topographies. Within this respective, the main goal of the present study was to provide an overview on the fabrication of gelatin/sodium alginate nanofibers with targeted diameter by understanding how the variations in solution properties affect the fiber diameter and its standard deviation. In this context, response surface methodology based on a three-level, four-variable Box–Benkhen design was employed, results of which implied that the highest gelatin concentration (20% w/v) coupled with the lowest content of alginate solution in the blend solution (10 vol%), and the highest content of acetic acid in the solvent of gelatin solution (80 vol%) resulted in the production of nanofibers with the largest diameter both in the absence and presence of ethanol. However, the influence of alginate concentration on fiber diameter was different for both cases. In the absence of ethanol, nanofibers with thicker diameter were obtained at low alginate concentrations. Whereas, this trend turned toward the opposite direction after the addition of ethanol into the blend solution. As depicted in Figure 3.11(a) and (b), electrospinning of blend solutions under these conditions gave rise to the bead-free and randomly arrayed nonwoven nanofibers with the average diameters of 218 ± 47 and 206 ± 63 nm in the absence and presence of ethanol, respectively. However, nanofibers were fused together at junctions in the presence of ethanol.

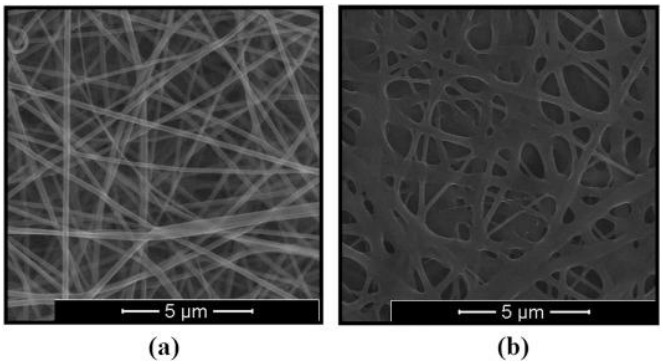

Figure 3.11 : Representative SEM images of nanofibers with the largest diameter in the (a) absence and (b) presence of ethanol.

3.4 Conclusions

The present study focused on presenting a facile and effective tool to produce electrospun gelatin/sodium alginate nanofibers with controllable diameter, as well as understanding how the variations in solution properties (namely, gelatin concentration, alginate concentration, content of alginate solution in the blend solution, and content of acetic acid in the solvent of gelatin solution) affect the fiber diameter and its standard deviation. In this context, blend solutions that were prepared both in the absence and presence of ethanol were electrospun into nanofibers to develop empirical models with the aid of response surface methodology based on a three-level, four-variable Box–Behnken design technique. Consequently, it was determined that highest gelatin concentration (20% w/v) coupled with the lowest content of alginate solution in the blend solution (10 vol%) and the highest content of acetic acid in the solvent of gelatin solution (80 vol%) brought about nanofibers with the largest diameter both in the absence and presence of ethanol. However, the impact of alginate concentration displayed reverse trends for both cases. Lower alginate concentration led to nanofibers with thicker diameter in the absence of ethanol, whereas the increase in higher alginate concentration resulted from the higher alginate concentration. It should also be noted that the models are applicable only under the experimental conditions inside the design space and need to be redeveloped for any other polymer solutions or electrospinning conditions. The potential use of the as-prepared gelatin/sodium alginate nanofibers in the applications of bone tissue engineering are still under investigation of our research group.

4. FABRICATION OF BIOACTIVE GLASS CONTAINING NANOCOMPOSITE FIBER MATS FOR BONE TISSUE ENGINEERING APPLICATIONS(*)

4.1 Introduction

The treatment of bone defects resulting from trauma, malignancy, infections, tumors or congenital diseases is a major challenge. Therefore, bone tissue engineering has emerged with the intension to repair, replace or regenerate these bone defects with the aid of biodegradable scaffolds, which serve as a temporary framework for providing a suitable environment that allows cells to synthesize their own extracellular matrix (ECM) and to degrade upon neogenesis of ECM [4,7,11,120–123]. Among existing methods for the fabrication of scaffolds, electrospinning has received much attention as a simple, cost-effective, and versatile technique to prepare non-woven mats consisting of fibers with diameters ranging from microns down to a few nanometers [7,11,48,124]. Using electrospinning, it is possible to create scaffolds that mimic the native architecture of the bone ECM owing to its high porosity, high aspect ratio, and large surface area. The large specific surface area of the electrospun scaffolds makes more surfaces suitable for cellular attachment, while the high porosity and the high interconnectivity of pores provide enough space for vascularization required to nourish new bone and to enable the exchange of nutrient and metabolic waste between the scaffold and environment [124].

To date, a variety of natural and synthetic polymers have been investigated for the fabrication of nanofibrous scaffolds. However, natural and synthetic polymers alone cannot meet all the requirements of an ideal scaffold. To overcome the shortcomings of synthetic and natural polymers, blends of two or more types of polymers have been devised by researchers that combines the advantages of both synthetic and natural materials, potentially improving cell affinity while offering ideal mechanical properties

(*) This chapter is based on the paper: "**Gönen, S. Ö.**, Erol Taygun, M., and Küçükbayrak, S. (2016). Fabrication of bioactive glass containing nanocomposite fiber mats for bone tissue engineering applications. *Composite Structures*, *138*, 96–106."

for tissue engineering applications. Within this respect, electrospun Gt/PCL nanofibers had been widely studied for engineering diversified tissues, including nerve [35,125–126], muscle [75], dental [127], cardiac [76], cardiovascular [128], bone [34,129], and cartilage [130–131]. It was reported that blending PCL with gelatin resulted in a new biomaterial with improved mechanical, physical, chemical, and biological properties [35,48,72,108].

Recent research efforts have been focused upon the development of composite materials comprising the biodegradable polymer matrix combined with inorganic components, such as hydroxyapatite [127,132], tricalcium phosphate [133], and bioactive glasses [7,11,14,134–139]. The reason lying behind that was to mimic both the physical architecture and chemical composition of natural bone ECM since it has a highly complex and well-harmonized composite structure that consists of type I collagen fibrils (50–500 nm in diameter) mineralized with a thin, highly crystalline carbonated hydroxyapatite layer [7,31,139].

Among inorganic components, bioactive glasses are a group of inorganic bioactive materials that have been extensively used in the treatment of bone defects, due to their ability to stimulate bone regeneration via dissolution, followed by the formation of a surface layer of hydroxycarbonate apatite upon exposure to physiological fluids [140–141]. This surface layer resembles the chemical composition and structure of bone mineral and thus, plays a key role in forming a bond with the surrounding bone tissues. Since their development, a large variety of bioactive glasses based upon derivations of the 45S5 composition have been developed and applied in bone tissue engineering owing to their good bioactivity, osteoconductivity, osseointegration, and biodegradability [10,16,124,142–146]. However, the main drawback of bioactive glasses is their internal stiffness, brittleness and low mechanical properties that make them difficult to use in load-bearing applications [12,147]. Within this respect, in an effort to make use of the intrinsic properties of polymers and bioactive glasses, other researchers attempted to incorporate bioactive glass particles into biodegradable polymers as fillers to form composite nanofibers. It was determined that the addition of the bioactive glass into the polymeric matrix greatly enhanced the mechanical and biological properties [7,11,14,136–139]. Hence, this study concentrated on loading bioactive glass particles

into the Gt/PCL nanofibers by using the electrospinning method to develop a composite scaffold with improved bioactivity, biodegradability, osteoconductivity, and mechanical stability for bone tissue engineering.

In addition, the structural integrity of a scaffold is an important aspect for the determination of the proliferation, differentiation, and long term-survival of the anchorage depended cells in the scaffolds [34]. Since gelatin is water soluble, the electrospun fibers can partially dissolve and lose its fibrous form upon exposure to a high humidity ambient (i.e., 80–90%) for a certain period of time [45,148]. In the literature, several physical (i.e., dehydrothermal treatment, UV irradiation, and plasma treatment) and chemical methods (e.g. chemically modifying gelatin with the use of cross-linking agents, including glutaraldehyde, 1-ethyl-3-(3-dimethylamino propyl) carbodiimide hydrochloride, and genipin) have been reported for cross-linking of the gelatin [45,55,116,148–152]. Among them, the use of glutaraldehyde is by far the most widely used cross-linking treatment, due to its high efficiency, ease of availability, and inexpensiveness [45]. Therefore, a cross-linking treatment with glutaraldehyde was also performed to preserve the fibrous morphology of the as-prepared mats.

On the other hand, a variety of studies have recently focused on enhancing the biological performance of bioactive glasses by doping them with therapeutic metal ions, including strontium [4,121,140] and copper [31,120]. Upon the dissolution of these bioactive glasses, the controlled release of therapeutic metal ions brings about additional functionalities, such as osteogenesis, angiogenesis, and antibacterial effects. Taken together, we hypothesized that combining polymers with bioactive glasses doped with strontium or copper will enable to develop nanocomposite fiber mats that have a potential to be used as multifunctional scaffolds in bone tissue engineering applications. In this context, emphasis has been placed on investigating the in vitro degradation behavior and bioactivity of the as-prepared nanocomposite fiber mats. To the best of our knowledge, this study is the first report that employs strontium or copper substituted bioactive glass particles to develop a nanocomposite material as a multifunctional scaffold by using electrospinning technique. In this context, strontium and copper containing bioactive glasses and gelatin/PCL blends were used to fabricate

nanocomposite scaffolds. The structural, bioactive and thermal behaviors of the scaffolds were investigated.

4.2 Materials and Methods

4.2.1 Materials

Gelatin (Gt, type A, from porcine skin), poly(ε-caprolactone) (PCL, Mn = 70,000–90,000), silicon dioxide (SiO_2, Sigma Aldrich), and copper(II) nitrate trihydrate ($Cu(NO_3)_2 \cdot 3H_2O$) were obtained from Sigma–Aldrich Chemicals. Glacial acetic acid (AcOH), formic acid, glutaraldehyde (GTA), di-sodium hydrogen phosphate anhydrous (Na_2HPO_4), calcium carbonate ($CaCO_3$), and sodium carbonate (Na_2CO_3) were purchased from Merck. Strontium nitrate ($Sr(NO_3)_2$) was supplied from Riedel-de-Haen. All chemicals were used as provided without further purification.

4.2.2 Preparation of bioactive glass particles

Two modified versions of 45S5 were prepared using a classical melting method in the present study. For this purpose, ca. 8.2 wt% of CaO in Bioglass® composition was replaced with SrO or CuO in order to produce strontium or copper substituted bioactive glass particles (Sr-BG or Cu-BG) with the composition of SiO_2:CaO:P_2O_5:Na_2O:XO (45:22.5:6:24.5:2 wt%, X = Sr or Cu). To prepare bioactive glass (BG) particles, appropriate amounts of precursor chemicals were first placed in a platinum crucible. After that, they were melted at 1350 °C for 2 h and rapidly quenched into deionized water to form frits. As-prepared frits were then ground and placed in the platinum crucible for repeating the melting and the quenching steps in order to obtain a homogeneous structure. Finally, the obtained BG frits were ground ($\leqslant$45 μm) to yield the BG particles.

4.2.3 Preparation of electrospinning solutions

BG particles were first dispersed in a co-solvent of acetic acid and formic acid (1:1 in volume) at room temperature for 1 h. Then, polymers were separately added into the BG containing solvents and stirred at room temperature for 3 h in order to obtain homogenous solutions with BG contents varying from 0% to 7.5% (w/v). Afterwards,

20% (w/v) Gt solution and 15% (w/v) PCL solution were mixed in a Gt/PCL ratio of 7/3 (w/w) at room temperature for 2 h.

4.2.4 Electrospinning

The as-prepared solutions were transferred to a plastic syringe equipped with a flat stainless steel needle, which was connected to a high-voltage supply. Voltage applied to the needle tip was 22.5 kV. The flow rate was set as 3 ml/h by a syringe pump. Nonwoven electrospun fibers were deposited onto an aluminum foil wrapped around a grounded collector placed at a distance of 10 cm perpendicular to the needle tip. Electrospinning procedure was performed under ambient conditions. The resultant nanocomposite fiber mats were dried at 37 °C for a couple of days to remove residual solvent and then transferred to a desiccator prior to further investigations.

4.2.5 Cross-linking treatment

Cross-linking process was carried out by placing samples of the as-prepared nanocomposite fiber mats in a sealed desiccator containing 25% (v/v) glutaraldehyde solution in a Petri dish. After 4 days, samples were removed from the desiccator and kept in the fume hood for 2 h, followed by a post treatment at 110 °C for 1 h to remove residual glutaraldehyde and to partially enhance the cross-linking. The success of cross-linking was determined by testing the dissolubility of the cross-linked mats immersed in simulated body fluid (SBF, pH 7.4) at 37 °C for different time points (up to 28 days).

4.2.6 Assessment of in vitro bioactivity

The acellular bioactivity of the nanocomposite fiber mats was performed in vitro to assess the potential osteoconductive properties of the materials. Briefly, small pieces of the cross-linked mats were soaked into the freshly prepared SBF in sterile polyethylene containers and were stored at controlled temperature of 37 °C for various time points up to 28 days. The degradation behavior of the samples was studied as a function of immersion time in SBF. At the end of each time point, the samples were removed from SBF, gently rinsed with deionized water for three times to remove saline, and dried at 37 °C until constant mass was reached. After that, the samples were kept in desiccators for further characterization. Meanwhile, SBF was cooled to room temperature, and the

concentration of therapeutic ions released into SBF was measured, as well. All experiments were conducted in duplicate.

4.2.7 Characterization of bioactive glass particles and nanocomposite fiber mats

The thermal behavior of BG particles and nanocomposite fiber mats were investigated by using a TA instruments Q600 SDT model thermogravimetric analyzer and differential scanning calorimeter. 4 mg of samples were heated at a rate of 20 °C/min from room temperature to 1000 °C under a nitrogen atmosphere.

The amorphous structure of BG particles and the characteristic phases of the nanocomposite fiber mats before and after immersion in SBF were identified using an X-ray diffraction analyzer (XRD, Bruker™ D8 Advance) with Cu-Kα radiation. XRD patterns were acquired over a 2θ range from 10° to 90° with a step size of 0.01°.

The surface morphology and microstructure of the nanocomposite fiber mats before and after immersion in SBF were observed by using a scanning electron microscope (SEM) operated at 20 kV. Prior to the SEM measurements, all of the samples cut from the fibrous mats were coated with platinum under vacuum for 120 s by using a SC7620 sputter coater (Quorum Technologies Ltd) in order to reduce electron charging effects. The diameter of the electrospun fibers was measured by using Image J software (National Institute of Health, USA). For each experiment, average fiber diameter and its standard deviation were determined from 25 measurements of the randomly chosen fibers.

The functional groups of the nanocomposite fiber mats before and after immersion in SBF were investigated by Fourier-transform infrared (FT-IR) spectroscopy. FT-IR spectra were collected using a Perkin Elmer Spectrum 100 model spectrometer in transmittance mode in the mid-IR region (4000–650 cm^{-1}).

The release of therapeutic ions was measured as a function of immersion time in SBF with the aid of inductively coupled plasma – mass spectrometer (ICP-MS, Perkin Elmer Elan DRC-e).

The percentage of weight loss was calculated from the weight of the nanocomposite fiber mats before and after immersion in SBF by using Eq. (4.1):

$$\%W_L = \frac{W_{0,dry} - W_{t,dry}}{W_{0,dry}} \times 100 \quad (4.1)$$

where $W_{0,dry}$ is the weight of the nanocomposite fiber mats before being soaked in SBF, while $W_{t,dry}$ is the weight of the nanocomposite fiber mats after being soaked in SBF and subsequently dried at 37 °C overnight.

4.3 Results and Discussion

4.3.1 Characterization of BG particles

XRD analysis of the BG particles was performed to validate the amorphous nature of BG particles. As seen from Figure 4.1(a), both of the BG particles exhibited a broad band characteristic, proving the amorphous state of these BG particles.

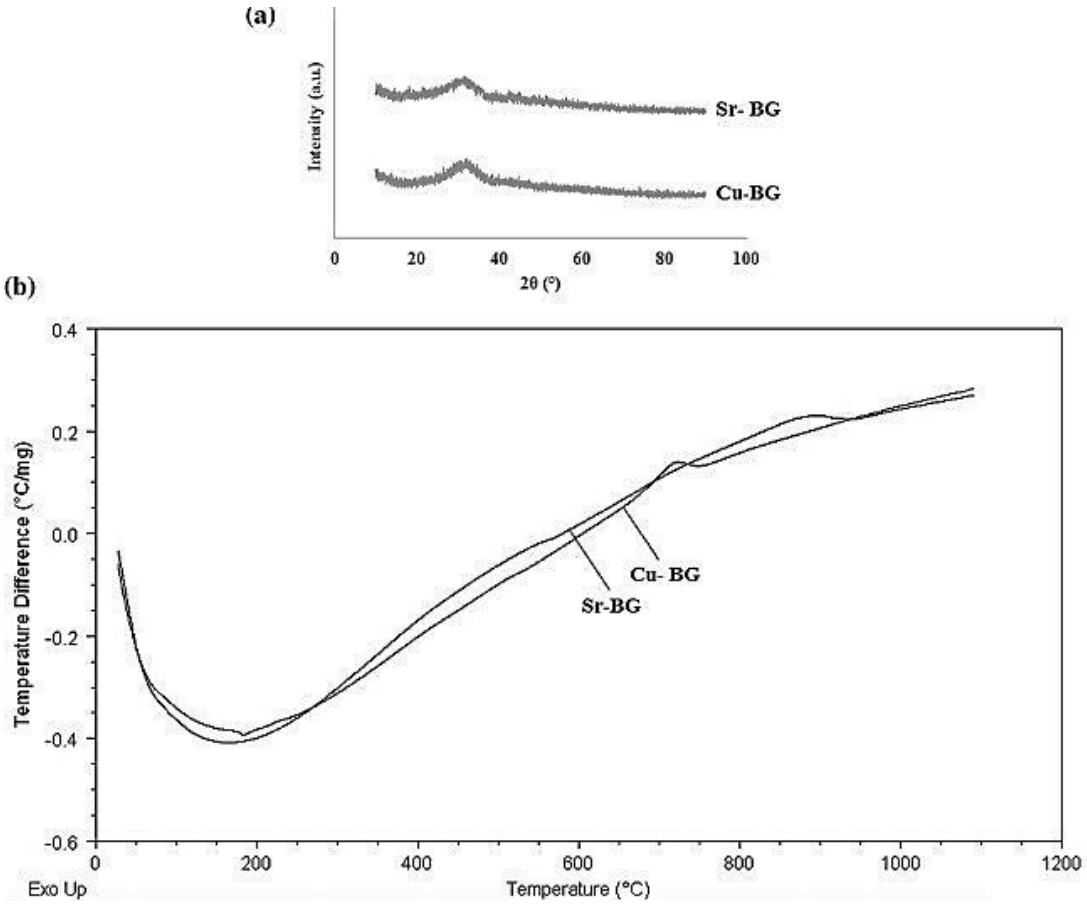

Figure 4.1 : Characterization results of the BG particles: (a) XRD patterns, and (b) DTA diagram.

In addition, thermal behaviors of the BG particles were also assessed to determine their characteristic temperatures, including glass transition and crystallization temperatures. Figure 4.1(b) shows the DTA thermograms of the glass samples scanned at the heating rate of 20 °C/min. As seen from Fig. 1b, it was determined that the glass transition temperatures of Sr-BG and Cu-BG were 562 °C and 528 °C, respectively, whereas crystallization temperatures were 889 °C and 723 °C. In the light of these data, it was clear that both temperatures were higher for Sr-BG compared to Cu-BG. It can be also said that glass samples are suitable for the glass–ceramic production.

4.3.2 Surface morphology of nanocomposite fiber mats

SEM micrographs, given in Figure 4.2(a), revealed that the electrospun Gt/PCL nanofiber mats were composed of randomly oriented, uniform, and bead free nanofibers, with an average fiber diameter of 346 ± 67 nm. The fabrication of many different sized Gt/PCL nanofibers have been reported by other researchers in the open literature. Some of them were in the size of 189 ± 56 nm [72], 471 ± 218 nm [35], 283 ± 87 nm [153], 161 nm [127], 663 ± 107 nm [39], 239 ± 37 nm [76], 540 ± 140 nm [154], and 440 ± 63 nm [155] when electrospinning was conducted with different solution and processing parameters.

On the other hand, nanocomposite fiber mats were also successfully generated without any beads through the electrospinning process (Figure 4.2(b) and (c)). As the BG content increased from 2.5 wt% to 7.5 wt%, the diameter of Gt/PCL/Sr-BG nanocomposite fiber mats ranged from 448 ± 111 nm to 532 ± 190 nm, whereas the diameter of Gt/PCL/Cu-BG nanocomposite fiber mats varied from 400 ± 71 nm to 463 ± 107 nm (Table 4.1). These results indicated that the introduction of BG particles into the Gt/PCL nanofibers increased the fiber diameter. Similar results were also obtained by other researchers when hydroxyapatite nanoparticles were introduced into the Gt/PCL nanofibers. For instance, Yang et al. [127] indicated an increase in the average diameter from 161 nm to 281 nm after the inclusion of hydroxyapatite nanoparticles into the system, while Linh et al. [132] reported that fiber diameter varied from 0.12 μm to 3.0 μm depending on the increase in the content of hydroxyapatite nanoparticles. It was claimed that this was likely due to the increase in viscosity with the content of hydroxyapatite

nanoparticles [132]. Similarly, Kouhi et al. [134] showed that average diameter of nanofibers increased from 411 nm to 483 nm by increasing BG content from 0 to 20 wt% of the PCL content.

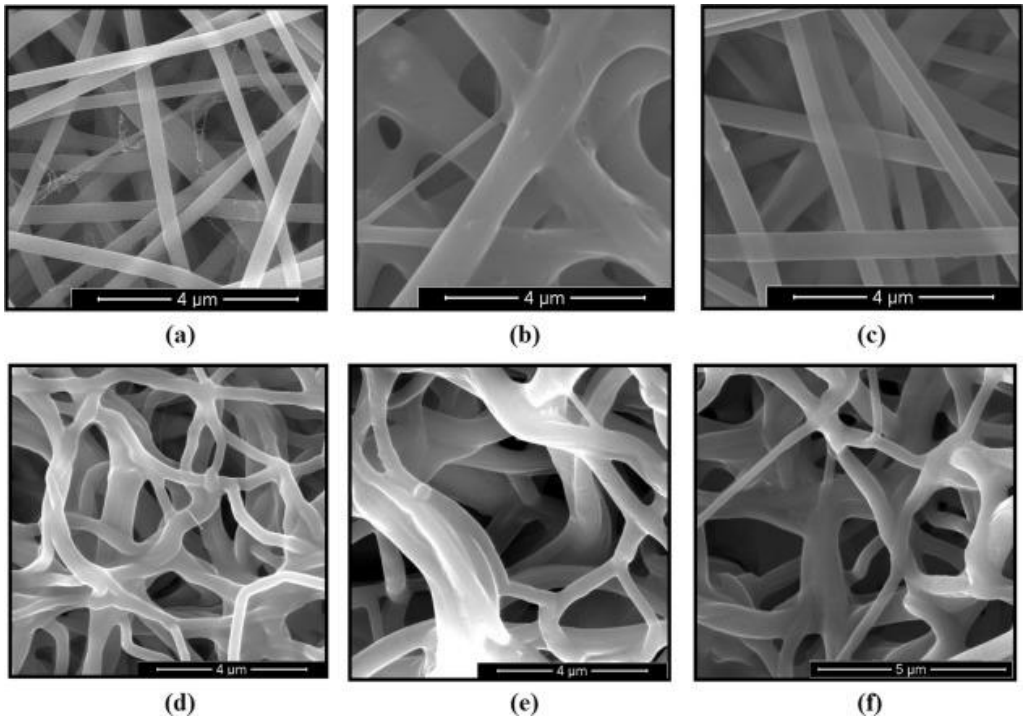

Figure 4.2 : SEM images of (a–c) as-spun and (d–f) cross-linked fiber mats: (a, d) Gt/PCL, (b, e) Gt/PCL/7.5Sr-BG, and (c, f) Gt/PCL/7.5Cu-BG fiber mats.

Table 4.1 : Average diameter of the fiber mats.

BG content (% w/v)	BG type	Coded name	Average fiber diameter (nm)
0	–	Gt/PCL	346 ± 67
2.5	Sr-BG	Gt/PCL/2.5Sr-BG	448 ± 111
5.0	Sr-BG	Gt/PCL/5Sr-BG	499 ± 86
7.5	Sr-BG	Gt/PCL/7.5Sr-BG	532 ± 190
2.5	Cu-BG	Gt/PCL/2.5Cu-BG	400 ± 71
5.0	Cu-BG	Gt/PCL/5Cu-BG	463 ± 68
7.5	Cu-BG	Gt/PCL/7.5Cu-BG	463 ± 107

Additionally, the formation of ultra large-sized fibers were observed when the BG content was 10 wt% (data not shown), defining the upper boundaries of the system. This was consistent with the findings of Noh et al. [136]. They determined that a well-developed nanocomposite fiber of poly(lactic acid) filled with BG nanoparticles was obtained when BG nanofiller was incorporated up to 10%, while beads and ultra large-sized fibers were obtained above that value.

4.3.3 Structural analysis of nanocomposite fiber mats

FT-IR spectroscopy was employed to investigate the functional groups of the fibrous mats. Figure 4.3 shows the transmittance spectra of nanofiber mats. Common bands of PCL are asymmetric CH_2 stretching at 2945 cm^{-1}, symmetric CH_2 stretching at 2865 cm^{-1}, carbonyl stretching at 1727 cm^{-1}, C–O and C–C stretching at 1293 cm^{-1}, asymmetric COC stretching at 1240 cm^{-1}, and symmetric COC stretching at 1170 cm^{-1} [39,72,152]. Whereas, FT-IR spectra of gelatin consist of typical bands such as N–H stretching at 3280 cm^{-1} (amide A), amide B at 3065 cm^{-1}, C = O stretching at 1650 cm^{-1} (amide I) and N–H bending coupled with C–N stretching at 1540 cm^{-1} (amide II), CH_2 scissoring and asymmetric CH_3 bending at 1450 cm^{-1}, CH_2 wagging at 1406 cm^{-1}, C–N stretching vibration coupled with N–H stretching in phase bending at 1240 cm^{-1} (amide III), and C–C stretching at 1158 cm^{-1} [39,72,116,150–152,156]. As depicted in Figure 4.3, the appearance of these characteristic peaks confirmed the presence of both polymers in the structure of Gt/PCL nanofiber mats. Meanwhile, Gt/PCL/Sr-BG and Gt/PCL/Cu-BG nanocomposite fiber mats showed nearly identical spectra, with additional bands corresponding to Si–O–Si symmetric and asymmetric stretching vibration located near 800 and 1070 cm^{-1}, respectively [10]. Therefore, FT-IR results confirmed that the BG particles were successfully incorporated into the Gt/PCL fibrous mats.

In addition to the FT-IR spectra, XRD patterns of the fibrous mats were also determined, as given in Figure 4.4. In general, gelatin shows no peak in XRD pattern, which indicates its amorphous nature. On the other hand, PCL shows sharp peak at 2θ of 22° and a relatively low intensity peak at 24°, suggesting the crystalline nature of PCL. Therefore, the presence of the characteristic peaks of PCL confirmed the crystalline nature of all fiber mats. However, the intensity of PCL peaks was lower for nanocomposite fiber mats. Similarly, Lin et al. [11] reported that the degree of crystallinity of the PCL decreased with the addition of mesoporous BG nanoparticles. It was inferred that during crystallization, the mesoporous BG nanoparticles were probably aggregated and subsequently occluded in intercrystalline domains, thereby hindering the crystallization of the polymer [11]. Meanwhile, other than the peaks of PCL, no

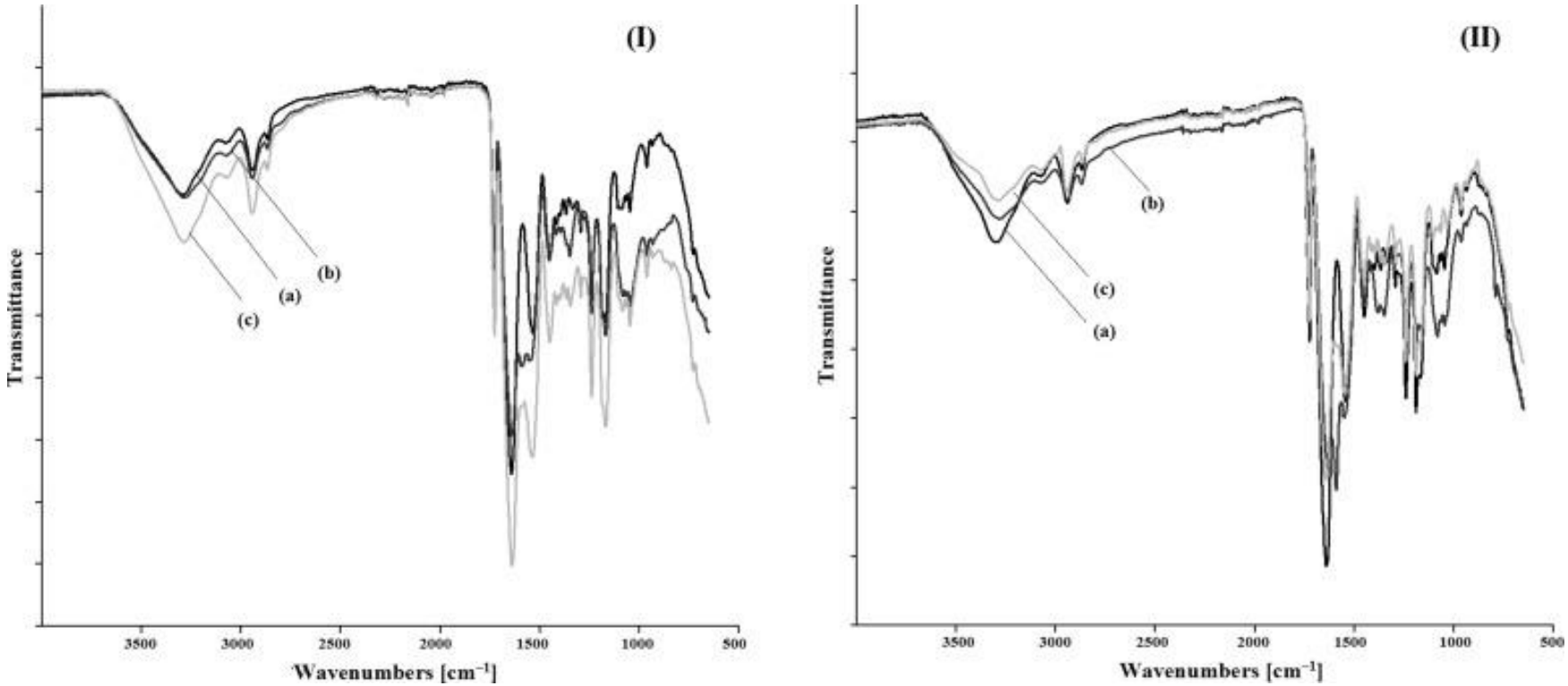

Figure 4.3 : FT-IR spectra of (I) as-spun and (II) cross-linked fiber mats: (a) Gt/PCL, (b) Gt/PCL/7.5Sr-BG, and (c) Gt/PCL/7.5Cu-BG fiber mats.

additional peak was observed for nanocomposite fiber mats suggesting that the amorphous nature of BG particles continued after the electrospinning process.

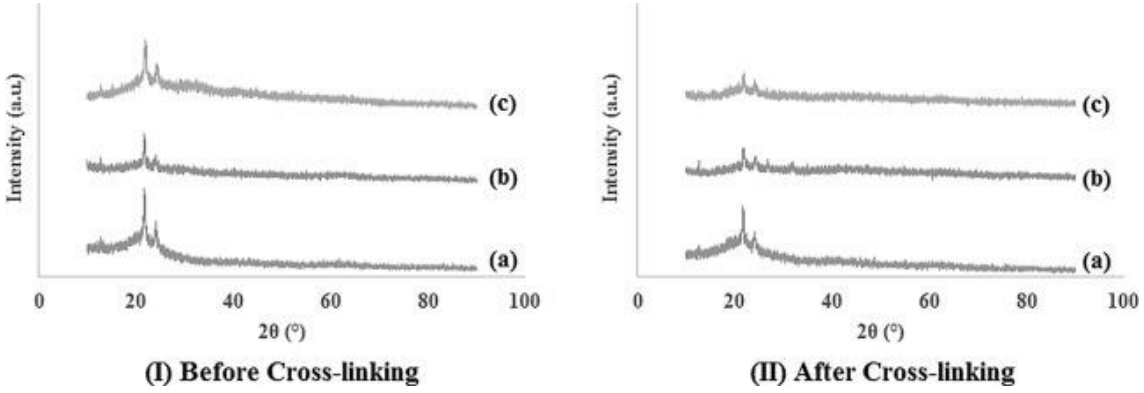

Figure 4.4 : XRD patterns of (I) as-spun and (II) cross-linked fiber mats: (a) Gt/PCL, (b) Gt/PCL/7.5Sr-BG, and (c) Gt/PCL/7.5Cu-BG fiber mats.

4.3.4 Confirmation of cross-linking treatment

Since gelatin is water soluble, even a drop of water can immediately destroy the nanofibrous structure. Moreover, electrospun fibers are even able to gradually form point bonds at the fiber junctions if placed in a high humidity ambient (i.e., 80–90%) for a certain period of time. To overcome this issue, a cross-linking treatment with glutaraldehyde vapor was applied. After the cross-linking treatment, the color of fibrous mats changed from white to yellow, which was explained by other researchers to be due to the formation of aldimine linkages (–CH = N–) between the free amino groups of lysine or hydroxylysine amino acid residues of gelatin and the aldehyde groups of glutaraldehyde [45,86,148–149,151]. In addition, the fibrous form of the as-prepared mats has been preserved during cross-linking treatment (Figure 4.2(d–f)). However, the fibers at touching points were fused together because of the existence of the water in moisture-rich glutaraldehyde vapor. In the light of these data, it is obvious that the fiber morphology was affected to some extent from the cross-linking treatment. Similar observations have also been indicated in other studies [45,86,148,150].

On the other hand, a change in the chemical signatures of gelatin during the cross-linking of the nanofibrous scaffolds was evaluated by FT-IR spectroscopy. As depicted in Figure 4.3, the effectiveness of the cross-linking process can be confirmed based on the presence of pronounced peaks in the C–H stretching region. The three methylene

groups of the glutaraldehyde molecule contribute to the intensity of bands at 2945 and 2865 cm^{-1}. In addition, the ratio of intensities of bands at 3065 cm^{-1} (which can be attributed to amide B) and 3280 cm^{-1} (related to N–H stretching mode of amide A) gradually decreased. This is consistent with the results of Skotak et al. [157].

Meanwhile, XRD analysis was also conducted to assess the changes in the crystallinity of the fibrous mats during the cross-linking treatment. As observed in Figure 4.4, XRD pattern showed that the characteristic diffraction peaks of PCL were significantly weakened after cross-linking treatment, proving a decreased crystallinity of PCL. The lower crystallinity of fiber mats suggested the presence of molecular interactions, as well.

To confirm the success of the cross-linking treatment, the nanofibrous mats were investigated through SEM and FT-IR analysis after being soaked in SBF. After immersing for 28 days, all of the fiber mats still kept an intact appearance in macroscopic view. From Figure 4.5, it was obvious that the nanocomposite fiber mats preserved their fibrous morphology, while the fibrous network of Gt/PCL mat experienced significant swelling after 24 h immersing in SBF. In the light of these data, it can be concluded that the addition of BG particles into the Gt/PCL nanofibers improved the water-resistancy of the fiber mats. In addition, the presence of the characteristic bands of gelatin in the FT-IR spectra (Figure 4.6) after the cross-linking treatment also validated the success of the cross-linking treatment.

4.3.5 Thermogravimetric analysis of nanocomposite fiber mats

Thermogravimetric analysis was performed to determine the thermal degradation pattern of the fiber mats. Figure 4.7 shows the DTA and TGA curves of the fiber mats and the results taken from these curves are given in Table 4.2. As seen from Table 4.2, gelatin exhibited a degradation peak at 324 °C, while PCL showed a degradation peak at 404 °C. However, nanocomposite fiber mats revealed only one peak at 350 °C and 358 °C for Gt/PCL/Sr-BG and Gt/PCL/Cu-BG fiber mats, respectively. These results confirmed that composite structures were successfully prepared in the current study.

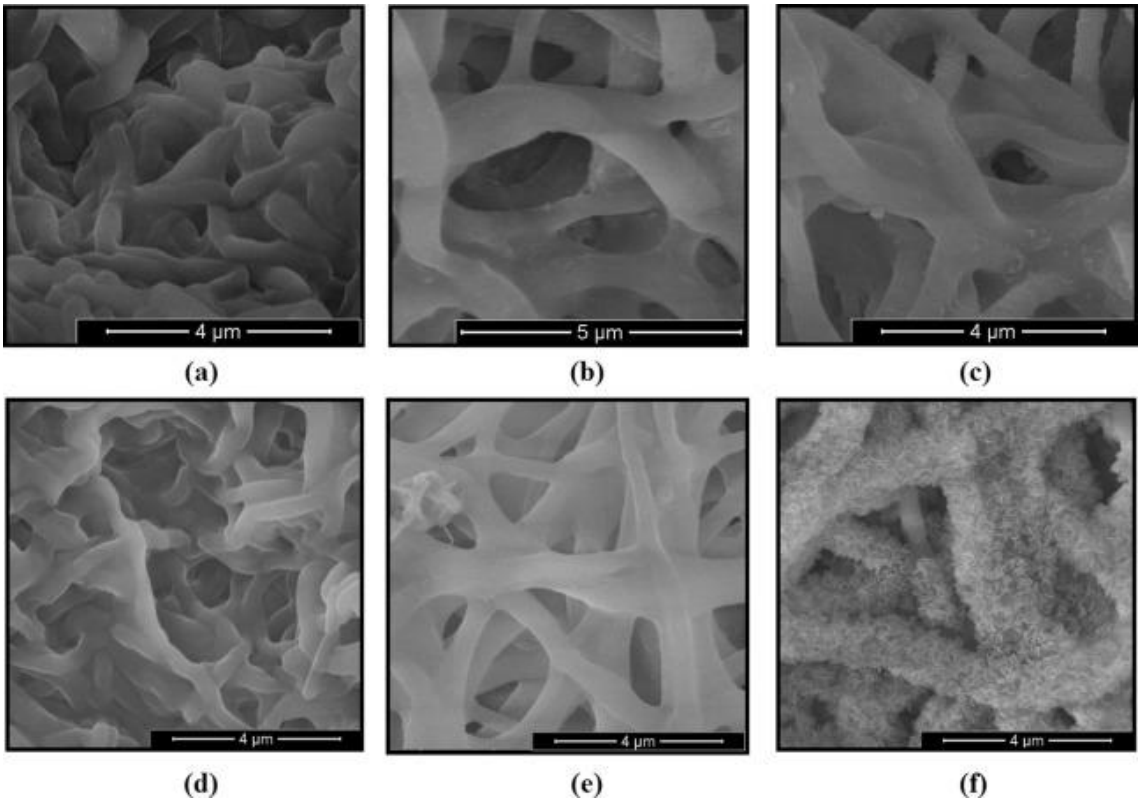

Figure 4.5 : SEM images of fiber mats after being soaked in SBF for (a–c) 1 day and (d–f) 28 days: (a, d) Gt/PCL, (b, e) Gt/PCL/7.5Sr-BG, and (c, f) Gt/PCL/7.5Cu-BG fiber mats.

Meanwhile, the thermogram for Gt/PCL fiber mat showed a steep weight loss between 220 and 500 °C and no residual matter remained after 500 °C indicating complete degradation of the polymer. In the case of nanocomposite fiber mats, 73% weight loss was observed over the temperature range used. This weight loss may be due to the removal of organic moieties, namely gelatin and PCL. At 1000 °C, a residual weight of 27% in the nanocomposite fiber mats indicated the presence of BG, which is consistent with the amount of BG content with respect to the polymeric content. Thus, the thermogravimetric analysis confirmed the removal of organic moieties and the presence of BG in the nanocomposite fiber mats.

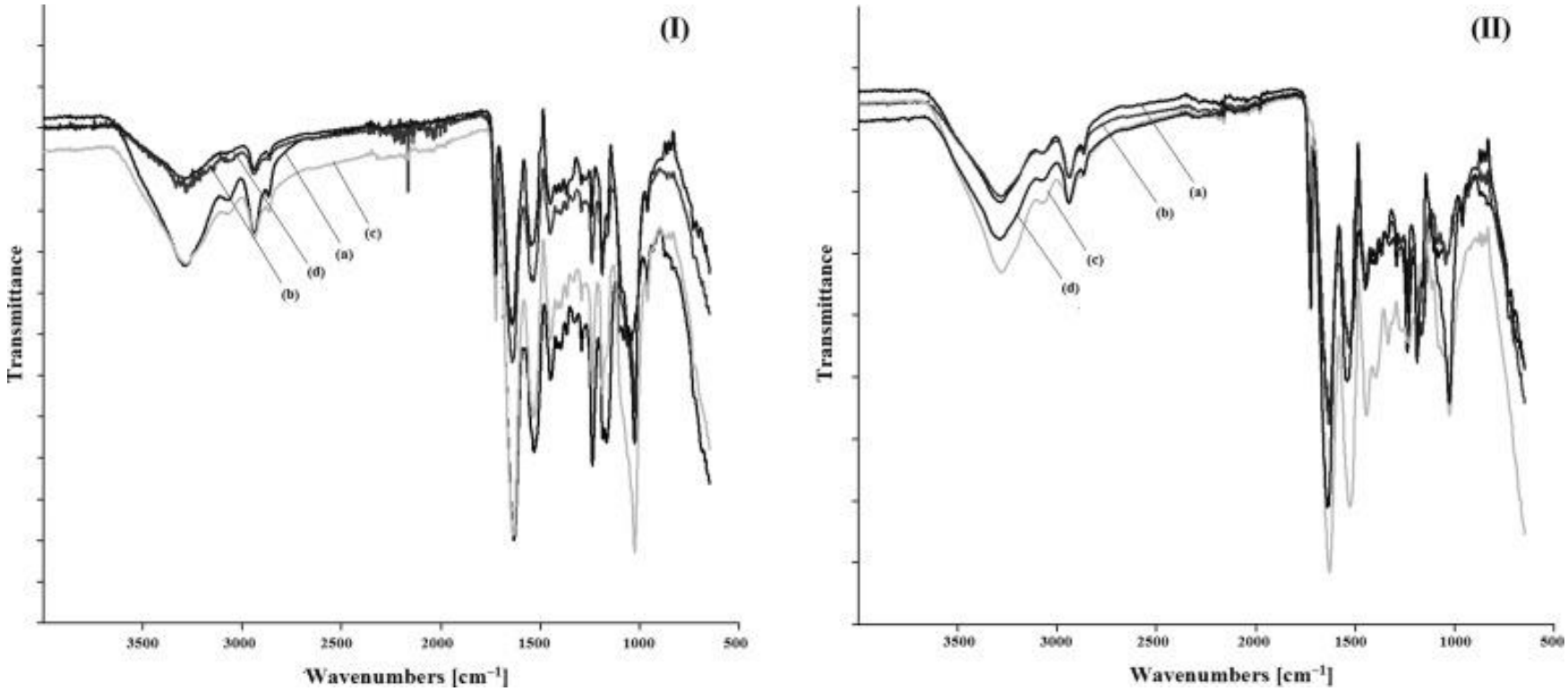

Figure 4.6 : FT-IR spectra of (I) Gt/PCL/Sr-BG and (II) Gt/PCL/Cu-BG fiber mats, with different BG contents, after immersed in SBF for 28 days: (a) 0 wt%, (b) 2.5 wt%, (c) 5 wt%, and (d) 7.5 wt%.

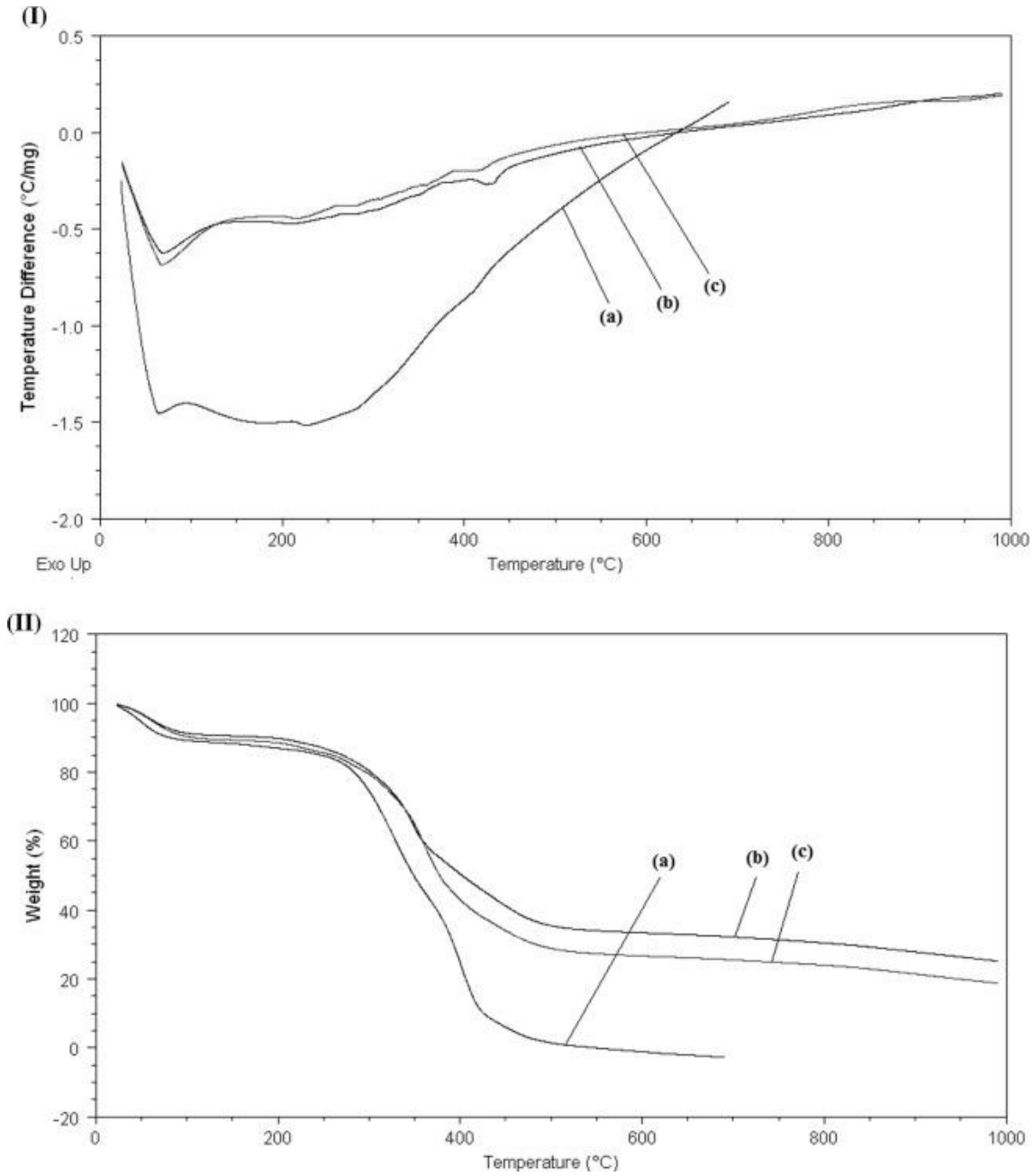

Figure 4.7 : Thermal behavior of (a) Gt/PCL, (b) Gt/PCL/7.5Sr-BG, and (c) Gt/PCL/7.5Cu-BG fiber mats: (I) DTA diagram, and (II) TGA diagram.

4.3.6 Assessment of in vitro bioactivity

The bone-bonding potentiality of a biomaterial is often estimated by examining its ability to form a layer of hydroxycarbonate apatite on its surface when exposed to SBF. In order to confirm the formation of this layer, the nanocomposite fiber mats were analyzed with SEM, XRD, and FT-IR before and after being soaked in SBF.

Table 4.2 : Thermal behavior of the fiber mats.

Coded name	Main region of decomposition (°C)	Decomposition weight (%)	$T_{max,1}$ (°C)	$T_{max,2}$ (°C)	Maximum degradation rate (%/min)
Gt/PCL	219–499	84.86	324	404	15.57
Gt/PCL/7.5Sr-BG	148–552	56.55	350	–	10.63
Gt/PCL/7.5Cu-BG	147–552	62.01	358	–	13.03
Gt/PCL	219–499	84.86	324	404	15.57

Visual inspection of the Gt/PCL fiber mat showed no sign of mineral formation after 4-week study (Figure 4.5(d)), suggesting that the formation of hydroxyapatite did not occur within 28 days when being immersed in SBF. This result was confirmed by the FT-IR analysis, which revealed no noticeable change in FT-IR spectra with the immersion in SBF (Figure 4.6). To further support these results, XRD analysis was also performed. As illustrated in Figure 4.8, there was no change in the XRD pattern of the Gt/PCL fiber mat after immersion in SBF for 28 days.

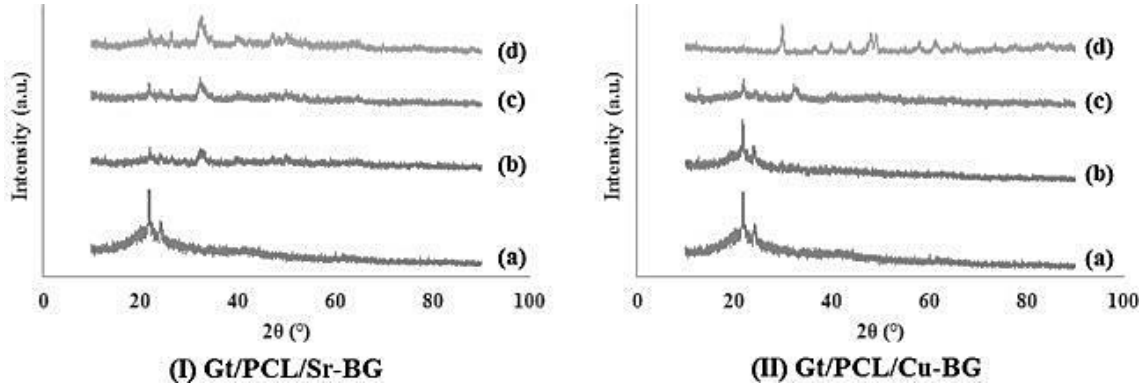

Figure 4.8 : XRD patterns of (I) Gt/PCL/Sr-BG and (II) Gt/PCL/Cu-BG fiber mats, with different BG contents, after immersed in SBF for 28 days: (a) 0 wt%, (b) 2.5 wt%, (c) 5 wt%, and (d) 7.5 wt%.

However, a number of precipitates was present on the surface of Gt/PCL/Sr-BG nanocomposite fiber mats (Figure 4.5(e)). By means of FT-IR spectroscopy, these precipitates were associated with hydroxyapatite since the appearance of the strong band at 1030 cm^{-1} proved the growth of a hydroxyapatite layer. Meanwhile, on the XRD pattern of Gt/PCL/Sr-BG nanocomposite fiber mats, there were two weak diffraction peaks of an apatite-like phase at 34.1° and 25.9°, which corresponded to the (2 0 2) and (0 0 2) crystal planes of apatite. With the increase of BG content, the characteristic peaks of apatite became stronger, which implied that the crystal degree and the amount of

apatite increased. In addition, new peaks at 32.9° (3 0 0), 39.8° (3 1 0), 46.7° (2 2 2), and 49.5° (2 1 3) corresponding to apatite were also observed for Gt/PCL/7.5Sr-BG nanocomposite fiber mat.

On the other hand, no apatite deposition was observed on the Gt/PCL/2.5Cu-BG fiber mat. However, Gt/PCL/5Cu-BG fiber mat exhibited two weak diffraction peaks of an apatite-like phase at 34.1° and 40°, which corresponded to the (2 0 2) and (3 1 0) crystal planes of apatite. With the increase of BG content, the characteristic peaks of apatite became stronger and new peaks at 32.9° (3 0 0), 37° (1 3 0), 39.8° (3 1 0), 46.7° (2 2 2), 49.5° (2 1 3), 53.2° (0 0 4), 61.5° (2 1 4), and 64.1° (3 0 4), corresponding to apatite were emerged for Gt/PCL/7.5Sr-BG nanocomposite fiber mat. These results coincided with the results of FT-IR analysis, revealing the formation of apatite by the presence of the strong band at 1030 cm^{-1}. In addition, the surface morphology of Gt/PCL/7.5Cu-BG nanocomposite fiber mat changed after soaking in SBF for 24 h, and some new tiny materials appeared on the nanofiber surface (Figure 4.5(c)). After prolonged immersion of 4 weeks, these new materials grew and the surface of the nanofibers was almost totally covered with the needle-like layer, as observed in Figure 4.5(f).

Taken together, the incorporated BG particles were proved to stimulate the formation of hydroxyapatite. This is consistent with the previous researches, which demonstrated that the inclusion of the BG particles into the polymeric matrix greatly enhanced the in vitro hydroxyapatite formation on the surface of the nanocomposites under a simulated physiological medium. For instance, Lin et al. [11] found that the incorporation of mesoporous BG into a PCL nanofibrous matrix significantly enhanced its apatite-formation ability in SBF compared with a PCL nanofibrous matrix. Similarly, Allo et al. [137] reported that contrary to control PCL fibrous scaffolds that were devoid of bone-like apatite particles, incubating PCL/BG fibrous scaffolds in SBF revealed bone-like apatite deposition. In addition, Han et al. [158] indicated the higher bioactivity of composite nanofibers compared to pure PAN-based carbon nanofibers. Meanwhile, Yang et al. [15] also reported that the presence of BG nanoparticles in the carbon nanofiber composites had increased the rates of the heterogeneous apatite nucleation. On the other hand, the in vitro bioactivity of the nanocomposite fiber mats increased with the content of BG particles, as previously shown by other researchers [11,14].

Assuming the formation of crystalline hydroxyapatite layer on the fiber mat as the marker of bioactivity, our results indicated that Gt/PCL/7.5Cu-BG fiber mat had the best bioactivity among all of the produced fiber mats. The bioactive materials are capable of bonding with bone through the formation of an apatite interface layer. The mechanism of apatite formation upon contact of bioactive glass with SBF consists of five stages: (1) fast ion exchange of alkali ions with hydrogen ions from the liquid medium; (2) glass network dissolution; (3) silica-gel polymerization; (4 and 5) chemisorption and crystallization of the carbonated hydroxyapatite layer. The detailed analysis of the reactions involved has been presented by Hench [159]. All of the Gt/PCL/Sr-BG fiber mats possessed in vitro bioactivity but at different extents depending on the BG content, while this was not the case for Gt/PCL/Cu-BG fiber mats. No biomineralization behavior was observed for Gt/PCL/Cu-BG fiber mat with a BG content of 2.5 wt%. This result can be explained with the faster degradation rate of Sr-BG as explained above. The faster dissolution of glass network resulted in an early calcium phosphate layer formation.

4.3.7 Investigation of degradation rate

The degradation rate of a scaffold is a key parameter for bone tissue engineering since it should match with the rate of neogenesis of ECM. Therefore, the in vitro biodegradation was studied by measuring the weight loss of the fiber mats in SBF at 37 °C during 4 weeks. After 28 days in SBF, the weight loss was below 5% in the case of Gt/PCL fiber mat, while it was higher (9–16%) in the case of the nanocomposite fiber mats over the same period (**Figure 4.9**). This indicated that the inclusion of BG particles accelerated the degradation rate of the fibrous mats. Similarly, Kouhi et al. [134] reported that the weight loss was only 4% in the case of PCL nanofibers, whereas it was higher in the case of PCL/BG nanocomposite fibers. In addition, they determined that increasing BG concentration from 5% to 20% led to an increase in the weight loss from 21% to 40% after 28 days. It was explained that the incorporation of a glass phase into the PCL matrix increased its capacity to absorb water during the incubation period and, thus, rised its hydrolytic degradation [134].

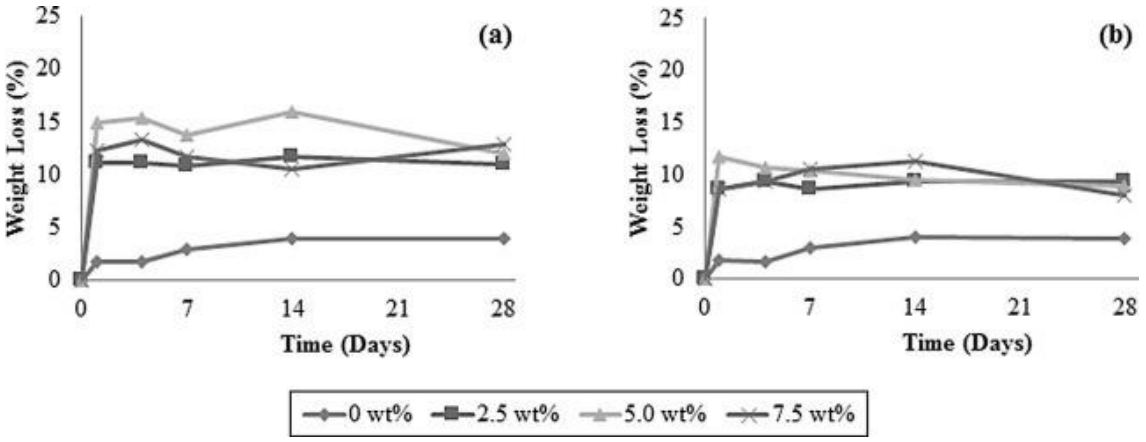

Figure 4.9 : Weight loss of fiber mats as a function of immersion time in SBF: (a) Gt/PCL/Sr-BG and (b) Gt/PCL/Cu-BG fiber mats.

On the other hand, the weight loss was slightly lower when the Cu-BG particles were introduced into the nanofibrous mats instead of Sr-BG particles, which was likely due to the faster degradation rate of Sr-BG compared to that of Cu-BG. The slower degradation of Cu-BG was explained by Wang et al. [160]. They claimed that when CuO was substituted with CaO, the Cu–O bond showed more covalent character compared to the Ca–O bond, resulting in the re-polymerization of Si–NBOs and higher network connectivity. Besides, the substitution of calcium by strontium in the 45S5 composition most likely resulted in a larger expansion of the glass network in order to accommodate the larger strontium cation compared to copper cation. This may lead to a more weakened network in the case of doping with SrO, accelerating the degradation rate of Sr-BG particles.

4.3.8 Determination of release of therapeutic ions

Recently, a variety of studies have been performed to enhance the biological performance of bioactive glasses by doping them with therapeutic ions. It was reported that upon the dissolution of the inorganic matrix, the controlled release of these ions brought about additional functionalities, including osteogenesis, angiogenesis, and antibacterial effects. Therefore, it is of great importance to determine the amount of therapeutic ions released from scaffolds. However, high concentrations of these ions can cause free radical formation and cytotoxicity. Thus, it is necessary to control the release of therapeutic ions at a clinically acceptable rate. Hence, the release of these ions from

the nanocomposite fiber mats when being soaked in SBF was investigated as given in Figure 4.10. Results showed that the release of strontium ions was between 5.4 and 10.1 mg/g scaffold, whereas 0.34–1.87 mg/g scaffold of copper ions was released. The fact that the release of copper ions being lower than those of strontium ions was likely due to the slower degradation of Cu-BG compared to Sr-BG as mentioned before. Although Cu-BG particles degraded more slowly, Gt/PCL/7.5Cu-BG fiber mat displaying the best bioactivity may seem a conflict. However, this was likely the result of the inhibitory effect of strontium ions on hydroxyapatite crystallization. Hoppe et al. [161] speculated that the transformation of the amorphous calcium phosphate layer to hydroxyapatite was delayed as a result of the inhibitory effects of strontium on hydroxyapatite crystallization.

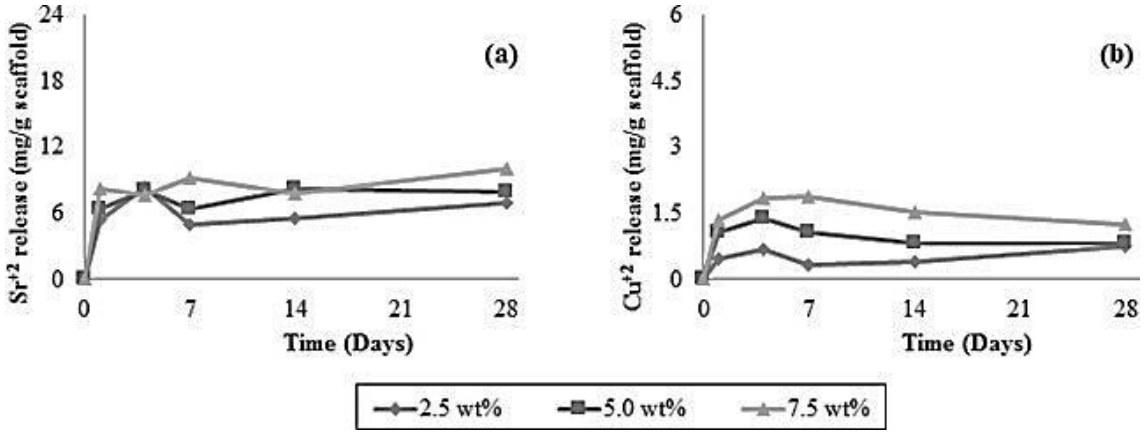

Figure 4.10 : Release of therapeutic ions as a function of immersion time in SBF: (a) Gt/PCL/Sr-BG and (b) Gt/PCL/Cu-BG fiber mats.

On the other hand, recent studies reported that the effective copper ion concentration for stimulating vascularization was 14–57 ppm [162], whereas stimulatory effects were induced on osteoblasts by the release of strontium ion in a range from 8.7 to 87.6 ppm [163–164]. The amounts of ion release obtained in the present study were lower compared to these studies. Therefore, the inclusion of more than 2 wt% SrO and CuO into BG composition may be more suitable in order to exploit the full osteogenic, angiogenic, and antibacterial potential of therapeutic ions without inducing any cytotoxic effects. Though, this work provides a basis for future studies.

4.4 Conclusion

In the present study, bioactive glasses doped with therapeutic metal ions (i.e., strontium or copper) were successfully incorporated into the Gt/PCL fibrous mats by means of electrospinning process. The hydroxyapatite forming ability of fiber mats gives insight into their bioactivity, which is relevant for bone regeneration. Thus, the impact of composition and content of bioactive glass on the mineralization behavior of the fiber mats were evaluated and discussed in detail. These findings indicated that the currently described electrospun nanocomposite fiber mats are very promising scaffolds as they combine the high bioactivity of bioactive glasses, the beneficial effects of therapeutic metallic ions on bone growth and an interconnected porous structure of electrospun nanofibers that may allow cell adhesion, cell invasion and vascularization. However, the addition of more than 2 wt% SrO and CuO into bioactive glass composition may be better to improve the osteogenic, angiogenic, and antibacterial potential of the nanocomposite fiber mats as scaffolds for bone tissue engineering. Within this respect, our observations provide the basis for further studies with regard to fabrication of multifunctional scaffolds for bone tissue engineering applications.

5. FABRICATION OF NANOCOMPOSITE MAT THROUGH INCORPORATING BIOACTIVE GLASS PARTICLES INTO GELATIN/POLY(ε-CAPROLACTONE) NANOFIBERS BY USING BOX–BEHNKEN DESIGN[(*)]

5.1 Introduction

In recent years, tissue engineering has emerged as a promising alternative pathway to conventional strategies in order to repair or replace the damaged organs and lost tissues by using a scaffold as a temporary support that reduces the size of the defect until the tissue has regenerated and remodeled itself naturally [156,165–166]. Using electrospinning, it is possible to produce scaffolds with similar morphology and architectural features to the natural extracellular matrix (ECM) [133,167]. Therefore, numerous electrospinning efforts have been directed in fabricating scaffolds from a wide variety of materials, including polymers, ceramics, and metals, as well as their blends and composites in different ratios [167–168].

The technique of electrospinning is dependent on several types of parameters, including solution parameters (i.e., polymer type, solution concentration, and solvent properties), processing parameters (e.g., applied voltage, distance between tip of syringe and collector, and flow rate), and ambient parameters (i.e., temperature, atmosphere pressure, and relative humidity) [83,169–179]. The biological, mechanical, electrical, and optical properties of electrospun nanofibers can be easily manipulated by altering these electrospinning parameters [62,81]. Since the success of tissue engineering strategies was highly dependent on the properties of scaffold, it is necessary to properly adjust these parameters for achieving a successful electrospinning operation. Therefore, a variety of studies have recently focused on assessing the effects of the electrospinning

[(*)] This chapter is based on the paper: "**Gönen, S. Ö.**, Erol Taygun, M., Aktürk, A., and Küçükbayrak, S. (2016). Fabrication of nanocomposite mat through incorporating bioactive glass particles into gelatin/poly(ε-caprolactone) nanofibers by using box–behnken design. *Materials Science and Engineering: C*, *67*, 684–693."

parameters on the average diameter of electrospun fibers by means of response surface methodology (RSM) based on central composite design [51,78,82,93,95,171–172] and Box–Behnken design [66,68,71,79,83,88,98,169–170,173–178]. For a quadratic response surface model with three or more factors, Box–Behnken design technique is reported to be much more advantageous in comparison to central composite design [68, 170,174–175].

Apart from the surface topography of scaffold, the structural composition of matrix has also influences on the performance of scaffold. This is because a single polymer cannot impart all the required properties to the scaffold. One of the strategies to overcome this notable problem is simply combining variable components, which has become an effective way for developing scaffolds with improved physicochemical and biological properties for tissue engineering applications [35,48,72,107]. In this context, recent studies have assessed the potential of electrospun gelatin/PCL nanofibers for engineering diversified tissues, including nerve [35,125–126], muscle [75], dental [127], cardiac [76], cardiovascular [128], bone [34,129], and cartilage [130–131]. Results showed that blending PCL with gelatin resulted in a new biomaterial with improved mechanical, physical, chemical, and biological properties [35,48,72,107]. For instance, Zhang et al. [48] reported that bone-marrow stromal cells can attach and grow on gelatin/PCL or PCL-alone scaffolds, but the cells spread better and migrate deeper inside gelatin/PCL scaffold. Similarly, Ghasemi-Mobarakeh et al. [173] indicated that nerve cells can attach and grow on PCL/gelatin and PCL nanofibrous scaffolds, but cell proliferation was improved by blending PCL with gelatin. Moreover, gelatin/PCL fibrous membrane was found to exhibit improved mechanical properties as well as more favorable wettability than that obtained from either gelatin or PCL alone [48].

In the open literature, the most common solvents for gelatin/PCL blends were fluorinated alcohols. Nevertheless, the cost, possible toxicity issues and environmental concerns of these solvents made them unsuitable for biomedical applications. Therefore, we have previously evaluated the possibility of preparing electrospun gelatin/PCL nanofibers with the use of an alternative solvent consisting of acetic acid and formic acid **[98]**. In the current study, we aimed to build on that previous work by combining the high bioactivity of bioactive glasses with the beneficial effects of electrospun

gelatin/PCL nanofibers. The reason lying behind that was strategies of bone tissue engineering being relied on incorporating bioactive inorganic particles (i.e., hydroxyapatite, tricalcium phosphate, and bioactive glass) into a polymeric matrix as fillers in order to mimic both the physical architecture and chemical composition of natural bone ECM [7,11,132–133,137,166,168]. Within this type of structural organization, the inorganic component mimics hydroxycarbonate-apatite and the polymer component resembles collagen-rich ECM.

Among the bioactive inorganic particles, bioactive glasses are excellent choices because of their high bioactivity that allows for forming a bone mineral-like hydroxyapatite phase on the material surface which ultimately induces direct bonding with native bone tissue [4,136,168,179–180]. Ever since its introduction by Hench et al. [18], various efforts have been made to utilize this capability of bioactive glasses in combination with different polymers [7,11,137,168]. These efforts showed that the addition of bioactive glasses into a polymeric matrix greatly enhanced the in vitro hydroxycarbonate apatite formation on the surface of nanocomposites under a simulated physiological medium [11,14,136]. Moreover, as the amount of bioactive glasses increased, the in vitro bioactivity of the nanocomposites was improved [11,14]. In addition to an improvement in bioactivity, the incorporation of bioactive glasses also improved mechanical properties (i.e., tensile strength and elongation to failure) [7,139], as well as biological properties (e.g., cellular differentiation and proliferation, alkaline phosphatase activity, and expression of genes associated with the bone regeneration) [11,14,136,138–139].

To the best of authors' knowledge, no published work has attempted to incorporate bioactive glass particles into gelatin/PCL nanofibers as fillers to form nanocomposite mats. Hence, this study concentrated on loading bioactive glass particles into the gelatin/PCL nanofibers by using electrospinning technique to develop a composite scaffold with improved biological and mechanical stability for bone tissue engineering applications. In this context, emphasis has been first placed on employing RSM based on Box-Behnken design as a useful guideline to choose the most appropriate parameter settings to obtain the nanocomposite fibrous mat with targeted fiber diameter. Afterwards, the morphological, structural, and thermal behaviors of the nanocomposite mat were investigated in detail.

5.2 Materials and Methods

5.2.1 Materials

Gelatin (type A, from porcine skin), PCL (M_n = 70,000–90,000), and silicon dioxide (SiO_2, Sigma Aldrich) were obtained from Sigma–Aldrich Chemicals. Glacial acetic acid (AcOH), formic acid, di-sodium hydrogen phosphate anhydrous (Na_2HPO_4), calcium carbonate ($CaCO_3$), and sodium carbonate (Na_2CO_3) were purchased from Merck. All chemicals were in GR grade and were used as provided without further purification.

5.2.2 Preparation of bioactive glass particles

45S5® bioactive glass particles (45 SiO_2 : 24.5 CaO : 6 P_2O_5 : 24.5 Na_2O wt%) were produced using melt-quenching technique. To prepare these particles, appropriate amounts of precursor chemicals were first placed in a platinum crucible. After that, they were melted at 1250 °C for 2 h and rapidly quenched into deionized water to form frits. As-prepared frits were then ground and placed into the platinum crucible for repeating the melting and the quenching steps in order to obtain a homogeneous structure. Finally, the obtained bioactive glass frits were ground ($\leq$ 45 μm) to yield the bioactive glass particles.

5.2.3 Preparation of electrospinning solutions

Bioactive glass particles were first dispersed in a co-solvent of acetic acid and formic acid (1:1 in volume) at room temperature for 1 h. Then, polymers were separately added into the bioactive glass containing solvents and stirred at room temperature for 3 h in order to obtain homogenous solutions with bioactive glass contents varying from 2.5% to 7.5% (w/v). Afterwards, 20% (w/v) gelatin solution and 15% (w/v) PCL solution were mixed in a gelatin/PCL ratio of 7/3 (w/w) at room temperature for 2 h.

5.2.4 Electrospinning

As-prepared solutions were loaded into a syringe, and they were fed from the syringe to a needle tip at a controlled flow rate by a syringe pump. Electrospinning process was performed with the use of an electrospinning device (Nanospinner 24 Touch, Inovenso

Co.) under different parametric modulations of applied voltage, tip-to-collector distance and flow rate as outlined in subsequent sections. The electrospun nanocomposite fibers were accumulated as nonwoven mats on a grounded target wrapped with aluminum foil. All electrospinning experiments were carried out at ambient conditions.

5.2.5 Experimental design

The number of factors that alters the electrospinning process is quite large. Hence, investigating all of them in the framework of one single research is impossible. However, some of these parameters can be held constant during experimental studies in order to minimize the number of experiments required for identifying the significance of each parameter on electrospinning process. In this regard, bioactive glass content, applied voltage, tip-to-collector distance, and flow rate were selected to be the most influential parameters. Whereas, solution parameters (e.g., polymer concentration of both solutions, weight ratio of one polymer to another, and solvent composition) were taken as optimized in our previous study [98].

To find an appropriate range for each parameter, a set of preliminary experiments was conducted. For instance, a bioactive glass content differing from 2.5% to 7.5% (w/v) was preferred in the present study. This is because bioactive glass contents above 7.5% (w/v) brought about fibers with very large diameters, while bioactive glass contents below 2.5% (w/v) would not be high enough. On the other hand, voltages below 20 kV was too low to electrospin all of the solutions, whereas voltages above 25 kV resulted in electrical arcs due to the static potential exceeding the resistance of the enclosed air inside the chamber. In this regard, a voltage between 20 and 25 kV was selected to be the desired domain for applied voltage. Similarly, distances below 7.5 cm led to electrical arcs as observed in high voltages, while electrospinning did not occur in the case of distance being longer than 12.5 cm. Therefore, a tip-to-collector distance varying from 7.5 to 12.5 cm was considered as the effective range for tip-to-collector distance. Moreover, the fiber formation was hindered due to insufficient supply of solution to the tip of the syringe needle when flow rates below 1 mL/h were employed. However, excessive feed of solution gave rise to the choking up of the syringe needle. As a result,

a flow rate ranging from 1 to 3 mL/h was chosen as the favorable range of flow rate in the present study.

The correct strategy to deal with several factors is to use a response surface methodology, which is a combination of mathematical and statistical techniques useful for developing empirical models that depicts the physical behavior of the system in the form of low-order polynomials. Therefore, the planning and analysis of the experiments were performed within the context of response surface methodology.

To capture the interaction between parameters, a quadratic model was employed to establish empirical relationships between four electrospinning parameters (bioactive glass content, applied voltage, tip-to-collector distance, and flow rate) and two responses (average fiber diameter and its standard deviation). This model was expressed as follows in Eq. (5.1):

$$y = C_0 + \sum_{i=1}^{4} C_i X_i + \sum_{i=1}^{4} C_{ii} {X_i}^2 + \sum_{i=1}^{3} \sum_{j=i+1}^{4} C_{ij} X_i X_j \qquad (5.1)$$

where *y* is the predicted response value and *Xi* is the *i*th independent factor. C_0, C_i, C_{ii}, and C_{ij} are the regression coefficients with C_0 being the constant term, C_i being the linear effect term, C_{ii} being the squared effect term, and C_{ij} being the interaction effect term.

For a quadratic model, experiments must be performed for at least three levels of each factor. These levels were chosen equally spaced. Coded and uncoded values of the factors are listed in Table 5.1. − 1, 0, and 1 are coded variables corresponding to low, intermediate and high levels of each factor, respectively.

Table 5.1 : Factors and their levels used in the experimental design.

Factors	Symbol	Levels		
		–1	0	1
Bioactive glass content (% w/v)	X_1	2.5	5	7.5
Applied voltage (kV)	X_2	20	22.5	25
Tip-to-collector distance (cm)	X_3	7.5	10	12.5
Flow rate (mL/h)	X_4	1	2	3

The regression analysis was performed using Minitab 16.0 statistical software (Minitab Inc., State College). The significance of each coefficient was determined from the t-values and p-values. Coefficients in the equation with t-values greater than t-values at 95% level of confidence or p-values being greater than 0.05 were considered statistically significant. The model was further refined by removing the insignificant terms. The accuracy of the model was evaluated by the coefficients of determination (R^2) and the analysis of variances (ANOVA). The predicted values were calculated by using the refined model. The validity of the models was evaluated in order to show the generalization ability of the models for predicting new conditions inside the design space. Contour plots were depicted to visualize the relationships between the responses and the electrospinning parameters. The optimum values of the selected variables were obtained by solving the regression equations and also by analyzing the contour plots. In this work, the optimum electrospun mat was defined as that with the highest bioactive glass content, the lowest diameter and the most homogeneously distributed fiber diameter.

5.2.6 Characterization

The surface morphology and microstructure of the fibrous mats were observed by using a scanning electron microscope (SEM, JSM-5410, Jeol) operated at 20 kV. Prior to the SEM measurements, all of the samples cut from the fibrous mats were coated with platinum under vacuum for 120 s by using a sputter coater (SC7620, Quorum Technologies Ltd) in order to reduce electron charging effects. The diameter of the electrospun fibers was measured by using Image J software (National Institute of Health). For each experiment, average fiber diameter and its standard deviation were determined from 100 measurements of the randomly chosen fibers.

The BET surface area of the fibrous mats were determined by nitrogen adsorption at − 196 °C using a surface analyzer (NOVA 1200, Quantachrome). Prior to gas adsorption experiments, the samples were degassed under vacuum at 100 °C for a period of 1.5 h to remove the adsorbed atmospheric gases from the sample.

The density of the bioactive glass particles and the fibrous mats were measured by gas displacement technique. These measurements were carried out using micrometrics pycnometry system with the use of inert gas, helium.

The amorphous structure of the bioactive glass particles and the characteristic phases of the fibrous mats were identified using an X-ray diffraction analyzer (XRD, D8 Advance, Bruker™) with Cu–Kα radiation. XRD patterns were acquired over a 2θ range from 10° to 90° with a step size of 0.01°.

The functional groups of the bioactive glass particles and the fibrous mats were investigated by Fourier-transform infrared (FT-IR) spectroscopy. FT-IR spectra were collected using a spectrometer (Spectrum 100, Perkin Elmer) with 4 cm^{-1} resolution in transmittance mode in the mid-IR region (4000–650 cm^{-1}).

The thermal behavior of the bioactive glass particles and the fibrous mats were investigated by using a differential thermal analyzer (DTA, Q600 SDT, TA instruments). 4 mg of samples were heated at a rate of 20 °C/min from room temperature to 1000 °C under nitrogen atmosphere.

5.3 Results and Discussion

5.3.1 Development of RSM models

To identify the effect of electrospinning parameters both on average fiber diameter and standard deviation, a Box-Behnken design was employed. Four factors each at three levels resulted in 27 experimental runs including 2 replicates at the center point. The predicted values and the corresponding experimental measurements for fiber diameter and its standard deviation values of each design point were tabulated in Table 5.2.

The primary results of ANOVA test were summarized in Table 5.3. P-values which are related to the estimated coefficients are the statistical measures of significance of each factor in providing the explanation for the unpredictability of the experimental data. A factor has a significant impact on the response when p-value is less than 0.05, while vice versa for p-value being greater than 0.05. Along with these statistics, it can be concluded that the factor appears to be more important when reported at lower p-value.

Table 5.2 : Box–Behnken design matrix and response values for each design point.

Design point	Coded levels of factors				Average fiber diameter (nm)	
	X_1	X_2	X_3	X_4	Experimental	Predicted
1	-1	-1	0	0	448 ± 196	597 ± 246
2	1	-1	0	0	577 ± 250	598 ± 264
3	-1	1	0	0	686 ± 283	664 ± 291
4	1	1	0	0	685 ± 306	665 ± 310
5	0	0	-1	-1	380 ± 164	352 ± 146
6	0	0	1	-1	311 ± 86	321 ± 122
7	0	0	-1	1	345 ± 180	350 ± 146
8	0	0	1	1	305 ± 70	320 ± 122
9	-1	0	0	-1	837 ± 355	696 ± 306
10	1	0	0	-1	580 ± 293	568 ± 325
11	-1	0	0	1	646 ± 332	565 ± 306
12	1	0	0	1	647 ± 327	695 ± 325
13	0	-1	-1	0	374 ± 110	317 ± 86
14	0	1	-1	0	337 ± 90	384 ± 132
15	0	-1	1	0	366 ± 105	287 ± 61
16	0	1	1	0	327 ± 84	354 ± 107
17	-1	0	-1	0	506 ± 277	583 ± 310
18	1	0	-1	0	629 ± 270	584 ± 271
19	-1	0	1	0	534 ± 244	553 ± 227
20	1	0	1	0	545 ± 354	554 ± 304
21	0	-1	0	-1	323 ± 71	365 ± 111
22	0	1	0	-1	389 ± 177	432 ± 157
23	0	-1	0	1	401 ± 147	364 ± 111
24	0	1	0	1	467 ± 214	431 ± 157
25	0	0	0	0	376 ± 154	398 ± 172
26	0	0	0	0	435 ± 190	398 ± 172
27	0	0	0	0	337 ± 130	398 ± 172

For the creation of new models with fewer parameters and better fitting to the experimental results, insignificant terms were removed from the models. From the analysis of variance, the coefficients of the final statistical models and the significance of each term were recalculated, as given in Table 5.4. By elimination of insignificant terms ($p > 0.05$) from the full quadratic model, the mathematical expressions which include a series of linear, quadratic and interaction terms for actual value of each parameter were determined, as follows:

$$Fiber\ diameter = 346.903 - 423.617\,X_1 + 13.4\,X_2 + 193.867\,X_3 - 129.75\,X_4 + 37.2217\,{X_1}^2 - 9.9983\,{X_3}^2 + 25.8\,X_1\,X_4 \quad (5.2)$$

Table 5.3 : Regression coefficients for the response surface model using coded values.

Term		Average fiber diameter*			Standard deviation**		
		Coefficient	t–value	p–value	Coefficient	t–value	p–value
Constant	C_0	382.667	8.451	0.000	158.000	5.927	0.000
X_1	C_1	0.500	0.022	0.983	9.417	0.707	0.493
X_2	C_2	33.500	1.480	0.165	22.917	1.719	0.111
X_3	C_3	-15.250	-0.674	0.513	-12.333	-0.925	0.373
X_4	C_4	-0.750	-0.033	0.974	10.333	0.775	0.453
X_1X_1	C_{11}	238.458	7.022	0.000	149.167	7.461	0.000
X_2X_2	C_{22}	-4.042	-0.119	0.907	-32.583	-1.630	0.129
X_3X_3	C_{33}	-56.667	-1.669	0.121	-32.458	-1.624	0.130
X_4X_4	C_{44}	27.333	0.805	0.437	15.292	0.765	0.459
X_1X_2	C_{12}	-32.500	-0.829	0.423	-7.750	-0.336	0.743
X_1X_3	C_{13}	-28.000	-0.714	0.489	29.250	1.267	0.229
X_1X_4	C_{14}	64.500	1.645	0.126	14.250	0.617	0.549
X_2X_3	C_{23}	-0.500	-0.013	0.990	-0.250	-0.011	0.992
X_2X_4	C_{24}	0.000	0.000	1.000	-9.750	-0.422	0.680
X_3X_4	C_{34}	7.250	0.185	0.856	-8.000	-0.347	0.735

*R^2 = 86.46% and R^2 adjusted = 70.65%; **R^2 = 88.62% and R^2 adjusted = 75.34%.

Table 5.4 : Regression coefficients for the refined model using coded values.

Term		Average fiber diameter*			Standard deviation**		
		Coefficient	t–value	p–value	Coefficient	t–value	p–value
Constant	C_0	398.194	17.715	0.000	171.593	10.069	0.000
X_1	C_1	0.500	0.026	0.980	9.417	0.824	0.420
X_2	C_2	33.500	1.721	0.102	22.917	2.005	0.059
X_3	C_3	-15.250	-0.783	0.443	-12.333	-1.079	0.294
X_4	C_4	-0.750	-0.039	0.970	–	–	–
X_1X_1	C_{11}	232.635	8.727	0.000	144.069	8.911	0.000
X_2X_2	C_{22}	–	–	–	-37.681	-2.331	0.031
X_3X_3	C_{33}	-62.490	-2.344	0.030	-37.556	-2.323	0.031
X_4X_4	C_{44}	–	–	–	–	–	–
X_1X_2	C_{12}	–	–	–	–	–	–
X_1X_3	C_{13}	–	–	–	29.250	1.477	0.156
X_1X_4	C_{14}	64.500	1.913	0.071	–	–	–
X_2X_3	C_{23}	–	–	–	–	–	–
X_2X_4	C_{24}	–	–	–	–	–	–
X_3X_4	C_{34}	–	–	–	–	–	–

*R^2 = 84.14% and R^2 adjusted = 78.30%; **R^2 = 86.74% and R^2 adjusted = 81.86%.

$$Standard\ deviation\ = -2846.89 - 273.544\,X_1 + 280.467\,X_2 + 91.8444X_3 + 23.0511\,{X_1}^2 - 6.0289{X_2}^2 - 6.0089{X_3}^2\ + 4.68\,X_1\,X_3 \quad (5.3)$$

P-values were also used for measuring the statistical significance of the models. The p-values of both models were less than 0.05, indicating that the models were significant at 95% level of confidence.

To confirm the adequacy of the fitted models, coefficient of determination (R^2) which represents the proportion of the total variability that has been explained by the regression model, was investigated. R^2 always increases when a new term is added to the model, regardless of whether introducing more terms is statistically significant or not. On the other hand, the adjusted form of R^2, Adj-R^2, is much less sensitive to the degrees of freedom and cannot be seriously affected by including more terms into the model. Therefore, Adj-R^2 increases only if the new terms enhance the model and it decreases if unnecessary terms are introduced. Higher values of R^2 and Adj-R^2 indicate how properly the model matches with the experimental results. In the light of this knowledge, it was revealed that the variation in the fiber diameter and its standard variation were explained reasonably well by the RSM approximation.

For evaluating the model associated errors, the lack of fit which compares the residual error (from model error) to the pure error (from replicated experiments), was computed, as shown in Table 5.5. Significant lack of fit indicates that the model does not adequately fit the experimental data. Thus, the p-values for lack of fit being greater than 0.05, confirmed the adequacy of the fitted models.

Table 5.5 : Summary of the ANOVA results for the refined model.

	Average fiber diameter		Standard deviation	
	F–value	p–value	F–value	p–value
Regression	14.40	0.000	17.76	0.000
Linear	0.89	0.487	1.95	0.155
Square	46.79	0.000	38.76	0.000
Interaction	3.66	0.071	2.18	0.156
Lack-of-Fit	1.97	0.389	2.61	0.092

5.3.2 Validation of RSM models

Following the estimation of the models correspondence to the experimental data, the next step in process is the verification of the developed models. The objective of this validation was to show that the models had good capabilities in the description of the selected response changes in the design space. For achieving this goal, additional experiments were conducted within the range of levels defined already. As shown in Table 5.6, the experimental measurements were in close agreement with the predicted values, which were calculated by using mathematical models derived in the current study. Hence, it was confirmed that each individual model showed a capacity to predict the fiber diameter and its standard deviation accurately.

Table 5.6 : Results of the validation experiments.

Trial number	Uncoded levels of factors				Average fiber diameter (nm)	
	X_1	X_2	X_3	X_4	Experimental	Predicted
1	2.5	25	12.5	3	508 ± 291	521 ± 212
2	5	20	7.5	1	316 ± 97	318 ± 86
3	5	25	12.5	3	298 ± 101	353 ± 107
4	5	20	10	2	337 ± 90	365 ± 111
5	7.5	25	12.5	1	584 ± 337	523 ± 290

5.3.3 Visualization of contour plots

A contour plot is the 2D display of a surface plot, which is a theoretical 3D plot that illustrates the relationship between response and independent variables. Therefore, the contour plots are employed to assess the impact of the electrospinning parameters on fiber diameter, to estimate the fiber diameter for an experimental condition inside the design space, and to specify the optimum conditions that results in fabricating mats with desired fiber diameter.

5.3.3.1 Assessing contour plot for fiber diameter

The influence of bioactive glass content on fiber diameter is presented in Figure 5.1(a), (b), and (c). As depicted in these figures, keeping one or more of the other parameters constant, an increase in the bioactive glass content decreases fiber diameter until a threshold limit. However, as the bioactive glass content exceeds a limit, fiber diameter increases with the bioactive glass content. This is presumably attributed to the

competition between viscosity and conductivity. As the bioactive glass content increases from 2.5% (w/v) to 7.5% (w/v), the zero shear viscosity of electrospinning solutions increases from 0.940 Pa·s to 1.256 Pa·s, while conductivity rises from 1408.2 μS/cm to 4487.8 μS/cm. In general, higher viscosity and lower conductivity tend to yield fibers with thicker diameter. Therefore, when the effect of conductivity is more dominant than that of viscosity, the increase in bioactive glass content induces the production of thinner fibers. Otherwise, fiber diameter increases with bioactive glass content.

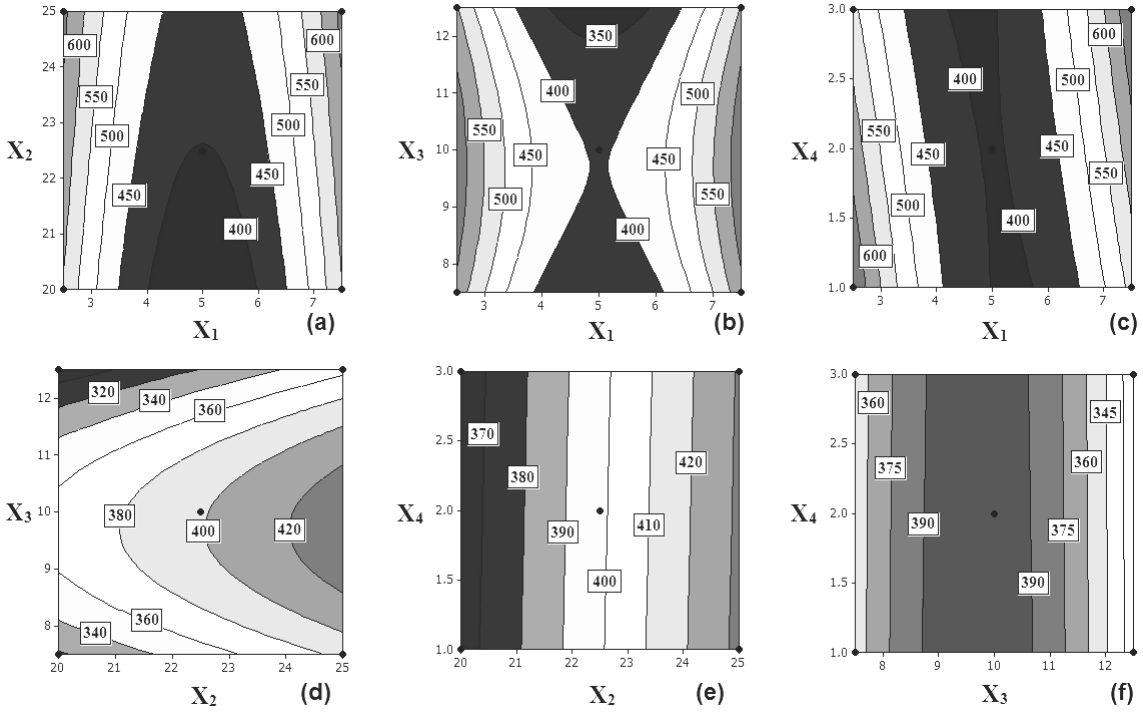

Figure 5.1 : Contour plots of electrospinning parameters for fiber diameter.

The effect of applied voltage on fiber diameter is shown in Figure 5.1(a), (d), and (e). As demonstrated in these figures, studying with high voltages leads to a slight increase in fiber diameter regardless of the other electrospinning parameters. Thus, applied voltage had no interaction with the other electrospinning parameters, which proves the absence of terms X_1X_2, X_2X_3 and X_2X_4 in the model of fiber diameter.

The impact of tip-to-collector distance on fiber diameter is given in Figure 5.1(b), (d), and (f). As observed in these figures, keeping one or more of the other parameters constant, fiber diameter increases with tip-to-collector distance until a threshold limit. Above this limit, the influence of tip-to-collector distance is totally reversed and fibers

with thinner diameters are obtained as tip-to-collector distance increases. This trend can be explained by the dual effect of tip-to-collector distance. On the one hand, employing longer distances favors the formation of thicker fibers as a result of a decrease in the electric field intensity [88]. On the other hand, increasing tip-to-collector distance extends the flight time of fluid jet, which ultimately brings about fibers with thinner diameter because of a longer flight time being prone to more stretching [66,88]. The competition between these two effects determines the variation in fiber diameter.

The effect of flow rate on fiber diameter is presented in Figure 5.1(c), (e), and (f). As depicted in these figures, the effect of flow rate is not always the same. When applied voltage and/or tip-to-collector distance are kept constant, fiber diameter remains almost constant with the increase in flow rate. On the other hand, the impact of flow rate on fiber diameter is highly depended on bioactive glass content. At low bioactive glass contents, operating with faster flow rate leads to the formation of thinner fibers, whereas at high bioactive glass contents, the effect of flow rate is totally reversed and fiber diameter increases with the flow rate. This means that the effect of flow rate on fiber diameter is only altered by bioactive glass content, implying the interaction of flow rate with bioactive glass content, which agrees with the presence of the term X_1X_4 in the model of fiber diameter.

5.3.3.2 Assessing contour plot for standard deviation

The influence of bioactive glass content on standard deviation is presented in Figure 5.2(a) and (b). As depicted in these figures, keeping one or more of the other parameters constant, an increase in the bioactive glass content decreases standard deviation until a threshold limit. However, as the bioactive glass content exceeds this limit, standard deviation increases with the bioactive glass content.

The effect of applied voltage on standard deviation is shown in Figure 5.2(a) and (c). As demonstrated in these figures, studying with high voltages leads to a slight increase in fiber diameter when bioactive glass content is remained constant. However, keeping tip-to-collector distance constant, fibers with larger standard deviation are obtained with the increase in applied voltage until a threshold limit, above which a reverse trend is observed.

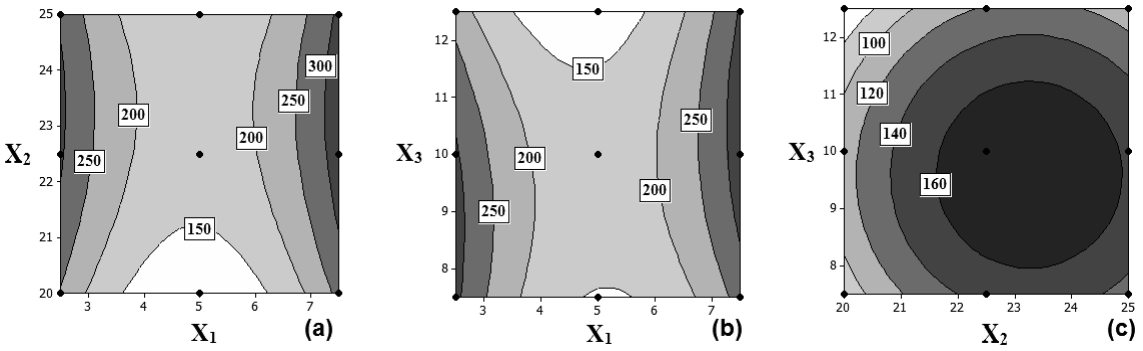

Figure 5.2 : Contour plots of electrospinning parameters for standard deviation.

The impact of tip-to-collector distance on standard deviation is given in Figure 5.2(b) and (c). As observed in these figures, the effect of tip-to-collector distance is not always the same. When applied voltage is kept constant, standard deviation increases with tip-to-collector distance until a threshold limit. Above this limit, the impact of tip-to-collector distance is totally reversed and fibers with narrower standard deviation are obtained as tip-to-collector distance increases. On the other hand, the influence of tip-to-collector distance on standard deviation is highly depended on bioactive glass content. At low bioactive glass contents, employing longer distances leads to the formation of fibers with narrower standard deviation, whereas at high bioactive glass contents, the effect of tip-to-collector distance is totally reversed and standard deviation increases with the tip-to-collector distance. This means that the influence of tip-to-collector distance on standard deviation is only altered by bioactive glass content, implying the interaction of tip-to-collector distance with bioactive glass content, which agrees with the presence of the term X_1X_3 in the model of standard deviation.

5.3.4 Characterization

5.3.4.1 Surface properties

As mentioned before, the main goal of this study was to identify the conditions that yield the electrospun mat with the highest bioactive glass content, the lowest diameter and the most homogeneously distributed fiber diameter. Within this respect, the best condition was estimated to be 7.5% (w/v), 25 kV, 12.5 cm and 1 mL/h in terms of bioactive glass content, applied voltage, tip-to-collector distance and flow rate, respectively, in comparison with the other conditions existing in the design space. For this condition, the

predicted value calculated by the response model was 584 ± 337 nm. This data was in a good match with experimental data of 523 ± 290 nm, further confirming the high reliability of the models. The fabrication of many different sized nanocomposite fibers has been reported by other researchers in the open literature. Some of them were in the size of 161–281 nm [127], 411–483 nm [168], and 0.12–3.0 μm [132] when electrospinning was conducted with different solutions and processing parameters.

Previous studies have demonstrated that the large specific surface area of electrospun nanofibers combined with their interconnected porous structures enhanced the osteogenic potential of scaffolds [11,137]. This is because interconnected pores provide spacing for the vasculature required to nourish new bone and to remove waste products, while the large specific surface area favors cell adhesion, proliferation, migration, and differentiation. For this reason, surface topography of the optimized nanocomposite mat was evaluated by using SEM analysis. SEM micrograph, given in Figure 5.3(a), revealed that the optimized nanocomposite mat was composed of randomly oriented, uniform, and bead free nanofibers. In comparison, a well-developed fibrous morphology with good electrospinnability has been reported to be obtained for gelatin/PCL nanofiber mat, with an average fiber diameter of 346 ± 67 nm [181].

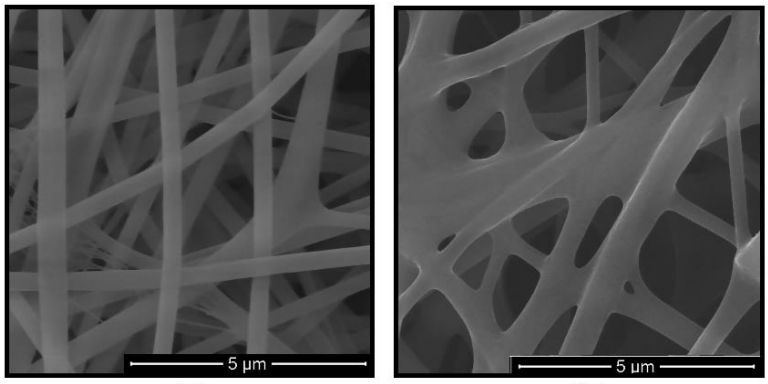

Figure 5.3 : SEM images of (a) nanocomposite mat and (b) gelatin/PCL mat.

BET and density analysis were also used to further characterize the fibrous mats and the bioactive glass particles. Nanocomposite mat gave a specific surface area of 1.81 m^2/g and a density of 1.39 g/cm^3, while gelatin/PCL nanofibrous mat was found to have a specific surface area of 7.40 m^2/g and a density of 1.53 g/cm^3. These results indicated

that the increase of fiber diameter reduces specific surface area and density. Meanwhile, bioactive glass particles had a specific surface area of 0.79 m^2/g and a density of 2.89 g/cm^3.

5.3.4.2 X-ray difraction analysis

XRD measurements were performed to examine the crystalline structure of the nanocomposite fibrous mat. In general, gelatin shows no peak in XRD pattern, which indicates its amorphous nature. While, PCL displays a sharp peak at 2θ of 21.4° and a relatively low intensity peak at 23.6°, indicating the crystalline nature of PCL. Therefore, the presence of the characteristic peaks of PCL (Figure 5.4(a)) confirmed the crystalline nature of the nanocomposite fibrous mat. In comparison, the intensity of PCL peaks was lower in the case of gelatin/PCL nanofibrous mat (Figure 5.4(b)), implying that the degree of crystallinity of the nanocomposite fibrous mat was higher than that of the gelatin/PCL nanofibrous mat. Normally, an opposite trend is expected because of the amorphous nature of the bioactive glass particles, which was confirmed by a broad hump in between 20 and 40 degrees (Figure 5.4(c)). However, measurements were not consistent with the expectations. In the literature, it was put forth that the crystallinity can be changed by the application of an electric field [182]. In this context, this inconsistency is likely due to the applied voltage that generated nanocomposite fibrous mat being higher (25 kV) compared to the applied voltage that yielded gelatin/PCL nanofibrous mat (20 kV [181]). On the other hand, it was also confirmed that bioactive glass particles loaded into the fibers retained their amorphous structure after electrospinning process, since no additional peak other than the peaks of PCL was observed for the nanocomposite fiber mat.

5.3.4.3 FT-IR analysis

FT-IR analysis was performed to identify the surface properties of the nanocomposite fibrous mat. The common bands of PCL appeared at 2949 cm^{-1} (asymmetric CH_2 stretching), 2865 cm^{-1} (symmetric CH_2 stretching), 1727 cm^{-1} (carbonyl stretching), 1293 cm^{-1} (C–O and C–C stretching), 1240 cm^{-1} (asymmetric C–O–C stretching), and 1170 cm^{-1} (symmetric C–O–C stretching) [156,167]. On the other hand, the characteristic bands of gelatin are 3443 cm^{-1} (N–H stretching of amide bond),

1650 cm^{-1} (C═O stretching of amide I), and 1540 cm^{-1} (coupling of N–H bending and C–N stretching) [77,155,167,183]. According to Figure 5.5(a), the nanocomposite mat had the characteristic bands of gelatin and PCL, confirming the presence of both polymers in the structure of nanocomposite mat after electrospinning process. In comparison, these characteristic bands were also present in the FT-IR spectra of gelatin/PCL nanofibrous mat (Figure 5.5(b)). The only difference between these two spectra was the presence of additional bands near 800 cm^{-1} (Si–O–Si symmetric stretching) and 1070 cm^{-1} (Si–O–Si asymmetric stretching) in the FT-IR spectra of nanocomposite mat [10,146,184]. These bands were also present in the FTIR spectra of the bioactive glass particles, as shown in Figure 5.5(c). This indicated that bioactive glass particles were successfully incorporated into the polymeric matrix.

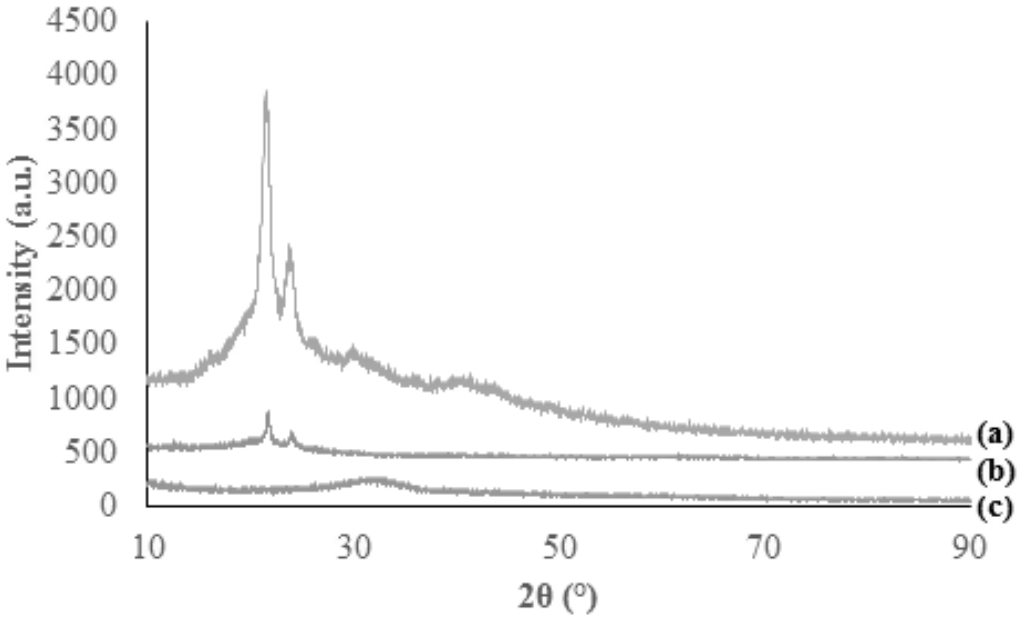

Figure 5.4 : XRD patterns of (a) nanocomposite mat, (b) gelatin/PCL mat, and (c) bioactive glass particles.

5.3.4.4 Thermal behavior

The thermal behavior of the nanocomposite fibrous mat was evaluated by thermogravimetric and differential thermal analysis in a range of 25–1000 °C. In the DTA thermogram of the nanocomposite fibrous mat, there was an endothermic peak with a maximum at 67 °C (Figure 5.6(a)), which was related to the melting of the semicrystalline PCL [155,168]. The same peak also existed in the thermogram of the

gelatin/PCL mat, with the difference that its place has slightly shifted to 60 °C (Figure 5.6(b)). Besides, there was an additional endothermic peak at 207 °C which can be attributed to triple helix to random coil transition. However, there was no evidence of transition of helix to coil conformation of gelatin in the case of nanocomposite mat (Figure 5.6(a)), indicating random coil conformation of gelatin molecules. Depending on the external conditions, gelatin molecules can either take random coil or helix conformation. It is evident from the literature that the helix conformation of gelatin molecules may occur in water-based solutions or neutralized to some degree acidic solutions, while acidic conditions or fluorinated alcohols may lead to gelatin molecules to be in coil conformation [165].

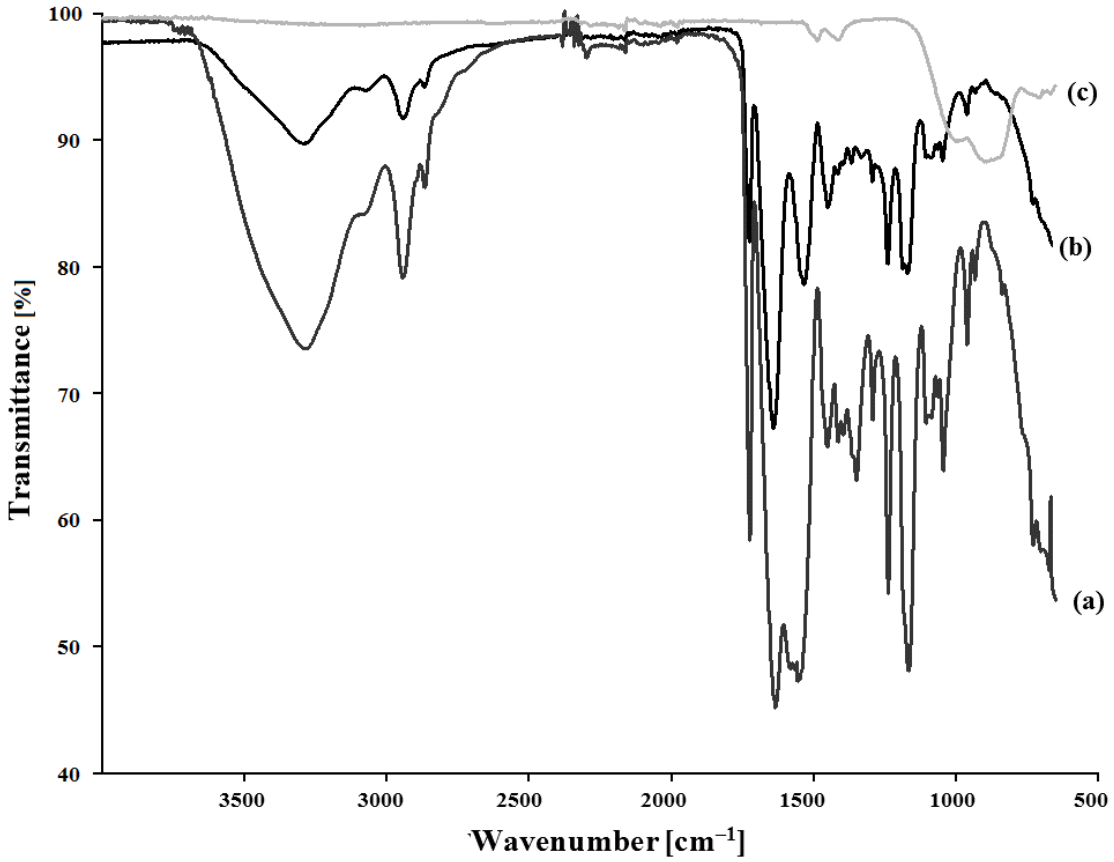

Figure 5.5 : FT-IR spectra of (a) nanocomposite mat, (b) gelatin/PCL mat, and (c) bioactive glass particles.

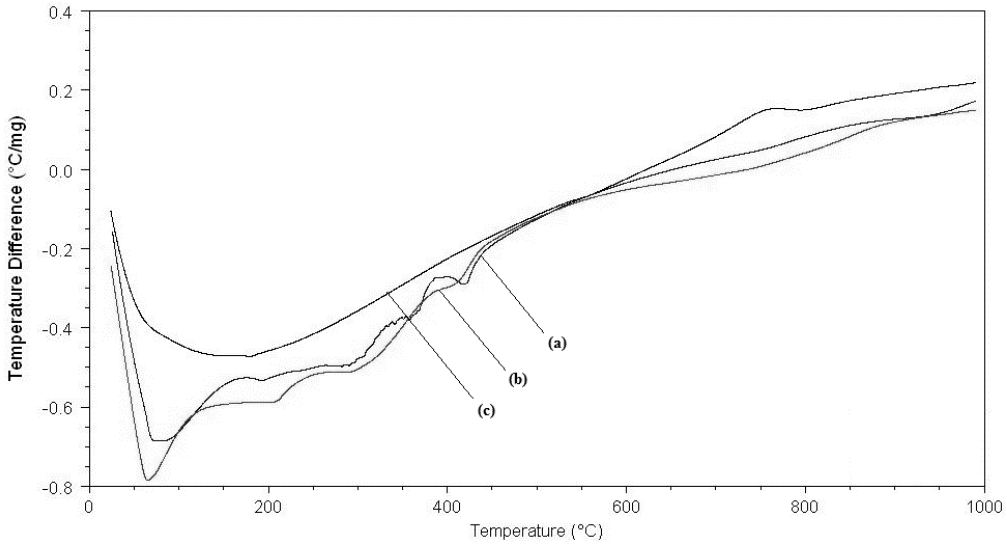

Figure 5.6 : DTA diagram of (a) nanocomposite mat, (b) gelatin/PCL mat, and (c) bioactive glass particles.

On the other hand, the DTG thermograms of fibrous mats were also investigated. For both fibrous mats, the initial weight loss occurred in the temperature range of 25–150 °C, which was related to the loss of absorbed and bound water. Weight loss in this temperature range was about 10%. As depicted in Figure 5.7(a), the thermal degradation of nanocomposite mat was single-stage, which started at around 200 °C and almost completed at 550 °C. In comparison, gelatin/PCL mat underwent a two-stage thermal degradation (Figure 5.7(b)). The first stage was observed in the temperature range of 240 °C–364 °C, which was likely accompanied by breaking of peptide bonds. While, the second stage was found to be between 364 °C and 560 °C, which can be attributed to the decomposition of PCL. The change from two-stage thermal degradation to single-stage degradation with the addition of bioactive glass particles was presumably due to the presence of molecular interactions, implying the success of the composite fabrication.

Finally, the thermal behavior of the bioactive glass particles was also assessed to determine their characteristic temperatures, including glass transition and crystallization temperatures. According to the DTA thermogram of the glass samples given in Figure 5.6(c), the glass transition temperature of bioactive glass particles was 553 °C, whereas crystallization temperature was 754 °C which showed the crystallization ability of the glass.

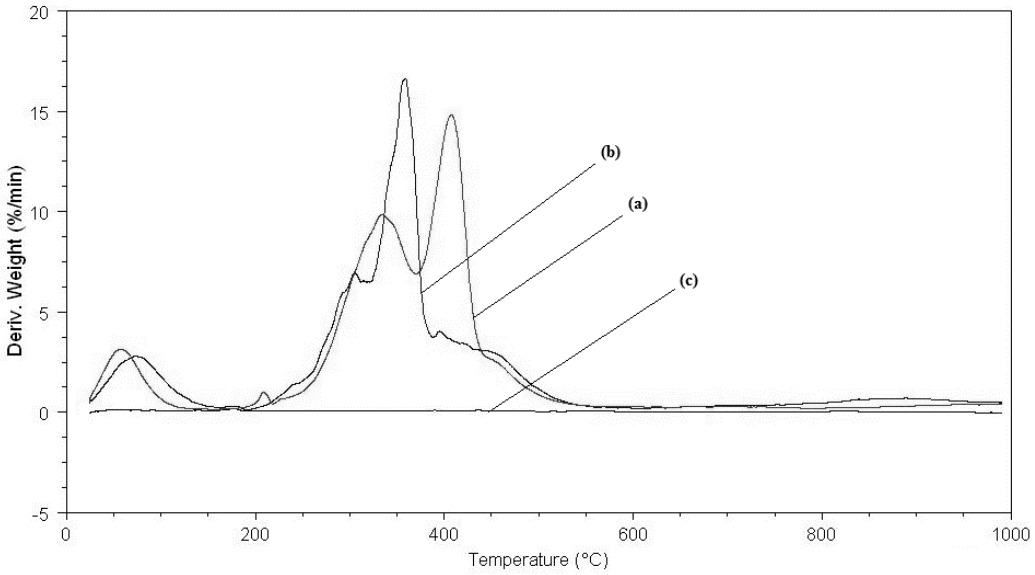

Figure 5.7 : DTG diagram of (a) nanocomposite mat, (b) gelatin/PCL mat, and (c) bioactive glass particles.

5.4 Conclusion

In this study, nanocomposite fibrous mats consist of gelatin, PCL, and 45S5® bioactive glass particles were fabricated through electrospinning technique. Processing and solution parameters were optimized to determine the domain of the parameters where targeted fiber diameter can be achieved. Within this respect, response surface methodology based on a three-level, four-variable Box-Behnken design was employed. Analysis of fiber diameter and its standard deviation as a function of electrospinning parameters showed that a bioactive glass content of 7.5% (w/v) with an applied voltage of 25 kV, a tip-to-collector distance of 12.5 cm, and a flow rate of 1 mL/h gave rise to nanocomposite fibers with desired fiber diameter. The optimized nanocomposite mat was further evaluated by X-ray diffraction analysis, Fourier transform infrared spectroscopy, and differential thermal analyzer. Results put forth the successful incorporation of bioactive glasses into the polymeric matrix, as well as a well-developed fibrous morphology. The findings of this study indicated that the nanocomposite mat with the controlled fiber diameter may serve as a potential candidate of bone tissue engineering scaffold. Future efforts will be focused on in vitro studies to investigate the performance of these functional scaffolds under conditions relevant to applications in bone tissue engineering.

6. CONCLUSIONS AND RECOMMENDATIONS

Creating an excellent scaffold is the challenge of tissue engineering. Therefore, polymer/bioactive glass nanocomposite scaffolds fabricated by electrospinning technique were aimed to be designed, characterized and investigated in vitro in this PhD thesis. Since solution properties (i.e., polymer concentration and solvent composition) and processing variables (e.g., applied voltage, tip-to-collector distance, and flow rate) affect the electrospinnability of polymer solutions and the microarchitectures of the resulting nanofibrous scaffolds, these factors were first optimized to fabricate scaffolds having appropriate properties for bone tissue engineering applications. In this context, response surface methodology based on Box-Behnken design technique was used to model the resultant diameter of the as-spun nanofibers. First two articles given in this thesis described the relationship between the fiber diameter and the solution properties. The results of these studies are listed below:

- Gelatin/PCL nanofibers with diameters ranging from 80 to 250 nm were produced depending on the solution properties. The highest PCL concentration (15% w/v) coupled with the highest gelatin concentration (20% w/v) and the highest content of gelatin solution in the blend solution (70 wt %) resulted in the production of nanofibers with the largest diameter. However, there was no strong statistical evidence that the content of acetic acid in the overall solvent had significant impact on the average fiber diameter.
- The average diameters of the gelatin/sodium alginate nanofibers were 68–166 nm and 90–155 nm in the absence and presence of ethanol, respectively. Highest gelatin concentration (20% w/v) coupled with the lowest content of alginate solution in the blend solution (10 vol%) and the highest content of acetic acid in the solvent of gelatin solution (80 vol%) brought about nanofibers with the largest diameter both in the absence and presence of ethanol. However, the impact of alginate concentration displayed reverse trends for both cases. Lower

alginate concentration led to nanofibers with thicker diameter in the absence of ethanol, whereas the increase in higher alginate concentration resulted from the higher alginate concentration.

The following studies were organized for the purpose of fabricating nanocomposite fibrous mats for bone tissue engineering. For this purpose, strontium or copper doped bioactive glass particles were successfully incorporated into gelatin/poly(ε-caprolactone) (Gt/PCL) nanofibers through electrospinning process. The hydroxyapatite forming ability of fiber mats gives insight into their bioactivity, which is relevant for bone regeneration. Thus, the impact of composition and content of bioactive glass on the mineralization behavior of the fiber mats were evaluated. The results of this study are summarized below:

- The average diameter and in vitro bioactivity of the fiber mats increased with the inclusion of bioactive glass particles into the polymeric matrix.
- The releases of therapeutic ions were in the range of 5.4–10.1 mg/g scaffold and 0.34–1.87 mg/g scaffold for strontium and copper ions, respectively.
- To increase the amount of therapeutic ion release from the scaffolds, more than 2 wt% SrO and CuO can be introduced into bioactive glass composition. In this way, the osteogenic, angiogenic, and antibacterial potential of the nanocomposite fiber mats can possibly be improved.

Additionally, we fabricated nanocomposite fibrous mats consist of gelatin, PCL, and 45S5® bioactive glass particles through electrospinning technique. Processing and solution parameters (bioactive glass content, applied voltage, tip-to-collector distance, and flow rate) were optimized to determine the domain of the parameters where targeted fiber diameter can be achieved. Similarly, response surface methodology was employed as an optimization method to choose the most appropriate parameter settings to obtain the gelatin/sodium alginate/bioactive glass nanocomposite mats with targeted fiber diameter. Besides, strontium or copper doped bioactive glass particles were successfully incorporated into gelatin/sodium alginate nanofibers through electrospinning process, as well. Since these studies are submitted manuscripts, they were not introduced into this PhD thesis.

REFERENCES

[1] Gu, Z., Xie, H., Li, L., Zhang, X., Liu, F., and Yu, X. (2013). Application of strontium-doped calcium polyphosphate scaffold on angiogenesis for bone tissue engineering. *Journal of Materials Science: Materials in Medicine*, *24* (5), 1251–1260.

[2] Wang, X., Wang, Y., Li, L., Gu, Z., Xie, H., and Yu, X. (2014). Stimulations of strontium-doped calcium polyphosphate for bone tissue engineering to protein secretion and mRNA expression of the angiogenic growth factors from endothelial cells in vitro. *Ceramics International*, *40* (5), 6999–7005.

[3] Kapoor, S., Goel, A., Pascual, M.J., and Ferreira, J. M. F. (2013). Thermo-mechanical behaviour of alkali free bioactive glass-ceramics co-doped with strontium and zinc. *Journal of Non-Crystalline Solids*, *375*, 74–82.

[4] Erol, M., Özyuğuran, A., Özarpat, Ö., and Küçükbayrak, S. (2012). 3D composite scaffolds using strontium containing bioactive glasses. *Journal of the European Ceramic Society*, *32* (11), 2747–2755.

[5] Chen, Y. W., Feng, T., Shi, G. Q., Ding, Y. L., Yu, X. X., Zhang, X. H., Zhang, Z. B., and Wan, C. X. (2008). Interaction of endothelial cells with biodegradable strontium-doped calcium polyphosphate for bone tissue engineering. *Applied Surface Science*, *255* (2), 331–335.

[6] Chen, Y. W., Shi, G. Q., Ding, Y. L., Yu, X., Zhang, X. H., Zhao, C. S., and Wan, C. X. (2008). In vitro study on the influence of strontium-doped calcium polyphosphate on the angiogenesis-related behaviors of HUVECs. *Journal of Materials Science: Materials in Medicine*, *19* (7), 2655–2662.

[7] Gao, C., Gao, Q., Li, Y., Rahaman, M. N., Teramoto, A., and Abe, K. (2013). In vitro evaluation of electrospun gelatin-bioactive glass hybrid scaffolds for bone regeneration. *Journal of Applied Polymer Science*, *127* (4), 2588–2599.

[8] Gao, C., Gao, Q., Li, Y., Rahaman, M. N., Teramoto, A., and Abe, K. (2012). Preparation and in vitro characterization of electrospun PVA scaffolds coated with bioactive glass for bone regeneration. *Journal of Biomedical Materials Research Part A*, *100* (5), 1324–1334.

[9] Allo, B. A., Rizkalla, A. S., and Mequanint, K. (2010). Synthesis and electrospinning of ε-polycaprolactone-bioactive glass hybrid biomaterials via a sol-gel process. *Langmuir*, *26* (23), 18340–18348.

[10] Lu, H., Zhang, T., Wang, X. P., and Fang, Q. F. (2009). Electrospun submicron bioactive glass fibers for bone tissue scaffold. *Journal of Materials Science: Materials in Medicine*, *20* (3), 793–798.

[11] Lin, H. M., Lin, Y. H., and Hsu, F. Y. (2012). Preparation and characterization of mesoporous bioactive glass/polycaprolactone nanofibrous matrix for bone tissues engineering. *Journal of Materials Science: Materials in Medicine*, *23* (11), 2619–2630.

[12] Bretcanu, O., Misra, S. K., Yunos, D. M., Boccaccini, A. R., Roy, I., Kowalczyk, T., Blonski, S., and Kowalewski, T. A. (2009). Electrospun nanofibrous biodegradable polyester coatings on Bioglass®-based glass-ceramics for tissue engineering. *Materials Chemistry and Physics*, *118* (2), 420–426.

[13] Jegal, S. H., Park, J. H., Kim, J. H., Kim, T. H., Shin, U. S., Kim, T. I., and Kim, H. W. (2011). Functional composite nanofibers of poly(lactide–co-caprolactone) containing gelatin–apatite bone mimetic precipitate for bone regeneration. *Acta Biomaterialia*, *7* (4), 1609–1617.

[14] Kim, H. W., Lee, H. H., and Chun, G. S. (2008). Bioactivity and osteoblast responses of novel biomedical nanocomposites of bioactive glass nanofiber filled poly(lactic acid). *Journal of Biomedical Materials Research Part A*, *85* (3), 651–663.

[15] Yang, Q., Sui, G., Shi, Y. Z., Duan, S., Bao, J. Q., Cai, Q., and Yang, X. P. (2013). Osteocompatibility characterization of polyacrylonitrile carbon nanofibers containing bioactive glass nanoparticles. *Carbon*, *56*, 288–295.

[16] Xia, W., Zhang, D., and Chang, J. (2007). Fabrication and in vitro biomineralization of bioactive glass (BG) nanofibers. *Nanotechnology*, *18* (13), 135601.

[17] Kim, H. W., Kim, H. E., and Knowles, J. C. (2006). Production and potential of bioactive glass nanofibers as a next-generation biomaterial. *Advanced Functional Materials*, *16* (12), 1529–1535.

[18] Hench, L. L., Splinter, R. J., Allen, W. C., and Greenlee, T. K. (1971). Bonding mechanisms at the interface of ceramic prosthetic materials. *Journal of Biomedical Materials Research Part A*, *5* (6), 117–141.

[19] Hild, N., Tawakoli, P. N., Halter, J. G., Sauer, B., Buchalla, W., Stark, W. J., and Mohn, D. (2013). pH-dependent antibacterial effects on oral microorganisms through pure PLGA implants and composites with nanosized bioactive glass. *Acta Biomaterialia*, *9* (11), 9118–9125.

[20] Jo, J. H., Lee, E. J., Shin, D. S., Kim, H. E., Kim, H. W., Koh, Y. H., and Jang, J. H. (2009). In vitro/in vivo biocompatibility and mechanical properties of bioactive glass nanofiber and poly(ε-caprolactone) composite materials. *Journal of Biomedical Materials Research Part B: Applied Biomaterials*, *91* (1), 213–220.

[21] Liu, F., Zhang, X., Yu, X., Xu, Y., Feng, T., and Ren, D. (2011). In vitro study in stimulating the secretion of angiogenic growth factors of strontium-doped calcium polyphosphate for bone tissue engineering. *Journal of Materials Science: Materials in Medicine*, *22* (3), 683–692.

[22] Fielding, G. A., Smoot, W., and Bose, S. (2014). Effects of SiO_2, SrO, MgO, and ZnO dopants in tricalcium phosphates on osteoblastic Runx2 expression. *Journal of Biomedical Materials Research Part A*, *102* (7), 2417–2426.

[23] Lacroix, J., Lao, J., Nedelec, J. M., and Jallot, E. (2013). Micro PIXE-RBS for the study of Sr release at bioactive glass scaffolds/biological medium interface. *Nuclear Instruments and Methods in Physics Research B*, *306*, 153–157.

[24] Su, W. T., Wu, P. S., Ko, C. S., and Huang, T. Y. (2014). Osteogenic differentiation and mineralization of human exfoliated deciduous teeth stem cells on modified chitosan scaffold. *Materials Science and Engineering C*, *41*, 152–160.

[25] Xie, H., Wang, J., Li, C., Gu, Z., Chen, Q., and Li, L. (2013). Application of strontium doped calcium polyphosphate bioceramic as scaffolds for bone tissue engineering. *Ceramics International*, *39* (8), 8945–8954.

[26] Gu, Z., Zhang, X., Li, L., Wang, Q., Yu, X., and Feng, T. (2013). Acceleration of segmental bone regeneration in a rabbit model by strontium-doped calcium polyphosphate scaffold through stimulating VEGF and bFGF secretion from osteoblasts. *Materials Science and Engineering C*, *33* (1), 274–281.

[27] Gu, Z., Wang, H., Li, L., Wang, Q., and Yu, X. (2012). Cell-mediated degradation of strontium-doped calcium polyphosphate scaffold for bone tissue engineering. *Biomedical Materials*, *7* (6), 065007.

[28] DeVoe, K., Banerjee, S., Roy, M., Bandyopadhyay, A., and Bose, S. (2012). Resorbable tricalcium phosphates for bone tissue engineering: influence of SrO doping. *Journal of the American Ceramic Society*, *95* (10), 3095–3102.

[29] Shen, Y., Liu, W., Lin, K., Pan, H., Darvell, B. W., Peng, S., Wen, C., Deng, L., Lu, W. W., and Chang, J. (2011). Interfacial pH: a critical factor for osteoporotic bone regeneration. *Langmuir*, *27* (6), 2701–2708.

[30] Amina, M., Hassan, M. S., Musayeib, N. M. A., Amna, T., and Khil, M. S. (2014). Improved antibacterial activity of HAP garlanded PLGA ultrafine fibers incorporated with CuO: synthesis and characterization. *Journal of Sol-Gel Science and Technology*, *71* (1), 43–49.

[31] Erol, M. M., Mourino, V., Newby, P., Chatzistavrou, X., Roether, J. A., Hupa, L., and Boccaccini, A. R. (2012). Copper-releasing, boron-containing bioactive glass-based scaffolds coated with alginate for bone tissue engineering. *Acta Biomaterialia*, *8* (2), 792–801.

[32] Tripathi, A., Saravanan, S., Pattnaik, S., Moorthi, A., Partridge, N. C., and Selvamurugan, N. (2012). Bio-composite scaffolds containing chitosan/nano-hydroxyapatite/nano-copper–zinc for bone tissue engineering. *International Journal of Biological Macromolecules*, *50* (1), 294–299.

[33] Gerard, C., Bordeleau, L. J., Barralet, J., and Doillon, C. J. (2010). The stimulation of angiogenesis and collagen deposition by copper. *Biomaterials*, *31* (5), 824–831.

[34] Binulal, N. S., Natarajan, A., Menon, D., Bhaskaran, V. K., Mony, U., and Nair, S. V. (2014). PCL–gelatin composite nanofibers electrospun using diluted acetic acid–ethyl acetate solvent system for stem cell-based bone tissue engineering. *Journal of Biomaterials Science, Polymer Edition*, *25* (4), 325–340.

[35] Gupta, D., Venugopal, J., Prabhakaran, M. P., Dev, V. R. G., Low, S., Choon, A. T., and Ramakrishna, S. (2009). Aligned and random nanofibrous substrate for the in vitro culture of Schwann cells for neural tissue engineering. *Acta Biomaterialia*, *5* (7), 2560–2569.

[36] Lu, Y., Jiang, H., Tu, K., and Wang, L. (2009). Mild immobilization of diverse macromolecular bioactive agents onto multifunctional fibrous membranes prepared by coaxial electrospinning. *Acta Biomaterialia*, *5* (5), 1562–1574.

[37] Heydarkhan-Hagvall, S., Schenke-Layland, K., Dhanasopon, A. P., Rofail, F., Smith, H., Wu, B. M., Shemin, R., Beygui, R. E., and MacLellan, W. R. (2008). Three-dimensional electrospun ECM-based hybrid scaffolds for cardiovascular tissue engineering. *Biomaterials*, *29* (19), 2907–2914.

[38] Chong, E. J., Phan, T. T., Lim, I. J., Zhang, Y. Z., Bay, B. H., Ramakrishna, S., and Lim, C. T. (2007). Evaluation of electrospun PCL/gelatin nanofibrous scaffold for wound healing and layered dermal reconstitution. *Acta Biomaterialia*, *3* (3), 321–330.

[39] Tığlı, R. S., Kazaroğlu, N. M., Mavıs, B., and Gümüsderelioğlu, M. (2011). Cellular behavior on epidermal growth factor (EGF)-immobilized PCL/ gelatin nanofibrous scaffolds. *Journal of Biomaterials Science, Polymer Edition*, *22* (1–3), 207–223.

[40] Safi, S., Morshed, M., Hosseini Ravandi, S. A., and Ghiaci, M. (2007). Study of electrospinning of sodium alginate, blended solutions of sodium alginate/ poly(vinyl alcohol) and sodium alginate/poly(ethylene oxide). *Journal of Biomaterials Science, Polymer Edition*, *104*, 3245–3255.

[41] Moon, S. C., Ryu, B. Y., Choi, J. K., Jo, B. W., and Farris, R. J. (2009). The morphology and mechanical properties of sodium alginate based electrospun poly(ethylene oxide) nanofibers. *Polymer Engineering & Science*, *49* (1), 52–59.

[42] Shalumon, K. T. Anulekha, K. H., Nair, S. V., Nair, S. V., Chennazhi, K. P., and Jayakumar, R. (2011). Sodium alginate/poly(vinyl alcohol)/nano ZnO composite nanofibers for antibacterial wound dressings. *International Journal of Biological Macromolecules*, *49* (3), 247–254.

[43] Lee, Y. J., Shin, D. S., Kwon, O. W., Park, W. H., Choi, H. G., Lee, Y. R., Han, S. S., Noh, S. K., and Lyoo, W. S. (2007). Preparation of atactic poly(vinyl alcohol)/sodium alginate blend nanowebs by electrospinning. *Journal of Applied Polymer Science*, *106* (2), 1337–1342.

[44] Li, W., Li, X., Chen, Y., Li, X., Deng, H., Wang, T., Huang, R., and Fan, G. (2013). Poly(vinyl alcohol)/sodium alginate/layered silicate based nanofibrous mats for bacterial inhibition. *Carbohydrate Polymers*, *92* (2), 2232–2238.

[45] Zhang, Y. Z., Venugopal, J., Huang, Z. M., Lim, C. T., and Ramakrishna, S. (2006). Crosslinking of the electrospun gelatin nanofibers. *Polymer*, *47* (8), 2911–2917.

[46] Sikareepaisan, P., Suksamrarn, A., and Supaphol, P. (2008). Electrospun gelatin fiber mats containing a herbal – Centella asiatica – extract and release characteristic of asiaticoside. *Nanotechnology*, *19* (1), 015102.

[47] Zhao, P., Jiang, H., Pan, H., Zhu, K., and Chen, W. (2007). Biodegradable fibrous scaffolds composed of gelatin coated poly(ϵ-caprolactone) prepared by coaxial electrospinning. *Journal of Biomedical Materials Research Part A*, *83* (2), 372–382.

[48] Zhang, Y., Ouyang, H., Lim, C. T., Ramakrishna, S., and Huang, Z. M. (2005). Electrospinning of gelatin fibers and gelatin/PCL composite fibrous scaffolds. *Journal of Biomedical Materials Research Part B: Applied Biomaterials*, *72* (1), 156–165.

[49] Zhang, Y., Huang, Z. M., Xu, X., Lim, C. T., and Ramakrishna, S. (2004). Preparation of core−shell structured PCL-r-gelatin bi-component nanofibers by coaxial electrospinning. *Chemistry of Materials*, *16* (18), 3406–3409.

[50] Chen, J. P., Ho, K. H., Chiang, Y. P., and Wu, K. W. (2009). Fabrication of electrospun poly(methyl methacrylate) nanofibrous membranes by statistical approach for application in enzyme immobilization. *Journal of Membrane Science*, *340* (1–2), 9–15.

[51] Yördem, O. S., Papila, M., and Menceloğlu, Y. Z. (2008). Effects of electrospinning parameters on polyacrylonitrile nanofiber diameter: An investigation by response surface methodology. *Materials & Design*, *29* (1), 34–44.

[52] Gómez-Tejedor, J. A., Overberghe, N. V., Rico, P., and Ribelles, J. L. G. (2011). Assessment of the parameters influencing the fiber characteristics of electrospun poly(ethyl methacrylate) membranes. *European Polymer Journal*, *47* (2), 119–129.

[53] Kołbuk, D., Sajkiewicz, P., Maniura-Weber, K., and Fortunato, G. (2013). Structure and morphology of electrospun polycaprolactone/gelatine nanofibers. *European Polymer Journal*, *49* (8), 2052–2061.

[54] Drexler, J. W., and Powell, H. M. (2011). Regulation of electrospun scaffold stiffness via coaxial core diameter. *Acta Biomaterialia*, *7* (3), 1133–1139.

[55] Ratanavaraporn, J., Rangkupan, R., Jeeratawatchai, H., Kanokpanont, S., and Damrongsakkul, S. (2010). Influences of physical and chemical crosslinking techniques on electrospun type A and B gelatin fiber mats. *International Journal of Biological Macromolecules*, *47* (4), 431–438.

[56] Ki, C. S., Baek, D. H., Gang, K. D., Lee, K. H., Um, I. C., and Park, Y. H. (2005). Characterization of gelatin nanofiber prepared from gelatin–formic acid solution. *Polymer*, *46* (14), 5094–5102.

[57] An, K., Liu, H., Guo, S., Kumar, D. N. T., and Wang, Q. (2010). Preparation of fish gelatin and fish gelatin/poly(L-lactide) nanofibers by electrospinning. *International Journal of Biological Macromolecules*, *47* (3), 380–388.

[58] Beachley, V., and Wen, X. (2009). Effect of electrospinning parameters on the nanofiber diameter and length. *Materials Science and Engineering: C*, *29* (3), 663–668.

[59] Dias, J., and Bártolo, P. (2013). Morphological characteristics of electrospun PCL meshes – the influence of solvent type and concentration. *Procedia CIRP*, *5*, 216–221.

[60] Wu, Y., and Clark, R. L. (2007). Controllable porous polymer particles generated by electrospraying. *Journal of Colloid and Interface Science*, *310* (2), 529–535.

[61] Doustgani, A., Vasheghani-Farahani, E., Soleimani, M., and Hashemi-Najafabadi, S. (2012). Optimizing the mechanical properties of electrospun polycaprolactone and nanohydroxyapatite composite nanofibers. *Composites Part B*, *43* (4), 1830–1836.

[62] Gu, S. Y., Ren, J., and Vancso, G. J. (2005). Process optimization and empirical modeling for electrospun polyacrylonitrile (PAN) nanofiber precursor of carbon nanofibers. *European Polymer Journal*, *41* (11), 2559–2568.

[63] Huang, X. J., Chen, P. C., Huang, F., Ou, Y., Chen, M. R., and Xu, Z. K. (2011). Immobilization of Candida rugosa lipase on electrospun cellulose nanofiber membrane. *Journal of Molecular Catalysis B: Enzymatic*, *70* (3–4), 95–100.

[64] Ray, S., and Lalman, J. A. (2011). Using the Box–Benkhen design (BBD) to minimize the diameter of electrospun titanium dioxide nanofibers. *Chemical Engineering Journal*, *169* (1–3), 116–125.

[65] Padmanabhan, T., Kamaraj, V., Magwood Jr., L., and Starly, B. (2011). Experimental investigation on the operating variables of a near-field

electrospinning process via response surface methodology. *Journal of Manufacturing Processes*, *13* (2), 104–112.

[66] Neo, Y. P., Ray, S., Easteal, A. J., Nikolaidis, M. G., and Quek, S. Y. (2012). Influence of solution and processing parameters towards the fabrication of electrospun zein fibers with sub-micron diameter. *Journal of Food Engineering*, *109* (4), 645–651.

[67] Kong, L. and Ziegler, G. R. (2013). Quantitative relationship between electrospinning parameters and starch fiber diameter. *Carbohydrate Polymers*, *92* (2), 1416–1422.

[68] Aliabadi, M., Irani, M., Ismaeili, J., and Najafzadeh, S. (2014). Design and evaluation of chitosan/hydroxyapatite composite nanofiber membrane for the removal of heavy metal ions from aqueous solution. *Journal of the Taiwan Institute of Chemical Engineers*, *45* (2), 518–526.

[69] Konwarh, R., Misra, M., Mohanty, A. K., and Karak, N. (2013). Diameter-tuning of electrospun cellulose acetate fibers: A Box–Behnken design (BBD) study. *Carbohydrate Polymers*, *92* (2), 1100–1106.

[70] Sarlak, N., Nejad, M. A. F., Shakhesi, S., and Shabani, K. (2012). Effects of electrospinning parameters on titanium dioxide nanofibers diameter and morphology: An investigation by Box–Wilson central composite design (CCD). *Chemical Engineering Journal*, *210*, 410–416.

[71] Roso, M., Lorenzetti, A., Besco, S., Monti, M., Berti, G., and Modesti, M. (2011). Application of empirical modelling in multi-layers membrane manufacturing. *Computers & Chemical Engineering*, *35* (11), 2248–2256.

[72] Ghasemi-Mobarakeh, L., Prabhakaran, M. P., Morshed, M., Nasr-Esfahani, M. H., and Ramakrishna, S. (2008). Electrospun poly(ε-caprolactone)/gelatin nanofibrous scaffolds for nerve tissue engineering. *Biomaterials*, *29* (34), 4532–4539.

[73] Hartman, O., Zhang, C., Adams, E. L., Farach-Carson, M. C., Petrelli, N. J., Chase, B. D., and Rabolt, J. F. (2010). Biofunctionalization of electrospun PCL-based scaffolds with perlecan domain IV peptide to create a 3-D pharmacokinetic cancer model. *Biomaterials*, *31* (21), 5700–5718.

[74] Padalhin, A. R., Linh, N. T. B., Min, Y. K., and Lee, B. T. (2014). Evaluation of the cytocompatibility hemocompatibility in vivo bone tissue regenerating capability of different PCL blends. *Journal of Biomaterials Science, Polymer Edition*, *25* (5), 487–503.

[75] Kim, M. S., Jun, I., Shin, Y. M., Jang, W., Kim, S. I., and Shin, H. (2010). The development of genipin-crosslinked poly(caprolactone) (PCL)/gelatin nanofibers for tissue engineering applications. *Macromolecular Bioscience*, *10* (1), 91–100.

[76] Kai, D., Prabhakaran, M. P., Jin, G., and Ramakrishna, S. (2011). Guided orientation of cardiomyocytes on electrospun aligned nanofibers for

cardiac tissue engineering. *Journal of Biomedical Materials Research Part B: Applied Biomaterials*, *98* (2), 379–386.

[77] Ghasemi-Mobarakeh, L., Prabhakaran, M. P., Nematollahi, M., Karbalaie, K. Ramakrishna, S., and Nasr-Esfahani, M. H. (2014). Embryonic stem cell differentiation to cardiomyocytes on nanostructured scaffolds for myocardial tissue regeneration. *International Journal of Polymeric Materials and Polymeric Biomaterials*, *63* (5), 240–245.

[78] Sukigara, S., Gandhi, M., Ayutsede, J., Micklus, M., and Ko, F. (2004). Regeneration of *Bombyx mori* silk by electrospinning. Part 2. Process optimization and empirical modeling using response surface methodology. *Polymer*, *45* (11), 3701–3708.

[79] Nasouri, K., Bahrambeygi, H., Rabbi, A., Shoushtari, A. M., and Kaflou, A. (2012). Modeling and optimization of electrospun PAN nanofiber diameter using response surface methodology and artificial neural networks. *Journal of Applied Polymer Science*, *126* (1), 127–135

[80] Ziabari, M., Mottaghitalab, V., and Haghi, A. K. (2010). A new approach for optimization of electrospun nanofiber formation process. *Korean Journal of Chemical Engineering*, *27* (1), 340–354.

[81] Gu, S. Y., and Ren, J. (2005). Process optimization and empirical modeling for electrospun poly(D,L-lactide) fibers using response surface methodology. *Macromolecular Materials and Engineering*, *290* (11), 1097–1105.

[82] Agarwal, P., Mishra, P. K., and Srivastava, P. (2012). Statistical optimization of the electrospinning process for chitosan/polylactide nanofabrication using response surface methodology. *Journal of Materials Science*, *47* (10), 4262–4269.

[83] Askari, M., Rezaei, B., Shoushtari, A. M., Noorpanah, P., Abdouss, M., and Ghani, M. (2014). Fabrication of high performance chitosan/polyvinyl alcohol nanofibrous mat with controlled morphology and optimised diameter. *The Canadian Journal of Chemical Engineering*, *92* (6), 1008–1015.

[84] Huang, Z. M., Zhang, Y. Z., Ramakrishna, S., and Lim, C. T. (2004). Electrospinning and mechanical characterization of gelatin nanofibers. *Polymer*, *45* (15), 5361–5368.

[85] Choktaweesap, N., Arayanarakul, K., Aht-Ong, D., Meechaisue, C., and Supaphol, P. (2007). Electrospun gelatin fibers: effect of solvent system on morphology and fiber diameters. *Polymer Journal*, *39*, 622–631.

[86] Songchotikunpan, P., Tattiyakul, J., and Supaphol, P. (2008). Extraction and electrospinning of gelatin from fish skin. *International Journal of Biological Macromolecules*, *42* (3), 247–255.

[87] Gu, S. Y., Wang, Z. M., Ren, J., and Zhang, C. Y. (2009). Electrospinning of gelatin and gelatin/poly(L-lactide) blend and its characteristics for wound dressing. *Materials Science and Engineering: C*, *29* (6), 1822–1828.

[88] Li, L., Jiang, Z., Xu, J., and Fang, T. (2014). Predicting poly(vinyl pyrrolidone)'s solubility parameter and systematic investigation of the parameters of electrospinning with response surface methodology. *Journal of Applied Polymer Science*, *131* (11), 40304.

[89] Erencia, M., Cano, F., Tornero, J. A., Macanás, J., and Carrillo, F. (2014). Resolving the electrospinnability zones and diameter prediction for the electrospinning of the gelatin/water/acetic acid system. *Langmuir*, *30* (24), 7198–7205.

[90] Bhattarai, N., Li, Z., Edmondson, D., and Zhang, M. (2006). Alginate-based nanofibrous scaffolds: structural, mechanical, and biological properties. *Advanced Materials*, *18* (11), 1463–1467.

[91] Bhattarai, N., and Zhang, M. (2007). Controlled synthesis and structural stability of alginate-based nanofibers. *Nanotechnology*, *18* (45), 455601.

[92] Saquing, C. D., Tang, C., Monian, B., Bonino, C. A., Manasco, J. L., Alsberg, E., and Khan, S. A. (2013). Alginate−polyethylene oxide blend nanofibers and the role of the carrier polymer in electrospinning. *Industrial & Engineering Chemistry Research*, *52* (26), 8692–8704.

[93] Khanlou, H. M., Sadollah, A., Ang, B. C., Kim, J. H., Talebian, S., Ghadimi, A. (2014). Prediction and optimization of electrospinning parameters for polymethyl methacrylate nanofiber fabrication using response surface methodology and artificial neural networks. *Neural Computing and Applications*, *25* (3), 767–777.

[94] Hakkak, F., and Rafizadeh, M. (2013). Optimization of electrospun polyacrylonitrile/poly(vinylidene fluoride) nanofiber diameter using the response surface method. *Journal of Macromolecular Science, Part B Physics*, *52* (9), 1250–1264.

[95] Amiraliyan, N., Nouri, M., and Kish, M. H. (2009). Electrospinning of silk nanofibers. I. An investigation of nanofiber morphology and process optimization using response surface methodology. *Fibers and Polymers*, *10* (2), 167–176.

[96] Ali, A. A., Eltabey, M. M., Farouk, W. M., and Zoalfakar, S. H. (2014). Electrospun precursor carbon nanofibers optimization by using response surface methodology. *Journal of Electrostatics*, *72* (6), 462–469.

[97] Maleki, H., Gharehaghaji, A. A., Criscenti, G., Moroni, L., and Dijkstra, P. J. (2015). The influence of process parameters on the properties of electrospun PLLA yarns studied by the response surface methodology. *Journal of Applied Polymer Science*, *132* (5), 41388.

[98] Gönen, S. Ö., Erol Taygun, M., and Küçükbayrak, S. (2015). Effects of electrospinning parameters on gelatin/poly(ε-caprolactone) nanofiber diameter: an investigation by Box–Behnken design. *Chemical Engineering & Technology*, *38* (5), 1–8.

[99] Moon, S. C., and Farris, R. J. (2009). Electrospinning of heated gelatin-sodium alginate water solutions. *Polymer Engineering & Science*, *49* (8), 1616–1620.

[100] Nie, H., He, A., Zheng, J., Xu, S., Li, J., and Han, C. C. (2008). Effects of chain conformation and entanglement on the electrospinning of pure alginate. *Biomacromolecules*, *9* (5), 1362–1365.

[101] Fang, D., Liu, Y., Jiang, S., Nie, J., and Ma, G. (2011). Effect of intermolecular interaction on electrospinning of sodium alginate. *Carbohydrate Polymers*, *85*, 276–279.

[102] Lu, J. W., Zhu, Y. L., Guo, Z. X., Hu, P., and Yu, J. (2006). Electrospinning of sodium alginate with poly(ethylene oxide). *Polymer*, *47* (23), 8026–8031.

[103] Park, S. A., Park, K. E., and Kim, W. D. (2010). Preparation of sodium alginate/poly(ethylene oxide) blend nanofibers with lecithin. *Macromolecular Research*, *18* (9), 891–896.

[104] Bonino, C. A., Krebs, M. D., Saquing, C. D., Jeong, S. I., Shearer, K. L., Alsberg, E., and Khan, S. A. (2011). Electrospinning alginate-based nanofibers: from blends to crosslinked low molecular weight alginate-only systems. *Carbohydrate Polymers*, *85* (1), 111–119.

[105] Leung, V., Hartwell, R., Elizei, S. S., Yang, H., Ghahary, A., and Ko, F. (2014). Postelectrospinning modifications for alginate nanofiber-based wound dressings. *Journal of Biomedical Materials Research Part B: Applied Biomaterials*, *102* (3), 508–515.

[106] Islam, M. S., and Karim, M. R. (2010). Fabrication and characterization of poly(vinyl alcohol)/alginate blend nanofibers by electrospinning method. *Colloids and Surfaces A: Physicochemical and Engineering Aspects*, *366* (1–3), 135–140.

[107] Binulal, N. S., Natarajan, A., Menon, D., Bhaskaran, V. K., Mony, U., and Nair, S. V. (2012). Gelatin nanoparticles loaded poly(ε-caprolactone) nanofibrous semi-synthetic scaffolds for bone tissue engineering. *Biomedical Materials*, *7* (6), 065001.

[108] Almeida, P. F., and Almeida, A. J. (2004). Cross-linked alginate–gelatine beads: a new matrix for controlled release of pindolol. *Journal of Controlled Release*, *97* (3), 431–439.

[109] Saravanan, M., and Rao, K. P. (2010). Pectin–gelatin and alginate–gelatin complex coacervation for controlled drug delivery: influence of anionic polysaccharides and drugs being encapsulated on physicochemical properties of microcapsules. *Carbohydrate Polymers*, *80* (3), 808–816.

[110] Saarai, A., Kasparkova, V., Sedlacek, T., and Saha, P. (2013). On the development and characterization of crosslinked sodium alginate/gelatine hydrogels. *Journal of the Mechanical Behavior of Biomedical Materials*, *18*, 152–166.

[111] Boateng, J., Burgos-Amador, R., Okeke, O., and Pawar, H. (2015). Composite alginate and gelatin based bio-polymeric wafers containing silver sulfadiazine for wound healing. *International Journal of Biological Macromolecules*, *79*, 63–71.

[112] Thu, H. E., and Ng, S. F. (2013). Gelatine enhances drug dispersion in alginate bilayer film via the formation of crystalline microaggregates. *International Journal of Pharmaceutics*, *454* (1), 99–106.

[113] Pawar, K., Mueller, R., Caioni, M., Prang, P., Bogdahn, U., Kunz, W., and Weidner, N. (2011). Increasing capillary diameter and the incorporation of gelatin enhance axon outgrowth in alginate-based anisotropic hydrogels. *Acta Biomaterialia*, *7*, 2826–2834.

[114] Graulus, G. J., Mignon, A., van Vlierberghe, S., Declercq, H., Fehér, K., Cornelissen, M., Martins, C., and Dubruel, P. (2015). Cross-linkable alginate-graft-gelatin copolymers for tissue engineering applications. *European Polymer Journal*, *72*, 494–506.

[115] Chen, H. C., Jao, W. C., and Yang, M. C. (2009). Characterization of gelatin nanofibers electrospun using ethanol/formic acid/water as a solvent. *Polymers for Advanced Technologies*, *20* (2), 98–103.

[116] Zha, Z., Teng, W., Markle, V., Dai, Z., and Wu, X. (2012). Fabrication of gelatin nanofibrous scaffolds using ethanol/phosphate buffer saline as a benign solvent. *Biopolymers*, *97* (12), 1026–1036.

[117] Casper, C. L., Yang, W., Farach–Carson, M. C., and Rabolt, J. F. (2007). Coating electrospun collagen and gelatin fibers with perlecan domain I for increased growth factor binding. *Biomacromolecules*, *8* (4), 1116–1123.

[118] Zhang, S., Huang, Y., Yang, X., Mei, F., Ma, Q., Chen, G., Ryu, S., and Deng, X. (2009). Gelatin nanofibrous membrane fabricated by electrospinning of aqueous gelatin solution for guided tissue regeneration. *Journal of Biomedical Materials Research Part A*, *90* (3), 671–679.

[119] Song, J. H., Kim, H. E., and Kim, H. W. (2008). Production of electrospun gelatin nanofiber by water-based co-solvent approach. *Journal of Materials Science: Materials in Medicine*, *19* (1), 95–102.

[120] Wu, C., Zhou, Y., Xu, M., Han, P., Chen, L., Chang, J., and Xiao, Y. (2013). Copper-containing mesoporous bioactive glass scaffolds with multifunctional properties of angiogenesis capacity, osteostimulation and antibacterial activity. *Biomaterials*, *34* (2), 422–433.

[121] Bi, L., Rahaman, M. N., Day, D. E., Brown, Z., Samujh, C., Liu, X., Mohammadkhah, A., Dusevich, V., Eick, J. D., and Bonewald, L. F. (2013). Effect of bioactive borate glass microstructure on bone regeneration, angiogenesis, and hydroxyapatite conversion in a rat calvarial defect model. *Acta Biomaterialia*, *9* (8), 8015–8026.

[122] Zhao, S., Zhang, J., Zhu, M., Zhang, Y., Liu, Z., Tao, C., Zhu, Y., and Zhang, C. (2015). Three-dimensional printed strontium-containing mesoporous bioactive glass scaffolds for repairing rat critical-sized calvarial defects. *Acta Biomaterialia*, *12*, 270–280.

[123] Yunos, D. M., Ahmad, Z., and Boccaccini, A. R. (2010). Fabrication and characterization of electrospun poly-DL-lactide (PDLLA) fibrous coatings on 45S5 Bioglass® substrates for bone tissue engineering applications. *Journal of Chemical Technology and Biotechnology*, *85* (6), 768–774.

[124] Xie, J., Blough, E. R., and Wang, C. H. (2012). Submicron bioactive glass tubes for bone tissue engineering. *Acta Biomaterialia*, *8* (2), 811–819.

[125] Beigi, M. H., Ghasemi-Mobarakeh, L., Prabhakaran, M. P., Karbalaie, K., Azadeh, H., Ramakrishna, S., Baharvand, H., and Nasr-Esfahani, M. H. (2014). In vivo integration of poly(ε-caprolactone)/gelatin nanofibrous nerve guide seeded with teeth derived stem cells for peripheral nerve regeneration. *Journal of Biomedical Materials Research Part A*, *102* (12), 4554–4567.

[126] Cirillo, V., Clements, B. A., Guarino, V., Bushman, J., Kohn, J., and Ambrosio, L. (2014). A comparison of the performance of mono- and bi-component electrospun conduits in a rat sciatic model. *Biomaterials*, *35* (32), 8970–8982.

[127] Yang, X., Yang, F., Walboomers, X. F., Bian, Z., Fan, M., and Jansen, J. A. (2010). The performance of dental pulp stem cells on nanofibrous PCL/gelatin/nHA scaffolds. *Journal of Biomedical Materials Research Part A*, *93* (1), 247–257.

[128] Fu, W., Liu, Z., Feng, B., Hu, R., He, X., Wang, H., Yin, M., Huang, H., Zhang, H., and Wang, W. (2014). Electrospun gelatin/PCL and collagen/PLCL scaffolds for vascular tissue engineering. *Journal of International Journal of Nanomedicine*, *9*, 2335–2344.

[129] Pereira, I. H. L., Ayres, E., Averous, L., Schlatter, G., Hebraud, A., de Paula, A. C. C., Viana, P. H. L., Goes, A. M., and Oréfice, R. L. (2014). Differentiation of human adipose-derived stem cells seeded on mineralized electrospun co-axial poly(ε-caprolactone) (PCL)/gelatin nanofibers. *Journal of Materials Science: Materials in Medicine*, *25* (4), 1137–1148.

[130] Liu, J., Nie, H., Xu, Z., Niu, X., Guo, S., Yin, J., Guo, F., Li, G., Wang, Y., and Zhang, C. (2014). The effect of 3D nanofibrous scaffolds on the chondrogenesis of induced pluripotent stem cells and their application in restoration of cartilage defects. *PLoS ONE*, *9* (11), e111566.

[131] He, X., Feng, B., Huang, C., Wang, H., Ge, Y., Hu, R., Yin, M., Xu, Z., Wang, W., Fu, W., and Zheng, J. (2015). Electrospun gelatin/polycaprolactone nanofibrous membranes combined with a coculture of bone marrow

stromal cells and chondrocytes for cartilage engineering. *Journal of International Journal of Nanomedicine*, *10*, 2089–2099.

[132] Linh, N. T. B., Min, Y. K., and Lee, B. T. (2013). Hybrid hydroxyapatite nanoparticles-loaded PCL/GE blend fibers for bone tissue engineering. *Journal of Biomaterials Science, Polymer Edition*, *24* (5), 520-538.

[133] Rajzer, I., Menaszek, E., Kwiatkowski, R., Planell, J. A., and Castano, O. (2014). Electrospun gelatin/poly(ε-caprolactone) fibrous scaffold modified with calcium phosphate for bone tissue engineering. *Materials Science and Engineering: C*, *44*, 183–190.

[134] Kouhi, M., Morshed, M., Varshosaz, J., Fathi, M. H. (2013). Poly (ε-caprolactone) incorporated bioactive glass nanoparticles and simvastatin nanocomposite nanofibers: Preparation, characterization and in vitro drug release for bone regeneration applications. *Chemical Engineering Journal*, *228*, 1057–1065.

[135] Silva, C. S. R., Luz, G. M., Gamboa-Martínez, T. C., Mano, J. F., Gómez-Ribelles, J. L., and Gómez-Tejedor, J. A. (2014). Poly(ε-caprolactone) electrospun scaffolds filled with nanoparticles. Production and optimization according to Taguchi's methodology. *Journal of Macromolecular Science Part B Physics*, *53* (5), 781–799.

[136] Noh, K. T., Lee, H. Y., Shin, U. S., and Kim, H. W. (2010). Composite nanofiber of bioactive glass nanofiller incorporated poly(lactic acid) for bone regeneration. *Materials Letters*, *64* (7), 802–805.

[137] Allo, B. A., Lin, S., Mequanint, K., and Rizkalla, A. S. (2013). Role of bioactive 3D hybrid fibrous scaffolds on mechanical behavior and spatiotemporal osteoblast gene expression. *ACS Applied Materials & Interfaces*, *5* (15), 7574−7583.

[138] Kim, G. H., Park, Y. D., Lee, S. Y., El-Fiqi, A., Kim, J. J., Lee, E. J., Kim, H. W., and Kim, E. C. (2015). Odontogenic stimulation of human dental pulp cells with bioactive nanocomposite fiber. *Journal of Biomaterials Applications*, *29* (6), 854–866.

[139] Talebian, S., Mehrali, M., Mohan, S., Raghavendran, H. R. B., Mehrali, M., Khanlou, H. M., Kamarul, T., Afifi, A. M., and Abass, A. A. (2014). Chitosan (PEO)/bioactive glass hybrid nanofibers for bone tissue engineering. *RSC Advances*, *4*, 49144–49152.

[140] Santocildes-Romero, M. E., Crawford, A., Hatton, P. V., Goodchild, R. L., Reaney, I. M., and Miller, C. A. (2015). The osteogenic response of mesenchymal stromal cells to strontium-substituted bioactive glasses. *Journal of Tissue Engineering and Regenerative Medicine*, *9* (5), 619–631.

[141] Gao, C., Gao, Q., Bao, X., Li, Y., Teramoto, A., and Abe, K. (2011). Preparation and in vitro bioactivity of novel mesoporous borosilicate

bioactive glass nanofibers. *Journal of the American Ceramic Society*, *94* (9), 2841–2845.

[142] Hong, Y., Chen, X., Jing, X., Fan, H., Guo, B., Gu, Z., and Zhang, X. (2010). Preparation, bioactivity, and drug release of hierarchical nanoporous bioactive glass ultrathin fibers. *Advanced Materials*, *22* (6), 754–758.

[143] Hong, Y., Chen, X., Jing, X., Fan, H., Gu, Z., and Zhang, X. (2010). Fabrication and drug delivery of ultrathin mesoporous bioactive glass hollow fibers. *Advanced Functional Materials*, *20* (9), 1503–1510.

[144] Asgharnia, S., and Alizadeh, P. (2013). Synthesis and characterization of SiO_2–CaO–P_2O_5–MgO based bioactive glass and glass-ceramic nanofibres by electrospinning. *Materials Letters*, *101*, 107–110.

[145] Li, Y., Li, B., Xu, G., Ahmad, Z., Ren, Z., Dong, Y., Li, X., Weng, W., and Han, G. (2014). A feasible approach toward bioactive glass nanofibers with tunable protein release kinetics for bone scaffolds. *Colloids and Surfaces B: Biointerfaces*, *122*, 785–791.

[146] Deliormanlı, A. M. (2015). Preparation and in vitro characterization of electrospun 45S5 bioactive glass nanofibers. *Ceramics International*, *41* (1), 417–425.

[147] Wang, D., Lin, H., Jiang, J., Jin, Q., Li, L., Dong, Y., and Qu, F. (2015). Fabrication of long-acting drug release property of hierarchical porous bioglasses/polylactic acid fibre scaffolds for bone tissue engineering. *IET Nanobiotechnology*, *9* (2), 58–65.

[148] Rujitanaroj, P. O., Pimph, N., and Supaphol, P. (2008). Wound-dressing materials with antibacterial activity from electrospun gelatin fiber mats containing silver nanoparticles. *Polymer*, *49* (21), 4723–4732.

[149] Xu, J., Yan, J., Gu, Q., Li, J., and Wang, H. (2011). Preparation of fluoride-containing gelatin nanofiber scaffold. *Materials Letters*, *65* (15–16), 2404–2406.

[150] Gomes, S. R., Rodrigues, G., Martins, G. G., Henriques, C. M. R., and Silva, J. C. (2013). In vitro evaluation of crosslinked electrospun fish gelatin scaffolds. *Materials Science and Engineering: C*, *33* (3), 1219–1227.

[151] Wang, H., Feng, Y., Fang, Z., Xiao, R., Yuan, W., and Khan, M. (2013). Fabrication and characterization of electrospun gelatin-heparin nanofibers as vascular tissue engineering. *Macromolecular Research*, *21* (8), 860–869.

[152] Gomes, S. R., Rodrigues, G., Martins, G. G., Roberto, M. A., Mafra, M., Henriques, C. M. R, and Silva, J. C. (2015). In vitro and in vivo evaluation of electrospun nanofibers of PCL, chitosan and gelatin: A comparative study. *Materials Science and Engineering: C*, *46*, 348–358.

[153] Gauthaman, K., Venugopal, J. R., Yee, F. C., Peh, G. S. L., Ramakrishna, S., and Bongso, A. (2009). Nanofibrous substrates support colony formation

and maintain stemness of human embryonic stem cells. *Journal of Cellular and Molecular Medicine*, *13* (9), 3475–3484.

[154] Perez, M. A. A., Guarino, V., Cirillo, V., and Ambrosio, L. (2012). In vitro mineralization and bone osteogenesis in poly(ε-caprolactone)/gelatin nanofibers. *Journal of Biomedical Materials Research Part A*, *100* (11), 3008–3019.

[155] Feng, B., Tu, H., Yuan, H., Peng, H., and Zhang, Y. (2012). Acetic-acid-mediated miscibility toward electrospinning homogeneous composite nanofibers of GT/PCL. *Biomacromolecules*, *13* (12), 3917−3925.

[156] Gautam, S., Dinda, A. K., and Mishra, N. C. (2013). Fabrication and characterization of PCL/gelatin composite nanofibrous scaffold for tissue engineering applications by electrospinning method. *Materials Science and Engineering: C*, *33* (3), 1228–1235.

[157] Skotak, M., Noriega, S., Larsen, G., and Subramanian, A. (2010). Electrospun cross-linked gelatin fibers with controlled diameter: the effect of matrix stiffness on proliferative and biosynthetic activity of chondrocytes cultured in vitro. *Journal of Biomedical Materials Research Part A*, *95* (3), 828–836.

[158] Han, B., Zhang, X., Liu, H., Deng, X., Cai, Q., Jia, X., Yang, X., Wei, Y., and Li, G. (2014). Improved bioactivity of PAN-based carbon nanofibers decorated with bioglass nanoparticles. *Journal of Biomaterials Science, Polymer Edition*, *25* (4), 341–353.

[159] Hench, L. L. (1991). Bioceramics: from concept to clinic. *Journal of the American Ceramic Society*, *74* (7), 1487–1510.

[160] Wang, H., Zhao, S., Zhou, J., Shen, Y., Huang, W., Zhang, C., Rahaman, M. N., and Wang, D. (2014). Evaluation of borate bioactive glass scaffolds as a controlled delivery system for copper ions in stimulating osteogenesis and angiogenesis in bone healing. *Journal of Materials Chemistry B*, *2*, 8547–8557

[161] Hoppe, A., Sarker, B., Detsch, R., Hild, N., Mohn, D., Stark, W. J., Boccaccini, A. R. (2014). In vitro reactivity of Sr-containing bioactive glass (type 1393) nanoparticles. *Journal of Non-Crystalline Solids*, *387*, 41–46

[162] Zhao, S., Wang, H., Zhang, Y., Huang, W., Rahaman, M. N., Liu, Z., Wang, D., and Zhang, C. (2015). Copper-doped borosilicate bioactive glass scaffolds with improved angiogenic and osteogenic capacity for repairing osseous defects. *Acta Biomaterialia*, *14*, 185–196

[163] Bonnelye, E., Chabadel, A., Saltel, F., and Jurdic, P. (2008). Dual effect of strontium ranelate: stimulation of osteoblast differentiation and inhibition of osteoclast formation and resorption in vitro. *Bone*, *42* (1), 129–138.

[164] Reginster, J. Y., and Meunier, P. J. (2003). Strontium ranelate phase 2 dose ranging studies: PREVOS and STRATOS studies. *Osteoporosis International*, *14*, 56–65.

[165] Denis, P., Dulnik, J., and Sajkiewicz, P. (2015). Electrospinning and structure of bicomponent polycaprolactone/gelatin nanofibers obtained using alternative solvent system. *International Journal of Polymeric Materials and Polymeric Biomaterials*, *64* (7), 354–364.

[166] Venugopal, J. R., Low, S., Choon, A. T., Kumar, A. B., and Ramakrishna, S. (2008). Nanobioengineered electrospun composite nanofibers and osteoblasts for bone regeneration. *Artificial Organs*, *32* (5), 388–397.

[167] Chong, L. H., Lim, M. M., and Sultana, N. (2015). Fabrication and evaluation of polycaprolactone/gelatin-based electrospun nanofibers with antibacterial properties. *Journal of Nanomaterials*, *2015*, 1–8.

[168] Kouhi, M., Morshed, M., Varshosaz, J., and Fathi, M. H. (2013). Poly (ε-caprolactone) incorporated bioactive glass nanoparticles and simvastatin nanocomposite nanofibers: Preparation, characterization and in vitro drug release for bone regeneration applications. *Chemical Engineering Journal*, *228*, 1057–1065.

[169] Pezeshki-Modaress, M., Mirzadeh, H., and Zandi, M. (2015). Gelatin–GAG electrospun nanofibrous scaffold for skin tissue engineering: Fabrication and modeling of process parameters. *Materials Science and Engineering: C*, *48*, 704–712.

[170] Zarghami, A., Irani, M., Mostafazadeh, A., Golpour, M., Heidarinasab, A., and Haririan, I. (2015). Fabrication of PEO/chitosan/PCL/olive oil nanofibrous scaffolds for wound dressing applications. *Fibers and Polymers*, *16* (6), 1201–1212.

[171] Khanlou, H. M., Ang, B. C., Talebian, S., Barzani, M. M., Silakhori, M., and Fauzi, H. (2015). Multi-response analysis in the processing of poly (methyl methacrylate) nano-fibres membrane by electrospinning based on response surface methodology: Fibre diameter and bead formation. *Measurement*, *65*, 193–206.

[172] Ahmadipourroudposht, M., Fallahiarezoudar, E., Yusof, N. M., and Idris, A. (2013). Application of response surface methodology in optimization of electrospinning process to fabricate (ferrofluid/polyvinyl alcohol) magnetic nanofibers. *Materials Science and Engineering: C*, *50*, 234–241.

[173] Konwarh, R., Misra, M., Mohanty, A. K., and Karak, N. (2013). Diameter-tuning of electrospun cellulose acetate fibers: A Box–Behnken design (BBD) study. *Carbohydrate Polymers*, *92* (2), 1100–1106.

[174] Salehi, R., Irani, M., Rashidi, M. R., Aroujalian, A., Raisi, A., Eskandani, M., Haririan, I., and Davaran, S. (2013). Stimuli-responsive nanofibers prepared from poly(N-isopropylacrylamide-acrylamide-vinylpyrrolidone)

by electrospinning as an anticancer drug delivery. *Designed Monomers & Polymers, 16* (6), 515–527.

[175] Anaraki, N. A., Rad, L. R., Irani, M., and Haririan, I. (2015). Fabrication of PLA/PEG/MWCNT electrospun nanofibrous scaffolds for anticancer drug delivery. *Journal of Applied Polymer Science, 132* (3), 41286.

[176] Pezeshki-Modaress, M., Zandi, M., and Mirzadeh, H. (2015). Fabrication of gelatin/chitosan nanofibrous scaffold: process optimization and empirical modeling. *Polymer International, 64*, 571–580.

[177] Boaretti, C., Roso, M., Lorenzetti, A., and Modesti, M. (2015). Synthesis and process optimization of electrospun peek-sulfonated nanofibers by response surface methodology. *Materials, 8* (7), 4096–4117.

[178] Gönen, S. Ö., Erol Taygun, M., and Küçükbayrak, S. (2016). Evaluation of the factors influencing the resultant diameter of the electrospun gelatin/sodium alginate nanofibers via Box-Behnken design. *Materials Science and Engineering: C, 58*, 709–723.

[179] Erol, M., Özyuğuran, A., Özarpat, Ö., and Küçükbayrak, S. (2012). Investigation of strontium effect on the bioactive behavior of glasses in the system SiO_2-CaO-P_2O_5-Na_2O-SrO. *Key Engineering Materials, 493–494*, 68–73.

[180] Erol, M., Özyuğuran, A., Maraslı, M., and Kucukbayrak, S. (2013). In vitro evaluation of Sr and Cu doped bioactive glasses. *Advanced Science Letters, 19* (11), 3333–3337.

[181] Gönen, S. Ö., Erol Taygun, M., and Küçükbayrak, S. (2016). Fabrication of bioactive glass containing nanocomposite fiber mats for bone tissue engineering applications. *Composite Structures, 138*, 96–106.

[182] Kepler, R. G., Anderson, R. A., and Lagasse, R. R. (1982). Electric field dependence of crystallinity in poly(vinylidene fluoride). *Physical Review Letters, 48* (18), 1274.

[183] Gautam, S., Chou, C. F., Dinda, A. K., Potdar, P. D., and Mishra, N. C. (2014). Surface modification of nanofibrous polycaprolactone/gelatin composite scaffold by collagen type I grafting for skin tissue engineering. *Materials Science and Engineering: C, 34*, 402–409.

[184] Deliormanlı, A. M. (2015). Preparation, in vitro mineralization and osteoblast cell response of electrospun 13–93 bioactive glass nanofibers. *Materials Science and Engineering: C, 53*, 262–271.

CURRICULUM VITAE

Name Surname **:** Seza Özge Gönen

Place and Date of Birth **:** İstanbul / May 1987

E-Mail **:** gonens@itu.edu.tr

EDUCATION **:**

- **B.Sc.** **:** 2008, ITU, Chemical and Metallurgical Faculty, Chemical Engineering Department
- **M.Sc.** **:** 2010, ITU, Chemical and Metallurgical Faculty, Chemical Engineering Department

PROFESSIONAL EXPERIENCE AND REWARDS:

- 2015 – date R&D Engineer at EVYAP
- 2010 – 2016 TÜBİTAK–BİDEB 2211 Scholarship for PhD candidates
- 2008 – 2010 TÜBİTAK–BİDEB 2210 Scholarship for MSc students

PUBLICATIONS, PRESENTATIONS AND PATENTS ON THE THESIS:

- **Gönen, S. Ö.**, Erol Taygun, M., and Küçükbayrak, S., 2015: Fabrication Of Bioactive Glass Containing Nanocomposite Fiber Mats For Bone Tissue Engineering Applications. International Conference on Advances in Composite Materials and Structures, April 13-15, 2015 Istanbul, Turkey.
- **Gönen, S. Ö.**, Erol Taygun, M., and Küçükbayrak, S., 2015. Effects Of Electrospinning Parameters On Gelatin/Poly(ε-Caprolactone) Nanofiber Diameter:

An Investigation By Box–Behnken Design, *Chemical Engineering & Technology*, *38* (5), 1–8.

- **Gönen, S. Ö.**, Erol Taygun, M., and Küçükbayrak, S., 2016. Evaluation Of The Factors Influencing The Resultant Diameter Of The Electrospun Gelatin/Sodium Alginate Nanofibers Via Box–Behnken Design, *Materials Science and Engineering: C*, *58*, 709–723.
- **Gönen, S. Ö.**, Erol Taygun, M., and Küçükbayrak, S., 2016. Fabrication Of Bioactive Glass Containing Nanocomposite Fiber Mats For Bone Tissue Engineering Applications, *Composite Structures*, *138*, 96–106.
- **Gönen, S. Ö.**, Erol Taygun, M., Aktürk, A., and Küçükbayrak, S., 2016. Fabrication Of Nanocomposite Mat Through Incorporating Bioactive Glass Particles Into Gelatin/Poly(ε-Caprolactone) Nanofibers By Using Box–Behnken Design, *Materials Science and Engineering: C*, *67*, 684–693.
- **Gönen, S. Ö.**, Erol Taygun, M., and Küçükbayrak, S., 2016. Empirical Modeling Of The Average Diameter Of Gelatin/Sodium Alginate Containing Nanocomposite Fibers, *Carbohydrate Polymers*, Submitted Manuscript.
- **Gönen, S. Ö.**, Erol Taygun, M., Aktürk, A., and Küçükbayrak, S., 2016. Evaluation Of Gelatin/Sodium Alginate Containing Fibrous Mats As Bone Tissue Engineering Scaffolds, *Composite Structures*, Submitted Manuscript.

OTHER PUBLICATIONS, PRESENTATIONS AND PATENTS:

- **Gönen, S. Ö.**, and Baysan, S., 2012. Fuzzy Topsis With Linguistic Evaluations Using α–Cuts. *Uncertainty Modeling in Knowledge Engineering and Decision Making: Proceedings of the 10th International FLINS Conference*, 112-117.
- **Gönen, S. Ö.**, Ertürk, B., Tüccar, E., Erol Taygun, M., and Küçükbayrak, S., 2014: Elektrospinning Parametrelerinin Jelatin/Biyoaktif Cam Nanolif Yapısı Üzerindeki Etkilerinin İncelenmesi [Effects Of Electrospinning Parameters On Gelatin/Bioactive Glass Nanofiber Diameter]. 11th National Chemical Engineering Congress, September 2-5, 2014 Eskişehir, Turkey.
- **Gönen, S. Ö.**, Kadakal, G., Öztürk, N., Yaman, D., Memişler, N., and Erol Taygun, M., Küçükbayrak, S., 2014: Polimer/Biyoaktif Cam Nanokompozit Malzemelerin Kemik Doku Mühendisliği Uygulamalarında Kullanım Alanlarının İncelenmesi [Investigation Of Polymer/Bioactive Glass Nanocomposite Materials For Applications In Bone Tissue Engineering]. 11th National Chemical Engineering Congress, September 2-5, 2014 Eskişehir, Turkey.
- **Gönen, S. Ö.**, Ertürk, B., Tüccar, E., Erol Taygun, M., and Küçükbayrak, S., 2015. Elektrospinning Parametrelerinin Jelatin/Biyoaktif Cam Nanolif Yapısı Üzerindeki Etkilerinin İncelenmesi, *Anadolu Üniversitesi Bilim ve Teknoloji Dergisi A - Uygulamalı Bilimler ve Mühendislik*, *16* (2), 135–144.